



Norwegian University of
Science and Technology

Description and Structural Analysis of a Marine Bridge for the Digernessund crossing

Elise Hellvik

Marine Technology

Submission date: June 2018

Supervisor: Bernt Johan Leira, IMT

Norwegian University of Science and Technology
Department of Marine Technology

Preface

This report presents a master thesis in marine structural engineering. The thesis was written at the Department of Marine Technology at the Norwegian University of Science and Technology (NTNU) in Trondheim. It was carried out during the spring 2018. The formulation of the thesis was established by Prof. Bernt Johan Leira, representing the Department of Marine Technology.

The topic of the thesis is marine bridges, with focus on submerged floating tunnels. It contains modeling and analysis of a previously developed concept for a submerged floating bridge, prepared by dr. Techn. Olav Olsen in 2016. Information concerning the concept was distributed by the National Public Road Administration (Statens Vegvesen). Please note that this thesis presents an extension of the work done in the authors project thesis, which was written during autumn 2017. Some of the theory sections are taken directly from the project thesis.

First, I would like to thank my supervisor Bernt Johan Leira for his support and for always answering questions. I want to thank Arianna Minoretti and Mathias Eidem Egeland from the NPRA for answering questions regarding the developed concept for the Digernessund. I want to thank the Sesam support team for answering all questions related to the Sesam software. I also want to thank my father, for being supportive and for answering questions regarding concrete structures in general. I want to thank my mom and my boyfriend William, for being supportive and for always believing in me. Finally, I want to thank all my friends at NTNU for five fun years in Trondheim.



Elise Hellvik, Trondheim June 11, 2018



Master Thesis, Spring 2018
for
Master Student Elise Hellvik

Description and Structural Analysis of a Marine Bridge for the Digernessundet crossing

*Beskrivelse og strukturanalyse av et marint brukonsept for kryssing av
Digernessundet*

Marine bridges (i.e. floating bridges, submerged tunnels and more traditional bridge types with floating foundations) are relevant for crossing of very deep and wide lakes or fjord systems. In order to compute the static and dynamic response of these bridges, the joint properties of the entire hydro-elastic system need to be accounted for. The objective of the present project is to outline methods for response analysis and illustrate the calculation procedure for a particular bridge concept.

The following subjects are to be addressed as part of this work:

1. Review of existing marine bridges and future plans for such bridges. Similarities and differences between the different bridge types are to be highlighted. Loads acting on such bridges are described together with associated structural models. Methods for both static and dynamic response analysis are elaborated and relevant numerical algorithms are described.
2. A global model of a particular bridge (Submerged tunnel for Digernessundet) is to be established in SESAM. Static response analyses are performed. Sensitivity studies of bending moment and axial forces with respect to current direction and profile are performed.
3. Concrete stresses for the most critical sections are to be controlled. The influence of post-tension cables on the stresses is to be investigated.
4. Natural frequencies (and mode shapes) are to be computed.
5. Dynamic response analysis is to be performed for the case of swell sea.
6. Parametric studies are performed with respect to curve height. Static response analyses with different curve heights are performed, and associated natural frequencies are investigated. The objective is to find the curve height where the first horizontal mode shape consists of two halfwaves.

The work scope may prove to be larger than initially anticipated. Subject to approval from the supervisor, topics may be deleted from the list above or reduced in extent.

In the thesis the candidate shall present his personal contribution to the resolution of problems within the scope of the thesis work. Theories and conclusions should be based on mathematical derivations and/or logic reasoning identifying the various steps in the deduction.

The candidate should utilise the existing possibilities for obtaining relevant literature.

The thesis should be organised in a rational manner to give a clear exposition of results, assessments, and conclusions. The text should be brief and to the point, with a clear language. Telegraphic language should be avoided.

The thesis shall contain the following elements: A text defining the scope, preface, list of contents, summary, main body of thesis, conclusions with recommendations for further work, list of symbols and acronyms, references and (optional) appendices. All figures, tables and equations shall be numbered.

The supervisor may require that the candidate, in an early stage of the work, presents a written plan for the completion of the work. The original contribution of the candidate and material taken from other sources shall be clearly defined. Work from other sources shall be properly referenced using an acknowledged referencing system.

The thesis shall be submitted in electronic form:

- Signed by the candidate
- The text defining the scope included
- Drawings and/or computer prints which cannot be bound should be organised in a separate folder.

Supervisor: Professor Bernt J. Leira

Deadline: Juni 11th 2018

Trondheim, Januar 15th, 2018


Bernt J. Leira

Abstract

The relevance of marine bridges have increased during the past years due to the plans of renewing route E39. Different types of marine bridges have been described in this thesis, with focus on the concepts proposed for the fjord-crossings along route E39. The existing bridge over the Digernesund does not meet the new requirements for the new E39, and a submerged floating tunnel (SFT) has therefore been proposed as a replacement. The proposed SFT, given in the technical report provided by dr. Techn. Olav Olsen, has been investigated in this thesis with respect to its structural behaviour.

The SFT proposed by dr. Techn. Olav Olsen is a reinforced concrete structure with post-tension cables. The cross-section used in this thesis is rectangular, and the bridge has one single span including both driving directions. There are no intermediate supports, meaning the bridge is only supported by buoyancy and the connections to rock tunnels at the two ends. The model and structural analysis of the SFT were established and conducted in the Sesam package. The bridge was modeled as an assemble of straight 2-node beam elements creating an arc. The influence of reinforcements and post-tension cables were accounted for in the bending stiffness of the structure, in the stress calculations and in the eigenvalue analysis. The average increase of moments of inertia is 3.89% for I_z and 3.24% for I_y . The axial compression from the PT-cables was calculated 5.75% of the Euler buckling load. Thus, global buckling was not considered a problem for the base case configuration of the bridge.

Buoyancy was found as the dominating load in the vertical direction for the base case. The results from static analysis showed high reaction forces to be transferred to the abutments and high bending moments. The stress calculations showed that the maximal total compressive stresses were below the allowable limit. However, the tensile stresses from the characteristic loads exceeds the tensile strength of concrete. Thus, the weight should be increased to balance the buoyancy. A full calculation of the amount of reinforcements should be carried out and its contribution included in the weight calculations. An alternative could be to increase the ballast chamber fill percentage to increase the weight. The transverse reactions are dependent on the current direction and profile. Different directions and profiles were investigated with respect to static response. The cases of applying uniformly distributed current loads to the full length of the bridge, in either the positive or negative transverse direction, gave the highest bending moments and axial forces in the structure. It was found that the contributions in stress from axial forces and bending moments due to current loads are small compared to the contributions from PT-cables and the net vertical forces.

Eigenvalue analyses were conducted using Sestra and Abaqus, and the results were compared to results from analytical calculations. The resulting mode shapes were sim-

ilar to those given in the technical report established by dr. Techn. Olav Olsen. The eigenperiods calculated by Sestra and Abaqus deviates from the calculations by the NPRA by about 10-20%. It is assumed that this deviations can be a result of differences in modeling and assumptions for the eigenvalue analysis. The eigenfrequency for the first mode is multiplied by a reduction factor to account for the influence of the compression force from the PT-cables. The first eigenperiod for the base case was thus calculated 9.14s. The second eigenperiod, corresponding to a horizontal mode with one half-wave, was calculated 5.16s by Sestra. The third and fourth eigenperiod, corresponding to vertical and horizontal mode with two half-waves respectively, were calculated 3.34s and 3.00s by Sestra. For increasing mode number, the eigenfrequencies were closely spaced.

A parameter study of the curve height in the transverse direction were also carried out. Increasing curve height influences the static response, the eigenfrequencies and the mode shapes. The main findings were that the transverse loading is carried by axial forces and bending moments, as expected. Increasing the curve height results in reduced bending moments due to transverse loads. However, it also results in increased torsion moments due to the translation of centre of gravity along the y-axis. For eigenvalue analysis, the first horizontal mode is of interest when introducing a curve height. The result is reduced eigenfrequency for increasing curve height. At one curve height, it was expected that the first and second horizontal mode shape changes place. The curve height corresponding to the changing point was calculated 49m analytically, 53m in Sestra and 56m in Abaqus.

Swell sea was the dominating wave type at the depth of the SFT. The submergence of the tunnel provides shelter from the wave loads as the wave action at the depth of the SFT is 35.8% of the wave action at the free surface. Wave loads due to swell sea were calculated using deterministic wave load calculation in Wajac. The dynamic response was calculated using direct time domain analysis in Sestra. However, the dynamic response due to swell waves was found to be of second importance compared to the response from static loads. Displacements due to the swell waves investigated in this thesis were found negligible compared to the results from static analysis. The bending moments due to swell waves were calculated 6% of the bending moment from net static loads. To ensure conservatism in stress calculations, the bending moments from wave loads should be included.

Sammendrag

Interessen for marine broer har økt de siste årene som et resultat av planene om en fornyet E39. Ulike typer marine broer har blitt presentert i denne oppgaven, med fokus på et konsept foreslått for en fjord-krysning langs E39. Den eksisterende broen over Digernessundet møter ikke dagens krav til nye E39 og en rørbro har derfor blitt foreslått som erstatning. Den foreslåtte broen, gitt i teknisk rapport av dr. Techn. Olav Olsen, har blitt undersøkt i denne oppgaven med fokus på konstruksjonens oppførsel.

Rørbroen foreslått av dr. Techn Olav Olsen er en armert betongkonstruksjon med etteroppspanning. Tverrsnittet brukt i denne oppgaven er rektangulært. Broen har ett enkelt spenn som inneholder begge kjøreretninger. Den har ingen mellomliggende støtter, og bæres av oppdrift og endeforbindelser til fjelltunneller. Elementmodell og strukturanalyse av rørbroen har blitt utført i programvaren Sesam pakken. Broen ble modelert som en kurve, sammensatt av rette 2-nodede bjelkeelementer. Innflytelse av armering og spennkabler ble tatt hensyn til i bøyestivheten til broen, i spenningsberegninger og i egenverdianalysen. Gjennomsnittlig økning av treghetsmomentene ble beregnet til 3.89% for I_z og 3.24% for I_y . Trykk-kraften fra spennkablene ble beregnet til 5.75% av Euler knekklasten. Global knekking ble derfor ikke sett på som et problem for konseptet brukt i denne oppgaven.

Oppdrift ble observert som den dominerende lasten i vertikal retning for konseptet brukt i oppgaven. Resultatene fra statistisk analyse viste høye reaksjonskrefter og bøyemomenter. Spenningsberegningene viste at de maksimale trykk-spenningene i betongen var innenfor tillatte verdier, men strekkspenningene fra karakteristiske laster overgikk karakteristisk strekkfasthet til betongen. Det er derfor viktig at vekten økes for å balansere oppdriften. Beregning av nødvendig armering og spennkabler må utarbeides og inkluderes i vektberegningen. Alternativt kan også prosent av fyllmasser i ballastkammerne økes. Tverr-reaksjonene er avhengig av strømretning og profil. Forskjellige strømretninger og profiler ble derfor undersøkt mot statistisk respons. Jevnt fordelt strømlast påsatt over hele lengden av broen ga høyeste aksialkrefter og bøyemomenter i konstruksjonen. Spenningsbidragene fra strøm var lave sammenliknet med bidragene fra spennkablene og netto vertikale krefter.

Egenverdianalysen ble utført ved bruk av programvarene Sestra og Abaqus. Resultatene ble sammenliknet med resultater fra analytiske beregningsmodeller. Resulterende svingeformer var nærliggende svingeformene gitt i teknisk rapport. Egenfrekvensen for første svingeform ble multiplisert med en reduksjonsfaktor for å ta hensyn til trykk-kraft fra spennkablene. Den første egenperioden ble dermed beregnet til 9.14s. Den andre egenperioden, tilsvarende første horisontal svingeform, ble beregnet til 5.16s av Sestra. Tredje og fjerde, tilsvarende andre vertikale og horisontale

svingform, ble beregnet til 3.34s og 3.00s av Sestra. For økende moder viste det seg at egenfrekvensene var nærliggende hverandre. Egenperiodene beregnet fra Sestra og Abaqus avvok fra beregningene til Statens vegvesen og dr. techn. Olav Olsen med 10-20%. Det ble antatt at disse avvikene skyldes forskjeller i modellering og antakelser for egenverdi-analysen.

Parameterstudie av kurvehøyden i tverr-retning ble også utført. Endring i kurvehøyde påvirker blant annet statisk respons, egenfrekvenser og svingeformer. Hovedfunnene var at tverrlast bæres både av aksiale krefter og bøyemomenter, som forventet. Økende kurvehøyde resulterte i reduserte bøyemomenter på grunn av tverrlaster, men økt torsjonsmoment. Sistnevnte antas å skyldes forskyvning av tyngdepunktet langs tverr-retningen når kurvehøyden øker. For egenverdi-analysen var første horisontale svingform av spesiell interesse ved introduksjon av kurvehøyde. Resultatet var redusert egenfrekvens for økende kurvehøyde. Ved en bestemt kurvehøyde ble det antatt at første og andre horisontale svingform ville skifte plass. Kurvehøyden som tilsvarer dette punktet ble beregnet til 49m analytisk, 53m av Sestra og 56m av Abaqus.

Dønninger ble funnet som den dominerende bølgetypen på dybden av rørboen. Neddykkingen av broen gir beskyttelse mot bølgelaster, da bølgepåvirkningen ved dybden av rørboen er redusert til rundt 35% av bølgepåvirkningen ved overflaten. Bølgelaster på grunn av dønninger ble beregnet ved bruk av deterministisk bølgestastberegning i Wajac. Her ble dønningene antatt regulære. Dynamisk respons ble beregnet ved hjelp av direkte analyse i tidsdomenet i Sestra. Resulterende nedbøyninger på grunn av dønningene brukt i denne oppgaven var neglisjerbare i forhold til den statiske responsen. Bøyemomentene på grunn av dønninger ble beregnet 6% av bøyemoment på grunn av netto statiske laster. For å sikre konservative resultater bør man ta hensyn til disse bøyemomentene i spenningsberegningene.

Contents

- Preface** **i**
- Abstract** **iv**
- Sammendrag** **vi**
- List of Tables** **xiii**
- 1 Introduction** **1**
 - 1.1 Background 1
 - 1.2 Objective 1
 - 1.3 Limitations 2
 - 1.4 Structure of the report 2
- I Marine bridges and load theory** **3**
- 2 Review of marine bridges** **5**
 - 2.1 Conventional floating bridges 5
 - 2.2 Suspension bridges 7
 - 2.2.1 Traditional suspension bridge 7
 - 2.2.2 Suspension bridge with TLP technology 8
 - 2.3 Cable-stayed bridges 9
 - 2.3.1 Traditional cable-stayed bridge 9
 - 2.3.2 Cable-stayed bridge with TLP technolgy 9
 - 2.4 Submerged floating tunnel 10
 - 2.4.1 SFT with tether support 11
 - 2.4.2 SFT with pontoon support 12
 - 2.4.3 Free-spanning SFT 13
 - 2.4.4 Combined SFT and floating bridge 14
- 3 Developed concept of a SFT for the Digernessund** **19**
 - 3.1 Functional requirements 20
 - 3.2 Global dimensions 20
 - 3.3 Cross-section 20
 - 3.4 Materials 22
 - 3.5 Environmental conditions on site 23
 - 3.5.1 Current 23
 - 3.5.2 Wave 23

4	Loads acting on marine bridges	25
4.1	Permanent loads	25
4.1.1	Self-weight and buoyancy	25
4.1.2	Traffic load	26
4.2	Environmental loads	27
4.2.1	Tide	27
4.2.2	Ice and snow	27
4.2.3	Current loads	27
4.2.4	Wind loads	29
4.2.5	Wave-induced loads	30
4.3	Deformation loads for concrete structures	32
4.3.1	Post-tension	32
4.3.2	Creep	33
4.3.3	Temperature	33
4.4	Accidental loads	33
II	Structural analysis of a SFT	35
5	FE-model of the SFT	37
5.1	Modeling software	37
5.2	Global model	38
5.3	Material	38
5.3.1	Reinforcement steel	39
5.3.2	Post-tension cables	39
5.4	Cross-sectional properties	40
5.4.1	Transformed cross-section	41
5.5	Boundary conditions	42
5.6	Ballast	43
5.7	Hydrodynamic coefficients	44
6	Static response analysis	45
6.1	Theory of static analysis	45
6.1.1	Static analysis	45
6.1.2	Finite element formulations	50
6.2	Load cases used in static analysis of the SFT	53
6.3	Load combinations	55
6.4	Stress calculations	56
6.5	Results from static analysis	58
6.5.1	Results from Sestra compared to hand-calculations	58
6.5.2	Base case static analysis results	58
6.5.3	Results from stress calculations for base case	62
6.5.4	Results from parameter study with curve height	62
6.6	Discussion of static analysis results	63
7	Eigenvalue analysis	69
7.1	Analytical solutions for eigenvalue analysis	70
7.1.1	Oscillating beam	70
7.1.2	Oscillating curved beams	70

7.1.3	Influence of axial forces on oscillating beams	72
7.2	Modal analysis	73
7.3	Eigenvalue problem in Sestra	73
7.4	Results from eigenvalue analysis	74
7.4.1	Effects of PT-cables and reinforcements	74
7.4.2	Eigenvalue analysis results for base case	74
7.4.3	Results from parameter study with curve height	76
7.5	Discussion of eigenvalue analysis results	76
8	Dynamic response analysis	81
8.1	Theory of dynamic analysis	81
8.1.1	Dynamic equilibrium equation	81
8.1.2	Mass matrix	82
8.1.3	Damping	82
8.1.4	Stiffness matrix	84
8.2	Wave theory and wave load model used in the dynamic analysis	85
8.2.1	Stochastic wave theory	85
8.2.2	Design swell model	87
8.2.3	Wajac	88
8.3	Solution methods of the dynamic equilibrium equation	89
8.4	Results of dynamic analysis	92
8.4.1	Estimation of Rayleigh-damping coefficients	92
8.4.2	Estimation of maximum wave height	93
8.4.3	Response due to swell sea	93
8.5	Discussion of results from dynamic analysis	95
9	Concluding remarks	99
10	Recommendations for further work	101
	Bibliography	103
A	Additional information about the SFT for the Digernessund gathered from the technical report	i
A.1	Load factors	ii
A.2	Eigenperiods calculated by the NPRA	iii
B	Section properties	v
B.1	Summary of section properties	v
B.2	Calculation of section properties	vi
B.3	Method for approximation of varying cross-section	viii
C	Curved model	ix
D	Material densities	xiii
E	Reinforcements and PT-cables	xv
E.1	Summary of ordinary reinforcements	xv
E.2	Sketch of reinforcements and PT-cables	xvi

F	Transformed cross-section	xvii
F.1	Summary of transformed cross-section properties	xvii
F.2	Transformed moment of inertia calculations	xvii
F.2.1	Transformed moment of inertia about z-axis	xvii
F.2.2	Transformed moment of inertia about y-axis	xix
G	Additional results from structural analysis	xxi
G.1	Additional static analysis results	xxi
G.1.1	Sensitivity study of current direction in SLS condition.	xxi
G.1.2	Static analysis results for case with specific weight of reinforced concrete $26.5kN/m^3$	xxiii
G.1.3	Static analysis results for alternative ballast cases	xxiv
G.2	Additional eigenvalue analysis results	xxv
G.2.1	Results for straight bridge model	xxv
G.2.2	Results for curved bridge model	xxvi
G.2.3	Additional results from parameter studies with curve height . . .	xxvii
G.2.4	Abaqus eigenvalue analysis with axial compression from PT-cables	xxvii
G.3	Additional dynamic response analysis results	xxx
H	Hand-calculations for checking results from static analysis in Sestra	xxxv
H.1	Selfweight check	xxxv
H.2	Buoyancy check	xxxvi
I	MATLAB script	xxxix
I.1	Script estimating the Rayleigh damping coefficients	xxxix
J	Sesam scripts	xli
J.1	Wajac analysis control file	xli
J.2	Sestra dynamic analysis control file	xliii

List of Tables

- 3.1 Functional requirements summarized. 20
- 3.2 Cross-section properties 22
- 3.3 Material properties for concrete B55-MF40 22
- 3.4 Material properties for reinforcement steel B500NC 22
- 3.5 Material properties for pretension cables Y1860S7 22
- 3.6 Estimated current velocities for the Digernessund. Values taken from [Engseth et al., 2016]. 23
- 3.7 Estimated data for wind induced waves.[Engseth et al., 2016] 23
- 3.8 Estimated data for swell waves.[Engseth et al., 2016] 23

- 4.1 Loads contributing to permanent self-weight for the SFT proposed for the crossing of Digernessund, values collected from [Engseth et al., 2016] 26

- 5.1 Summary of calculated minimum reinforcement 39
- 5.2 Linearly varying ballast fill, section 1 to 5. 43
- 5.3 Constant average ballast fill, for average cross-section. 44

- 6.1 Load combination for ULS max buoyancy 55
- 6.2 Load combination for SLS 56
- 6.3 Comparison of results for the bending moments about y-axis from hand calculations and SESAM. Straight bridge configuration with constant average cross-section is assumed here. 58
- 6.4 Amplification factor for straight bridge configuration with fixed ends and constant average cross-section. 58
- 6.5 Reaction forces, ULS max buoyancy 58
- 6.6 Bending moments and torsion moment, ULS max buoyancy 58
- 6.7 Bending moments, torsion moment, axial forces and reaction forces for base case, SLS. The bending moments include an amplification factors due to compression force from PT-cables. 60
- 6.8 Displacements for base case, SLS. Including amplification factor due to compression force from PT-cables. 60
- 6.9 Calculated maximum compression stresses in concrete σ_c for SLS. The results are given in N/mm^2 and in percent of the compression strength of the base case bridge. 62
- 6.10 Calculated maximum tensile stresses in concrete σ_{cs} for SLS. The results are given in N/mm^2 and in percent of the tensile strength of the base case bridge. 62

6.11	The curve heights used in the parameter study with associated element lengths and total bridge length. The number of elements are 12 for all curve heights.	62
6.12	SLS reaction forces, bending moments and axial forces for different curve heights with the case of a negative current applied to the full length of the bridge.	63
6.13	SLS displacements for different curve heights.	63
7.1	Eigenvalues used in equation 7.1.[Larsen, 2014]	70
7.2	Reduction of eigenfrequency because of axial compression due to PT-cables.	74
7.3	Eigenfrequencies and periods for curved model, varying cross-section, obtained with Sestra and Abaqus. The deviations between the results from the two softwares are also given.	74
7.4	Eigenperiod and frequency for the first mode for base case, including analytically calculated reduction factor due to PT-cables.	75
7.5	Curve heights in-which the order of the first and second horizontal mode shapes changes. f_2 corresponds to the first horizontal natural frequency.	76
8.1	Overview of the sea states investigated in this thesis.	88
8.2	Rayleigh-damping coefficients for different damping ratios.	92
8.3	Estimation of maximum wave height for the given 100 year sea state.	93
A.1	Eigenperiods and frequencies calculated by the NPRA and dr. techn. Olav Olsen.[Engseth et al., 2016]	iii
B.1	Summary of section properties for section 1-5 and average section	v
D.1	Total material densities for section 1 to 5, with linearly varying ballast	xiii
D.2	Total material densities for average section and section 5, with constant ballast	xiii
E.1	Total minimum longitudinal reinforcement areas mm^2 for section 1 to 5	xv
F.1	Calculated transformed moment of inertia and transformed area for section 1 to 5	xvii
F.2	Calculated transformed moment of inertia for average section	xvii
G.1	Bending moments and reaction forces due to net vertical forces, SLS.	xxiii
G.2	Ballast fill percentages for three different ballast cases.	xxiv
G.3	Maximal concrete stress in most critical section with respect to tension.	xxiv
G.4	Vertical (V) and horizontal (H) eigenperiods and frequencies for straight bridge.	xxv
G.5	Eigenperiods and frequencies obtained with Sestra and Abaqus.	xxv
G.6	Convergence test for straight bridge model. D_{an} is the deviation from the analytical calculation results for straight beam.	xxvi
G.7	Analytical results for curved beam, constant cross-section, vertical (V) and horizontal (H) modes.	xxvi
G.8	Eigenperiods and frequencies for curved model, constant cross-section, obtained with Sestra and Abaqus.	xxvii
G.9	Results for the first six modes from parameter study with curve height.	xxvii

G.10 Results for eigenvalue analysis in Abaqus for straight bridge. Results with and without compression from PT-cables are compared. xxviii

G.11 Abaqus results for curved structure subjected to bolt loads. xxix

H.1 Calculation parameters xxxvi

H.2 Maximal bending moments caused by buoyancy xxxvi

Symbols

Symbols

A	Circumference area, used in dynamic analysis	$[m^2]$
A_c	Cross sectional area of concrete	$[m^2]$
A_{kj}	Added mass coefficient	$[\]$
A_p	Cross sectional area of post-tension cables	$[m^2]$
A_s	Cross sectional area of reinforcements	$[m^2]$
A_{SB}	Cross sectional area of solid ballast	$[m^2]$
$A_{SC,y}$	Shear area, y-axis	$[m^2]$
$A_{SC,z}$	Shear area, z-axis	$[m^2]$
A_T	Transformed cross-section	$[m^2]$
A_{WB}	Cross sectional area of water ballast	$[m^2]$
b	Outer width of cross-section	$[m]$
b_2	Inner width of cross-section	$[m]$
B_{kj}	Damping coefficient	$[\]$
c_y	Location of shear center in y-direction, relative to center of gravity of a given section	$[m]$
c_z	Location of shear center in y-direction, relative to center of gravity of a given section	$[m]$
\bar{C}	Horizontal curve height	$[m]$
C_D	Drag coefficient	
C_{kj}	Restoring coefficient	
D	Characteristic cross-section length	$[m]$

E_{cm}	Elasticity modulus concrete	[GPa]
E_p	Elasticity modulus post-tension cables	[GPa]
E_s	Elasticity modulus reinforcement steel	[GPa]
E_{xx}	Greens strain	[]
f_{ck}	Characteristic compressive strength of concrete	[MPa]
f_{ctm}	Characteristic tensile strength of concrete	[MPa]
f_n	Natural frequency	[1/s]
f_m	Amplification factor	[-]
f_{pk}	Characteristic tensile strength of post-tension cables	[MPa]
$f_{p0.1k}$	Characteristic 0.1% tensile strength of post-tension cables	[MPa]
f_v	Vortex shedding frequency	[Hz]
f_{wmax}	Amplification factor	[-]
f_{yd}	Design yield strength of reinforcement steel	[MPa]
f_{yk}	Characteristic yield strength of reinforcement steel	[MPa]
F_C	Ice load	[N]
F_D	Viscous current load	[N/m]
F_j	Hydrodynamic force	[N]
F_W	Wind load normal to structure	[N]
g	Gravitational acceleration constant	[9.81, m/s ²]
h	Outer height of cross-section	[m]
h_2	Inner height of cross-section	[m]
H_M	Estimation of maximum wave height	[m]
H_s	Significant wave height	[m]
i_r	Radius of gyration	[m]
I_t	Torsion moment of inertia about shear center	[m ⁴]
$I_{t,y}$	Transformed moment of inertia about y-axis	[m ⁴]
$I_{t,z}$	Transformed moment of inertia about z-axis	[m ⁴]

I_y	Moment of inertia about y-axis	$[m^4]$
I_z	Moment of inertia about y-axis	$[m^4]$
k	Wave number	$[1/m]$
\mathbf{K}	Global stiffness matrix	
l_k	Buckling length	$[m]$
L_e	Element length	$[m]$
L_{bridge}	Total length of the bridge	$[m]$
m	Total mass per unit length, including mass of the structure and added mass	$[kg/m]$
m_a	Added mass per unit length	$[kg/m]$
\mathbf{M}	Mass matrix	$[\]$
M_{xy}	Bending moment about y-direction.	GPa
M_{xz}	Bending moment about z-direction.	GPa
N	Axial force	$[N]$
N_E	Euler buckling load	$[N]$
P	Axial force in PT-cables	$[N]$
\mathbf{Q}	Vector with external loads	N
R	Radius of horizontal curve	$[m]$
S	Projected area used in wind calculation	$[m^2]$
S_T	Strouhals number	$[\]$
S_y	Static area moment about y-axis	$[m^3]$
S_z	Static area moment about z-axis	$[m^3]$
t_1	Thickness of vertical wall (web)	$[m]$
t_2	Thickness of horizontal wall (flange)	$[m]$
t_3	Thickness of inner part of the cross-section	$[m]$
T	Wave period	$[s]$
T_p	Spectral peak period	$[s]$

T_v	Vortex shedding period	[s]
U_∞	Incident current velocity	[m/s]
U_R	Reduced velocity	[m/s]
$U_{R,IL}$	Reduced velocity for in-line flow	[m/s]
$U_{R,CF}$	Reduced velocity for cross-flow	[m/s]
$U_{T,z}$	Mean wind velocity averaged over a time T at height z above ground	[m/s]
u, v, w	Displacement of the structure in x,y and z-direction.	[m]
W_t	Torsion section modulus about shear center	[m ³]
W_y	Section modulus about y-axis	[m ³]
W_z	Section modulus about z-axis	[m ³]
Greek letters		
α	Rayleigh damping coefficient	[-]
β	Rayleigh damping coefficient	[-]
β_0	Wave propagation direction	[Deg]
λ	Wave length	m
ν	Poisson's ratio	[-]
ρ_a	Mass density of air	[kg/m ³]
ρ_{RC}	Density of reinforced concrete	kg/m ³
ρ_W	Density of seawater	kg/m ³
ρ_{WB}	Density of water ballast	kg/m ³
ρ_{SB}	Density of solid ballast	kg/m ³
κ	Curvature	[]
ω	Wave frequency	[rad/s]
σ_c	Stress in concrete	[N/mm ²]
η	Motion of the structure	[m]
$\dot{\eta}$	Velocity of the structure	[m/s]
$\ddot{\eta}$	Acceleration of the structure	[m/s ²]

Abbreviations

ULS Ultimate limit state

SLS Serviceability limit state

FEM Finite element method

FE Finite element

PT-cables Post-tension cables

SFT Submerged floating tunnel

NPRA Norwegian Public Road Administration (Statens vegvesen)

Chapter 1

Introduction

1.1 Background

The relevance of marine bridges has increased the previous years due to the Norwegian government plans for a renewed route E39. The Norwegian Parliament (Stortinget) has decided to renew route E39 in Norway, between Trondheim and Kristiansand. A part of the plan is to lower the travel time by avoiding ferries, which is done by replacing the ferries by bridges and tunnels. Due to the large spans and depths of some of the fjord-crossings, marine bridges are assumed to be the most suitable solutions for these crossings.

1.2 Objective

Different types of marine bridges are described briefly in this thesis, with focus on structural behaviour and loads acting on such bridges. Both existing marine bridges and future plans for such bridges are reviewed, with reference to the ongoing ferry-free E39 project. The main objective of this thesis is to investigate the structural behaviour of a submerged floating tunnel. That is, both static response due to weight, traffic, buoyancy and current as well as dynamic response due to waves. The material of the floating tunnel is reinforced concrete with post-tension cables. The influence of the PT-cables on the static behaviour, the natural frequencies and mode shapes will also be investigated. Another objective of this thesis is to investigate the effect of increasing height of arc with respect to mode shape and the natural frequencies. In particular, the mode shape and eigenfrequency of the first horizontal mode is of special interest.

Another objective of this thesis is to get more familiar with the software package Sesam, provided by the DNV-GL. Quite some time was spent trying to understand the available programs for hydrodynamic and structural analysis in Sesam. This was done by reading the user manuals corresponding to the respective programs, and by email correspondence with the Sesam support team.

The reader should be familiar with basic hydrodynamics and regular wave theory. Knowledge of concrete structures is also beneficial, but not a demand.

1.3 Limitations

Some limitations of the thesis are listed below.

- The model established in this thesis is based on a feasibility study, and not detailed design, of a SFT for the Digernessund.
- Only the minimum reinforcements in longitudinal direction has been included in the calculations.
- The model established in this thesis does not have a vertical alignment as the original concept for simplicity.
- Nonlinear geometric stiffness effects are not accounted for. The linear analysis program Sesam has been used for analyses.
- The dynamic response analysis is based on swell waves only, which are modeled as regular waves.
- The hydrodynamic coefficients are assumed constant and independent of frequency.

1.4 Structure of the report

This report is divided in two parts. The first part gives a review of existing marine bridges and future plans for such bridges together with load theory. This part also gives a description of the concept for a particular marine bridge, which is analyzed in part two. Part two concerns structural analyses of the particular marine bridge. The structural analyses part is divided into five chapters. The first chapter, chapter 5, gives a description of the finite element model of the SFT. The next three chapters concerns analyses of the finite element model. Chapter 6 concerns static analysis, including theory for static analysis, finite element formulations, load cases and combinations used in the static analysis, results and discussion.

The next chapter, chapter 7, concerns eigenvalue analysis of the SFT. Both analytical solutions and theory of modal analysis are given. Results and discussion of the different configurations of the bridge are also included. Chapter 8 concerns dynamic response analysis. Here, the dynamic behaviour of the SFT is investigated due to regular swell waves. Chapter 9 gives concluding remarks, and chapter 10 gives recommendations for further work. At the end, the bibliography is given. The thesis also include an appendix with more detailed information and results.

Part I

Marine bridges and load theory

Chapter 2

Review of marine bridges

Existing floating bridges and future planes are reviewed in this chapter. Floating bridges have been built for decades for varying purposes. During antiquity, such structures were often used for military operations. Today, floating bridges are of conventional use in the road network.[Lwin, 2000]

Parts of this chapter is taken from the authors project thesis.

2.1 Conventional floating bridges

Existing floating bridges consist of an elevated superstructure of either steel or concrete, supported by floating pontoons. The pontoons can be one large continuous part or several separated ones. For separated pontoons, it is important to ensure that the superstructure has sufficient strength and stiffness to maintain the relative position of the pontoons. The structural system of existing bridges is basically a beam supported by floating pontoons. The pontoons takes advantage of the buoyancy to support the beam.[Lwin, 2000] In addition, the bridge has to carry sideways forces from e.g. wind, waves and current. This has been ensured by either side-anchoring or by building a curved structure. The latter concept is based on the fact that curved structures carry the forces as axial forces and bending moments.[Øderud and Nordahl, 2017]

In Norway, there are two existing floating bridges with separated pontoons, the Bergsøysund bridge (fig.2.1a) and the Nordhordland bridge (fig.2.1b). The Bergsøysund bridge, opened in 1992, has concrete pontoons and a total span of 931 m. The bridge is only connected at the two ends, ie. without side-anchoring. In addition to lightweight concrete pontoons, the bridge consists of a steel truss-work in an horizontal arch.[Riksantikvaren, Hovedkontor, 2008]



(a) Bergsøysund bridge
(Illustration: Kulturminnesok.no,
photographer: Andersen, O. S.)



(b) Nordhordland Bridge
(Illustration: www.broer.no)

Figure 2.1: Existing floating bridges in Norway.

The Nordhordland bridge is a combination of a floating bridge and a cable-stayed bridge. This concept was chosen because of the possibility for a ship channel under the cable-stayed bridge. The floating part consists of a steel box girder and ten concrete pontoons. The cable-stayed bridge is made of concrete, and consists of a 30 meter deep underwater foundation and two 99.3 meter high towers. The total length of the bridge is 1615 meter.[Moe et al., 1995]

One of the concepts proposed for the Sognefjorden crossing, which is a part of the ferry-free E39 project, is a floating bridge (fig.2.2a). The fjord is very deep, and the is 3700 meters wide. A ship channel is placed midway. The concept can be related to that of the Bergsøysund bridge, even though the design is somewhat different. Here, the bridge is connected to the pontoons with columns instead of a steel trusswork as for the Bergsøysund bridge. Because of the deep fjord, it is desired to avoid secondary anchoring systems. The structure is curved, providing horizontal stiffness, and the pontoons are assumed to have high stiffness in the transverse direction of the bridge. To ensure horizontal stiffness, an alternative is to introduce secondary bearings by splitting the railway. [Statens Vegvesen, 2011]



(a) Floating bridge with ship channel mid-ways for Sognefjorden (Illustration: NPRA).



(b) Combined floating bridge and cable-stayed bridge. (Illustration: NPRA)

Figure 2.2: Future plans of floating bridges in Norway.

A concept proposed for the Bjørnafjorden crossing, which also is a part of the ferry-

free E39 project, is a combined floating bridge and cable-stayed bridge, fig. 2.2b. The concept can be related to that of the Nordhordland bridge.[Statens Vegvesen, 2011] The floating part of the bridge is a conventional floating bridge with separated concrete pontoons, and this part is connected to the seabed with mooring lines. As for the Nordhordland bridge, the bridge girder consists of a single steel box. The cable-stayed bridge is supported by an A-shaped tower with a height of 215 m. The total length is approximately 4500 m.[Project group, 2016]

2.2 Suspension bridges

To describe floating suspension bridges, a brief description of traditional suspension bridges is first given. The suspension bridges with TLP technology, cable-stayed bridges and cable-stayed bridges with TLP-technology are then described.

2.2.1 Traditional suspension bridge

The first suspension bridge in Norway, with steel-wires as suspension cables, was built in 1904 (Gulsvik bridge).[Olsen, 2008] Today, Hardanger bridge is the longest suspension-bridge in Norway.[broer.no, 2018] The main bearing in suspension bridges are the cables, which carry axial loads. The towers usually have a height, from the lowest points of the cables to the tower top, which is approximately 1/10 of the span. The suspension cables are anchored to the ground at the two ends of the bridge.[Olsen, 2008]



Figure 2.3: Picture of multi-span suspension bridge Chacao Bridge. [KAA, 2016]

A few suspension bridges with multi-spans have been constructed in China, one is under construction in Chile (fig.2.3) and several projects have been carried out. The fundamental challenge with this solution is that if the bridge is loaded over one span, the central tower will lean relatively freely towards the loaded span. This is because the cables in the other main span provide little horizontal resistance to movements of the tower top leading to large vertical displacements in both main spans. For the Chacao Bridge, the stability has been achieved by a central rigid four-legged A-shaped tower that prevents the tower top from large horizontal displacements. The TLP-connections also reduce the vertical displacements of the bridge spans as well.[KAA, 2016]

2.2.2 Suspension bridge with TLP technology

The idea of floating suspension bridges is to combine traditional suspension bridge with offshore solutions, to reduce the span of long crossings. Reduced span is desired, because both the costs and aerodynamic challenges increase with increased span. [Statens Vegvesen, 2011] Because of the high depths of the Norwegian fjords, TLP-foundations are considered possible solutions for floating towers. This kind of suspension bridge has never been built before, but has been proposed for the crossings over Bjørnafjorden, Sulafjorden and Sognefjorden. [NPRA, 2016] The first one will be the reference case here, because it is the most investigated for now.

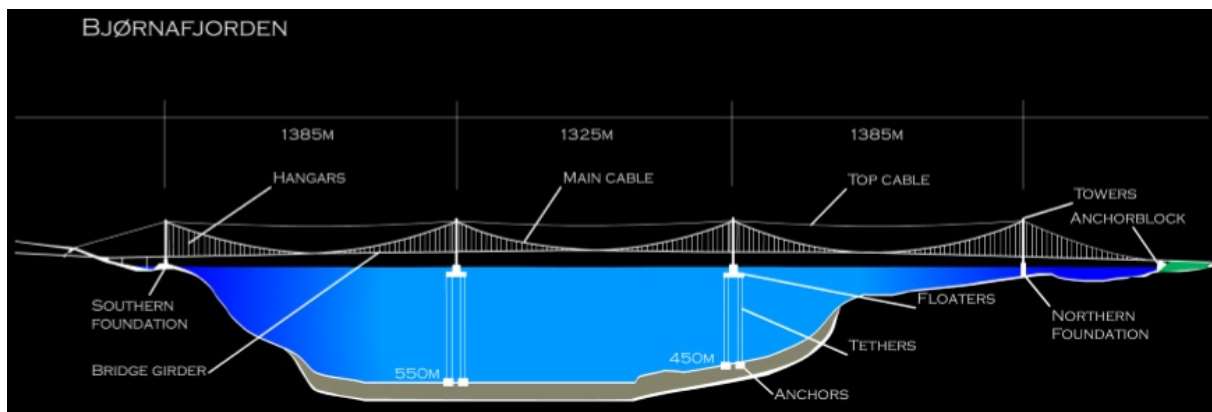


Figure 2.4: Concept overview for Bjørnafjorden (Illustration:[NPRA, 2016]).

The total length of the Bjørnafjorden crossing is approximately 5 km. The proposed suspension bridge has four TLP-foundations, three main spans and side spans at each end (fig.2.4). The TLP-foundations are made of concrete. The hull, either made of steel or concrete, can be connected to seabed with tensioned tethers (fig.2.6b) and suction anchors, which provides high stiffness in the vertical direction and for rotation about the two horizontal axes. The TLP-foundations provide buoyancy, which outweighs the gravity of the structure and introduce permanent tension of the tethers. In addition, they are designed to minimize heave, roll and pitch motions. The tension in the tethers, suspension cables and top cables provides a restoring force for the transverse displacements. Additional stiffness is added in the longitudinal direction by a top cable, due to the flexible supports at the central towers. This is to prevent large movements of the tower top. [KAA, 2016]

However, a floating object like a TLP-foundation will be susceptible to motions like heave, roll and pitch. The tethers of a TLP will eliminate these and create a steady-state support condition. The tethers also restrain horizontal motions and will recover the neutral position after movements caused by environmental loads. [KAA, 2016] The global stiffness, provided by the tethers, suspension cables and top cables, is not that high as if the central pylons were fixed/not floating. To improve this, it was found efficient to integrate the floating pylon with the bridge deck. By this, they are monolithically connected, meaning that all degrees of freedom are transferred between them. [KAA, 2016]

2.3 Cable-stayed bridges

2.3.1 Traditional cable-stayed bridge

Modern cable-stayed bridges, which also are a type of suspension bridges, were developed in the 1950s. The first modern cable-stayed bridge in Norway was the Stavanger city bridge, which opened in 1979.[Øderud and Nordahl, 2017] The Helgelandsbrua, shown in fig 2.5, opened in 1991 and is 1065m long. The main span is 425m.[Broer.no, 2017]

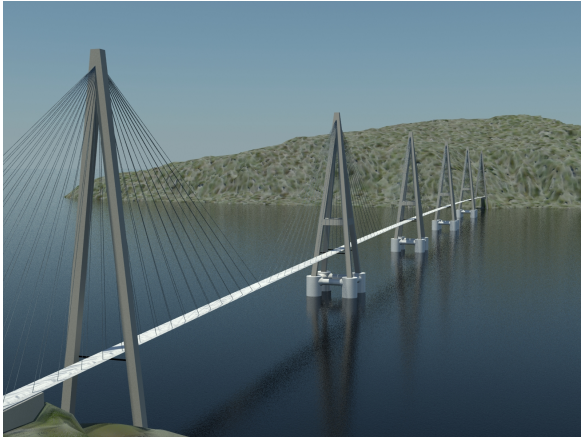


Figure 2.5: Picture of the traditional cable-stayed bridge Helgelandsbrua.(Picture: broer.no, 2017)

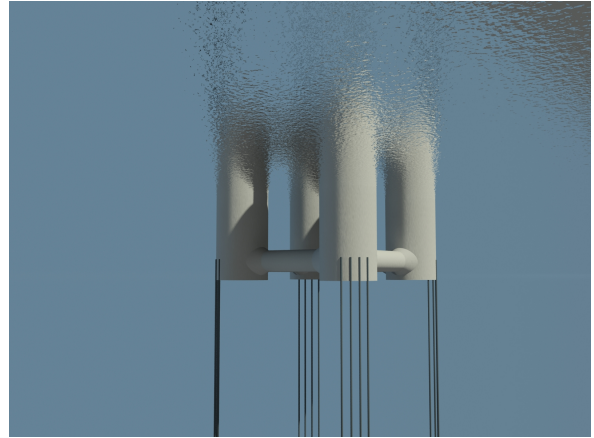
Cable-stayed bridges are different from suspension bridges described in 2.2.1. The carriageway-girder is carried by straight, tilted steel trusses connected to a tower. Contrary to other suspension bridges, the height of the tower is usually $1/5$ of the length of the span.[Øderud and Nordahl, 2017]

2.3.2 Cable-stayed bridge with TLP technology

Another concept proposed for the project ferry-free E39 is a cable-stayed bridge with TLP-foundations. A cable-stayed bridge, fig. 2.6a, supported by TLP foundations, has never been built before. The idea is to combine the common cable-stayed bridge with offshore solutions, ie. TLP foundations. The intention is to reduce the large spans of the crossings by dividing the bridge in multiple spans, in the same way as for the case for floating suspension bridge. See section 2.2.2 for more details about TLP-foundations.



(a) Cable-stayed bridge with floating pontoons. The pontoons are anchored by bars. (Illustration: Myhre, A. J, NPRA)



(b) Anchoring of cable-stayed bridge with floating pontoons, seen from the water (Illustration: Myhre, A. J, NPRA)

Figure 2.6: Cable-stayed bridge with pontoons.

2.4 Submerged floating tunnel

A submerged floating bridge has never been built before. However, the concept is old and has been studied in Norway as well as other countries for years. The first SFT solution for a fixed link in Norway was established for the crossing of Karmsundet (1947). As the years past by, the concept was proposed for e.g. crossing of Høgsfjorden, Hardangerfjorden and other crossings.[NPRA, 2012] In the recent years, it has been proposed for crossings in the ferry-free E39 project, including the Digernessund crossing. The latter will be used as reference later in this assignment.

A submerged floating bridge is a structure floating beneath the sea surface. There exists several solutions for providing buoyancy and anchoring. The two main solutions are tether support and pontoon support, see fig.2.7. The different concepts that has been studied includes many different cross-sections and designs, e.g. circular cylinders, rectangular boxes, single or double.

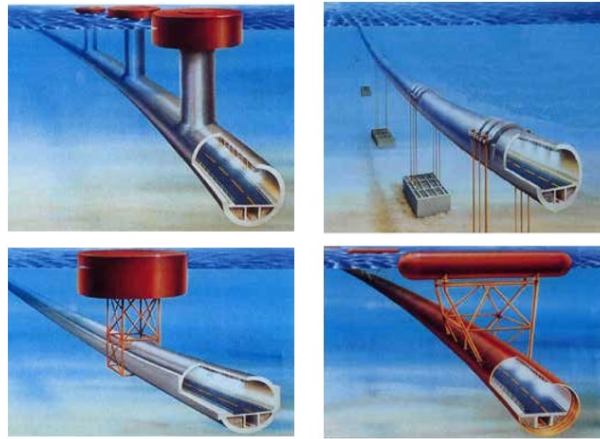


Figure 2.7: Concept overview for Høgsfjorden (1980s)
[NPRA, 2012]

The Norwegian Coastal Administration (Kystverket) sets the requirements for clearance for ship channels. To allow for the largest cruise ships of today, the requirement for vertical clearance is set to 75m.[Kystverket, 2014] Thus, this requirement set limits to the height of bridges crossing Norwegian fairways, and submerged floating tunnels can thus be a good alternative to avoid high bridges.

2.4.1 SFT with tether support

Tethers connected to the seabed provide both vertical and horizontal stiffness (fig.2.8). The SFT with tethers has excessive buoyancy so that the tethers are in tension at all times. The tethers are anchored by e.g. gravitational anchors to transfer the tension forces to the ground. [Statens Vegvesen, 2011]

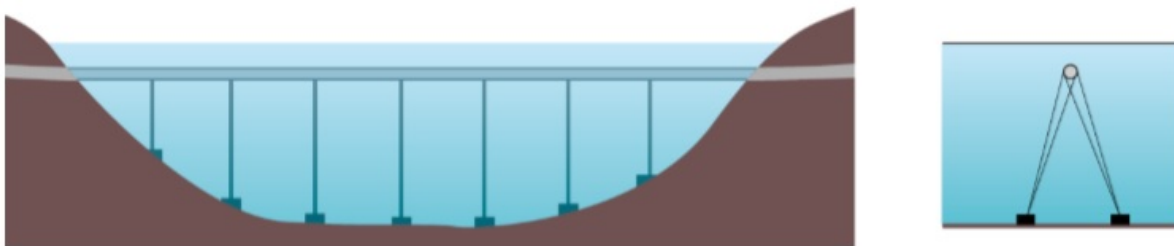


Figure 2.8: Submerged floating tunnel with tether support. (Illustration: NPRA, [Statens Vegvesen, 2011])

This concept is limited to certain depths. However, for moderate depths, this solution is highly relevant. This solution was in fact considered the best and safest solution for submerged bridges after the development of the Høgsfjord crossing, especially at locations that may be exposed to high waves.[Statens Vegvesen, 2011] This concept was also proposed for some of the crossings in the ferry-free E39 project, including Sulafjorden and Digernessund. Both crossings are under research.

2.4.2 SFT with pontoon support

The main idea of using pontoons is to provide buoyancy and stiffness in the vertical direction. To provide horizontal stiffness, the bridge is horizontally curved.

[Statens Vegvesen, 2011] The pontoons consists of either steel or concrete, and can have different shapes and connections to the bridge (fig.2.7).[NPRA, 2012]

In the case of a single bridge, the structure may need additional side-anchored bars providing enough stiffness against transverse movements of the bridge (fig.2.9). For shorter spans, smaller than approximately 2km, the additional side-anchored bars may be redundant. In the case of a double bridge the two bridges will be parallel and connected (fig. 2.10). The connection of the two bridges, together with the fact that the bridge is curved, provides horizontal stiffness. [Statens Vegvesen, 2011]

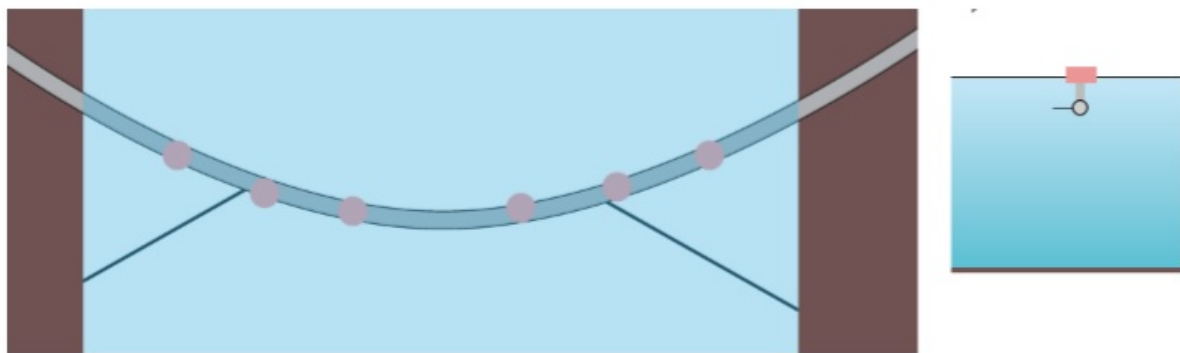


Figure 2.9: Side-anchored bridge with pontoons.[Statens Vegvesen, 2011]

Some of the drawbacks using pontoons are that the pontoons will be visible on the free surface, they can be a hinder for ship traffic and exposed to ship collisions. Another fact, that can be a challenge, is that the concept has to account for tidal variations of the supports. [Engseth et al., 2016] In addition, waves can be of great importance for the movements of the pontoons.[Statens Vegvesen, 2011]

However, there is an big advantage using pontoons for submerged floating bridges. In the case of very deep fjords and crossings, like Sognefjorden, it is not considered feasible to have tethers connected to the seabed. Using pontoons, this problem is avoided.[Statens Vegvesen, 2011] This concept has been proposed for the deepest crossings of the ferry-free E39 project, including Sognefjorden and Bjørnafjorden.

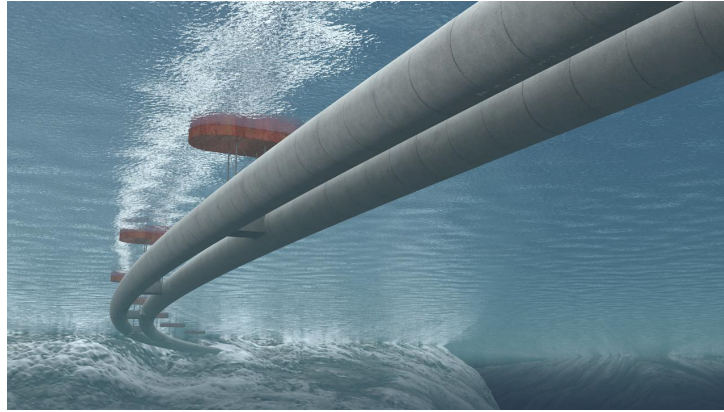


Figure 2.10: Submerged floating tunnel with pontoon support.(Illustration: NPRA)

2.4.3 Free-spanning SFT

Another solution for submerged bridges, proposed by dr. techn. Olav Olsen for the crossing of Digernessund (fig.2.11), is a single bridge without any tethers or pontoons. This solution was proposed because the span of this crossing is relatively small (690m). The drawback is that the solution results in high forces transferred to the abutments. However, this solution was considered relevant because of small waves and moderate current in the strait. The proposed bridge is a reinforced concrete structure with post-tension cables. Several cross-sections have been evaluated, both circular and rectangular. See fig.2.12 for illustration of three cross-section proposed for the free spanning concepts. The bridge has both horizontal and vertical alignment resulting in a curved structure.[Engseth et al., 2016]

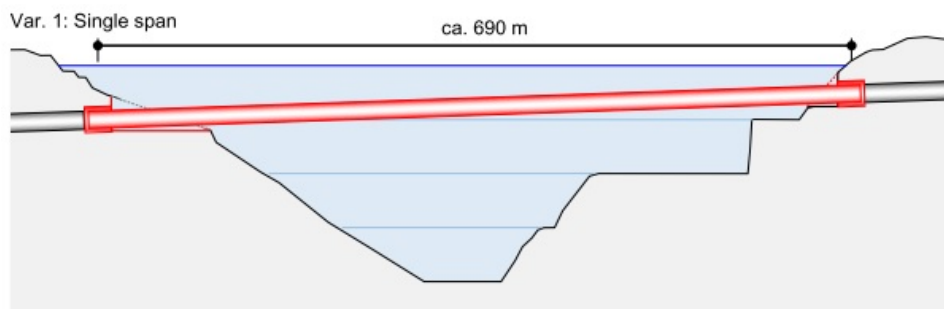


Figure 2.11: Concept without intermediate support proposed for crossing of Digernessund (Illustration: NPRA/dr. techn. Olav Olsen, [Engseth et al., 2016])

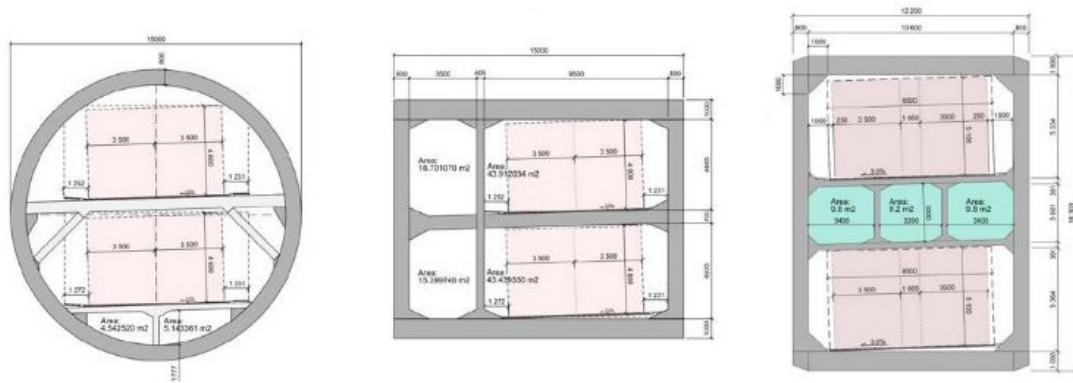


Figure 2.12: Three different cross-sections proposed for the free-spanning concept for the Digernessund. Illustrations:[Engseth et al., 2016]

2.4.4 Combined SFT and floating bridge

The main reason for combining a floating bridge and a submerged floating tunnel is to provide a ship channel. Four different concepts will be presented in the following.

Y-shaped SFT combined with floating bridge

A concept proposed for the crossing of Sognefjorden is given in fig. 2.13. The concept consists of a floating bridge resting on pontoons, connected to two submerged floating tunnels making a Y-shape. The SFTs are connected to the seabed with tethers, providing vertical stiffness. The Y-shape of the submerged part of the bridge provides horizontal anchoring and separation of the submerged floating tunnels towards separate rock tunnels at the landfalls.[Statens Vegvesen, 2011]

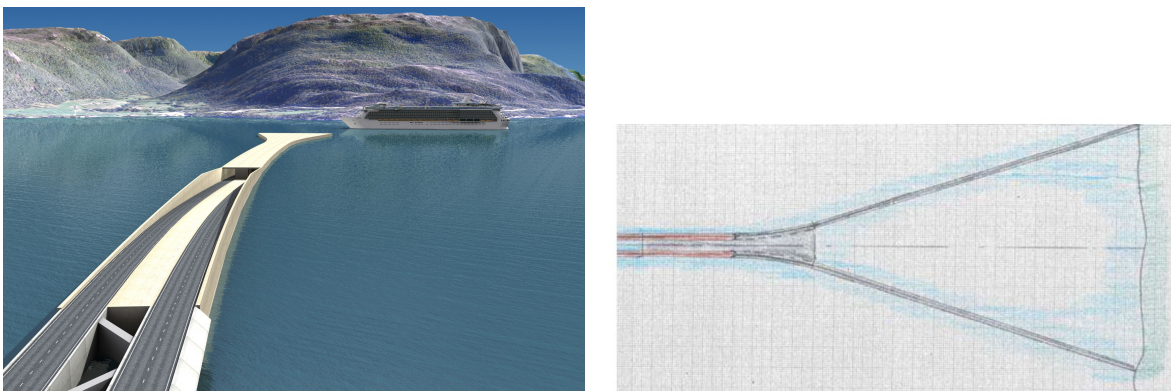


Figure 2.13: Y-shaped concept for a combination of two submerged floating tunnels and a floating bridge.[Statens Vegvesen, 2017, Statens Vegvesen, 2011]

Concept for the crossing of Rovdefjord



Figure 2.14: Illustration of Rovdefjord bridge [Snøhetta, 2016b]

Rovdefjord bridge will be an important link between the southern Sunnmøre and the outer parts of Nordfjord, at the west coast of Norway. The first conceptual ideas for a bridge crossing the Rovdefjord were launched in the 1980s. In 2011, the foundation Rovdefjordsambandet AS was established to investigate the possibilities for a ferry-free crossing of Rovdefjord. The companies Reinertsen AS, dr. techn Olav Olsen, Snøhetta and SINTEF have, on behalf of Vanylven Utvikling AS, developed a concept for crossing the Rovdefjord with a SFT (fig.2.14). In 2016, the local council Sande kommune, approved the municipal sector plan for the Rovdefjord bridge. [Sande kommune, 2016] However, the bridge has not been built yet.

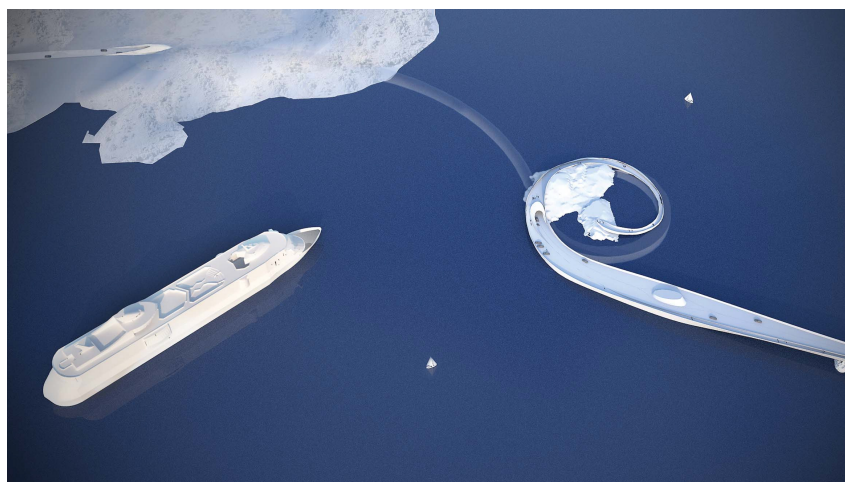


Figure 2.15: Illustration of Rovdefjord bridge showing the spiral connection between the SFT and the floating bridge at Saudeholmen. [Snøhetta, 2016b]

The proposed bridge concept has a total length of 3500 m and consists of a rock tunnel, a floating bridge of length 1500 m and a SFT of length 230 m. The floating bridge, which is curved in the horizontal plane, is a steel girder connected to 14 concrete pontoons. The floating bridge is further connected to the SFT by a spiral culvert at a small

island called Saudeholmen, fig. 2.15. The SFT is curved in the horizontal plane, consists of concrete, and has a circular cross-section.[Sande kommune, 2016] The SFT has no intermediate supports and is thus supported only by its buoyancy and the connections at the two ends.

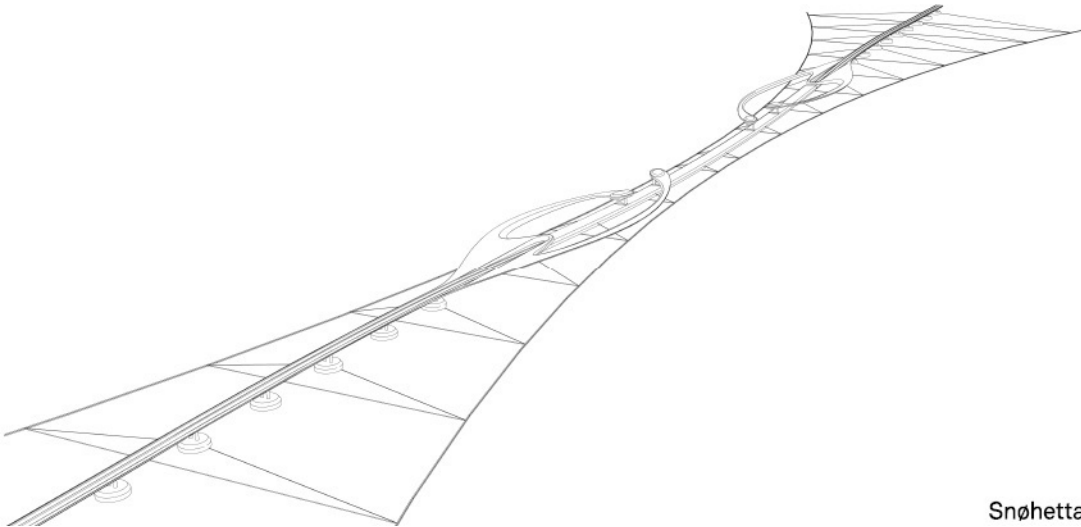
Artificial seabed



Figure 2.16: Illustration of Artificial seabed concept. [Snøhetta, 2016b]

An ongoing research project called Artificial seabed started in 2014 and is a collaboration project between the former Reinertsen, Dr. Techn. Olav Olsen, Snøhetta, Sapa, Hydro, Deep Ocean Group and Sintef. The project is supported by The Research Council of Norway.[Snøhetta, 2016a] The concept (fig. 2.16) is a mooring system for a combined floating bridge and SFT, which enables a flexible placement of the SFT independent of the water depth on site and sea bottom conditions. The idea is a submerged anchoring system which provides lateral stiffness of a slender bridge through side mooring. The anchoring system consists of two pretensioned bundles of steel pipes across the fjord. The bundles consist of three steel pipes, which are neutrally buoyant, submerged to about 35 meters and horizontally curved (fig. 2.17). Transverse steel pipes connect the two bundles making the total anchoring system a stiff horizontal frame.[Reiso et al., 2017]

A crossing which has been evaluated for the Artificial seabed concept is the Bjørnafjord. For this particular crossing, the distance between the bundles at the bridge ends are 800m, while the distance at mid fjord is 80m. Both the floating bridge and the SFT are connected to the Artificial seabed by mooring. Transverse loads are transferred to the submerged anchoring system, and then transferred further to the abutments as axial forces. The concept allows for reduced span due to side mooring, compared to a horizontally curved end-moored concept. Another advantage is that the ship passage can be optimally placed with respect to the ship traffic. However, the concept require large submerged mooring chambers. These chambers can be accessed by land.[Reiso et al., 2017]




Snøhetta 

Figure 2.17: Illustration of the artificial seabed, mooring system, pontoons, ship barriers and the combined floating bridge and SFT bridge. [Snøhetta, 2016b]

Chapter 3

Developed concept of a SFT for the Digernessund

The Digernes strait is one of the crossings along the route E39, with an existing suspension bridge called Stordbrua. This bridge is a part of the triangle link connecting Haugaland and Sunnhordaland, and consists of the 677 m long Stordbrua and a 7.8 km submerged tunnel crossing the Bømlafjorden meeting at a small island named Føyno. Spatial restrictions at Føyno resulted in a road alignment with a gradient which does not meet the requirement for the new E39. The requirement is a maximum gradient of 5%, and two lanes per driving direction. Therefore, alternative modifications of the link have been considered.[Engseth et al., 2016]

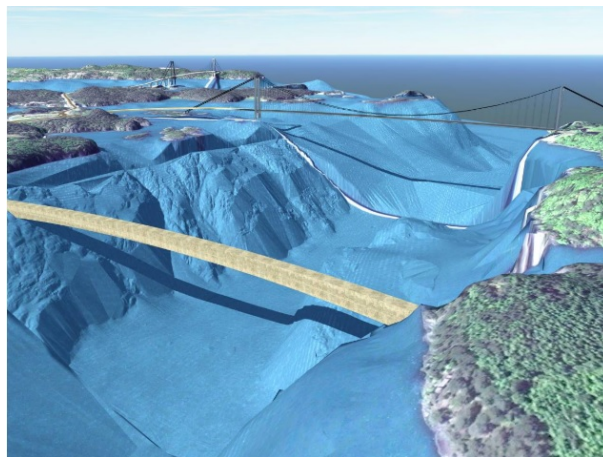


Figure 3.1: Illustration of the proposed SFT for the Digernessund. (Illustration:[Engseth et al., 2016])

The submerged tunnel over the Bømlafjorden has a minimum elevation of -260m below the free surface, which govern the high gradient between the Stordbrua and the submerged tunnel. A submerged floating tunnel bridge is considered a suitable alternative to existing bridges requiring high gradients accessing roads, like the crossing of Digernes strait. On behalf of the NPRÅ, Dr. techn. Olav Olsen has prepared a feasibility study for a SFT for this crossing (fig.3.1).[Engseth et al., 2016] This thesis takes advantage of the work done by dr. techn. Olav Olsen in the feasibility study.

3.1 Functional requirements

Some functional requirements for the SFT are given in tab. 3.1. According to [Vegdirektoratet, 2015] the crossing shall have a design life of 100 years. The NPRA has advised the limiting values of vertical and horizontal deflections of $L/350$ and $L/200$ respectively. For horizontal deflections, L represents the total length between the abutments, while for vertical deflections, L represents the total length between vertical supports. Further, NPRA has advised maximum accelerations as summarized in tab.3.1 to ensure pedestrian comfort.[Engseth et al., 2016]

Table 3.1: Functional requirements summarized.

Parameter	Requirement
Design life	100 years
Horizontal deflection	$L/200$
Vertical deflection	$L/350$
Horizontal vibration	0.3 m/s^2
Vertical vibration	0.5 m/s^2

The bridge girder should ensure water tightness in operation and temporary conditions. The design criteria for serviceability limit state is zero crack width, $w_k = 0$ and membrane compression in the longitudinal direction in the outer fibre. There is also restrictions with respect to the minimum compression zone height. For the ultimate limit state and accidental limit state, the strains in the PT-cables and reinforcements are limited to the elastic region. Hydrostatic stability should also be ensured in accordance with requirements in the DNV-OS-C301.[Engseth et al., 2016]

3.2 Global dimensions

The technical report [Engseth et al., 2016] specifies parameters for a SFT for the crossing of the Digernes strait. The total length of the bridge model is 690m, but in the conceptual design $L_{bridge} = 600\text{m}$ is used for modelling and analysis. The bridge has an alignment in both horizontal and vertical direction. The radius of curvature is 1850m for the horizontal alignment, and the radius of curvature in vertical direction is 14km. The depth of the bridge varies from -50m to -40m . Several bearing systems have been proposed in the feasibility study including free span, tether support, column support and pontoon support.[Engseth et al., 2016]

3.3 Cross-section

Several cross-sections have been proposed in the feasibility study, both circular and rectangular. One of the cross-section proposed by dr. Techn Olav Olsen for the free span solution is given in figure 3.2. In the following, this will be referred to as the

original cross-section. A varying cross-section is proposed for separation of carriage-ways at the landfalls. The cross section height varies over a length of 200m out from the two ends. The cross-section to the right (cross-section b) in Fig. 3.2 is situated at the landfalls while the cross-section to the left (cross-section a) is situated at the mid-span.[Engseth et al., 2016]



Figure 3.2: Cross sections a and b, free span bridge [Engseth et al., 2016].

The cross-section consists of two sections for traffic tunnels and three ballast chambers. The height variation is added to the ballast chambers. The traffic tunnels have the same width as the rock tunnels connected to the SFT, which is a T10.5 tunnel profile. The free height of the traffic tunnels is 5.1m, including requirements, safety margin, tolerances, increased pavement thickness and room for fire protection and signaling.[Engseth et al., 2016] Cross-section dimension can be found in fig 3.2 and some of the properties are summarized in tab.3.2.

Table 3.2: Cross-section properties

Parameter	Cross-section a	Cross-section b
Top- and bottom thickness (m)	1	1
Web thickness (m)	0.8	0.8
Width (m)	12.2	12.2
Total height (m)	16.3	18.8
Concrete area (m^2/m)	57.8	61.8
Ballast chambers		
Ballast compartment area (m^2)	28.8	53.8
Ballast fill percent (%)	60.4	79
Ballast fill (m^2)	17.28	42.5

3.4 Materials

The materials suggested for the bridge girder are concrete B55-MF40 with reinforcement steel B500NC. It is also suggested to post-tension the bridge with post-tension cables, 6-31 stand Y1860.[Engseth et al., 2016] Material properties for these materials are given in tables 3.3, 3.4 and 3.5. Information about the materials B55-MF40 and reinforcement steel B500NC are gathered from [NS-EN1992, 2004]. Information about the PT cable material is gathered from [Johansen, 2017].

Table 3.3: Material properties for concrete B55-MF40

Parameter	Unit	Concrete B55-MF40
Elasticity modulus E_{cm}	GPa	38
Poisson's ratio ν	–	0.2
Characteristic compr. strength f_{ck}	MPa	55
Characteristic tensile strength f_{ctm}	MPa	4.2

Table 3.4: Material properties for reinforcement steel B500NC

Parameter	Unit	Steel B500NC
Elasticity modulus E_s	GPa	200
Poisson's ratio ν	–	0.3
Characteristic yield strength f_{yk}	MPa	500
Design yield strength f_{yd}	MPa	434

Table 3.5: Material properties for pretension cables Y1860S7

Parameter	Unit	Y1860
Elasticity modulus E_p	GPa	195
Characteristic tensile strength f_{pk}	MPa	1860
Characteristic 0.1% tensile strength $f_{p0,1k}$	MPa	1640

3.5 Environmental conditions on site

3.5.1 Current

The current velocities estimated by the NPRA are given in table 3.6. These values are gathered from [Engseth et al., 2016], where it is stated that the estimates are coarse and probably conservative. The deep water current velocity is used at the depth of the SFT.

Table 3.6: Estimated current velocities for the Digernessund. Values taken from [Engseth et al., 2016].

Type of current	Current velocity (m/s)
Surface current	2.5
Deep water current	1.0

3.5.2 Wave

The data for wind sea and swell sea are estimated by the NPRA and represented in tab. 3.7 and tab.3.8 respectively. These values are gathered from [Engseth et al., 2016].

Table 3.7: Estimated data for wind induced waves.[Engseth et al., 2016]

Direction	Waves form east 105°-125°		Waves from west 280°-310°	
	H_s (m)	T_p (s)	H_s (m)	T_p (s)
Return period (years)				
10	1.08	3.1-4.3	0.96	2.9-3.8
100	1.29	3.3-4.7	1.14	3.2-4.0
10000	1.62	3.7-5.2	1.42	3.5-4.5

Table 3.8: Estimated data for swell waves.[Engseth et al., 2016]

Direction	120°-140°	
Return period (years)	H_s (m)	T_p (s)
100	0.1	14

Chapter 4

Loads acting on marine bridges

This section describe loads acting on marine bridges in general and then relate them to the SFT proposed for crossing of Digernessund. Most of the theory is taken from the handbook N400 "Bruprosjektering", which is a handbook regarding design rules for bridges, established by NPRA.

Loads acting on marine bridges can be divided into three categories, permanent loads, variable loads and accidental loads. Permanent loads are assumed constant in the time-interval considered, and includes self-weight, buoyancy and permanent ballast and equipment. Variable loads vary in time and include traffic loads, environmental loads, variable ballast and equipment and loads affecting the bridge in temporary phases like installation and fabrication. Accidental loads are loads due to accidents or abnormal events. [Vegdirektoratet, 2015]

4.1 Permanent loads

4.1.1 Self-weight and buoyancy

Self-weight is the weight of all permanent parts of the structure. That is, calculated weight of the structure, permanent solid ballast, permanent water ballast, permanent wearing layer, permanent equipment and buoyancy of the structure. There are also variable permanent self-weights meaning weight of wearing layer, curb stones, fire protection, fans, cables, ducts, signals, call stations and illuminations. Variable free self-weight includes loads that may be removed, including weight of marine growth, water absorption of the structure and solid ballast, dust accumulation, movable ballast, variable wearing layer and replaceable equipment.[Engseth et al., 2016]

Buoyancy can be determined based on net structural dimension and the mean sea water level. Specific weight of water can be assumed $9.955kN/m^3$, in accordance with [Engseth et al., 2016] and [Vegdirektoratet, 2015].

For the SFT proposed for the crossing of Digernessund, the values in tab.4.1 are assumed for the relevant permanent weights:

Table 4.1: Loads contributing to permanent self-weight for the SFT proposed for the crossing of Digernessund, values collected from [Engseth et al., 2016]

Load	Value	Comment
Reinforced concrete, specific weight	25 kN/m^3	
Solid ballast, specific weight	19 kN/m^3	
Water ballast, specific weight	9.81 kN/m^3	Assuming water density 1000 kg/m^3
Fire protection	8 kN/m	Assuming 40 mm layer with specific weight 5 kN/m^3
Wearing layer	34 kN/m	Assuming 80 mm permanent layer, 2 kN/m
Curb stones	20 kN/m	Assuming 150 mm curb
Fans	0	Assuming no need for fans in 500m long tunnel section
Cables	0.07 kN/m	Assuming 10 copper cables with $\varnothing 20$ diameter
Signals	0.1 kN/m	Assuming 1000 kg per 100m
Call stations	0.01 kN/m	Assuming a 100 kg call station every 200 m
Illumination	0.08 kN/m	Assuming 100kg every 25 m

Marine growth depends on the outer perimeter of the bridge, and is calculated based on wet surface. For depths above 12m, assume that the weight due to marine growth is 235 N/m^2 . Water absorption in concrete and solid ballast is assumed 1% of the volume. Weight of dust is included in the variable asphalt thickness and therefore assumed zero. Relocatable water ballast is not accounted for in this project. However, it is a requirement that the ballast system has capacity to increase and decrease. Variable wearing layer is assumed 40 mm asphalt, either added or removed, corresponding to 17 kN/m . Uncertainties in measured permanent weights in dock are added as a load factor of 1%. Tolerance of 15% is added as load factor for variable permanent self-weights. Variable free self-weights are added with a load factor of 1.35%. [Engseth et al., 2016]

4.1.2 Traffic load

Traffic loads are given in NS-EN-1991-1-2. For influence lengths above 500 m the load model is specified in "NA-rundskriv 07/2015". The latter will be used for the SFT proposed for Digernessund. In the load model given in "NA-rundskriv 07/2015", all traffic lanes are loaded with 9 kN/m simultaneously. Line load per driving direction, for two lanes, is then 18 kN/m . Thus, a total of 36 kN/m for both directions.[Engseth et al., 2016]

4.2 Environmental loads

4.2.1 Tide

For marine bridges with structural members near or above the free surface, variations in the sea level have to be accounted for. According to chapter 5.4.4.2 in N400, tidal variations should be accounted for when calculating current and wave heights for both the low and high tide. If the current from tidal variations is significant, this should be accounted for in the calculations of wave loads.[Vegdirektoratet, 2015]

Tidal variations and the influence of tide on the environmental loads are neglected for the free-spanning SFT proposed for the Digernessund due to the submergence to 50 meters.

4.2.2 Ice and snow

Snow loads are calculated according to NS-EN 1991-1-3. The procedure for calculating ice loads is given in chapter 5.4.7 in N400. Ice loads from drifting ice are assumed to act in the most unfavourable level between LAT and HAT. The load from a flat layer of drifting ice can be calculated according to the procedures stated in 5.4.7 in N400. Dynamic response due to ice-breaking should be investigated if the displacement of the structure due to the ice-breaking is higher than 10 mm.[Vegdirektoratet, 2015]

Horizontal ice loads due to fixed layers of ice are calculated as an uniform distributed load, and can be calculated according to the procedures in 5.4.7 in N400. [Vegdirektoratet, 2015] If the sea level changes, the ice loads from fixed layers of ice get a vertical component with a maximum magnitude of 1/3 of the horizontal ice load.[Vegdirektoratet, 2015]

Ice and snow loads are only relevant for marine bridges with structural parts near or above the mean sea level. Thus, these loads are not accounted for in the study of a free-spanning SFT for the Digernessund.

4.2.3 Current loads

According to N400, calculation of current loads should be based on measurements or numerical simulations for the specific site. As a minimum, three profiles should be investigated: uniform distributed current velocity over the whole bridge length, uniform distributed current velocity over a mid-section of the bridge and a shear current with uniform current velocity. Methods for calculating current loads for bridges are given in DNV-RP-C205 and N-003.[Vegdirektoratet, 2015]

When a current flow past a structure flow, separation may occur, depending on Reynolds number. Due to instabilities, asymmetric wake regimes occur and the consequence is vortex shedding. Vortex shed from the structure results in oscillatory forces acting on the body in both lift and drag direction. The oscillatory forces may cause resonance problems, referred to as vortex-induced resonance vibrations.[Faltinsen, 1990] In the

following, the calculation model for viscous drag force caused by cross-flow current and vortex induced vibration will be described.

Viscous drag force

The viscous current load can be generalized for slender structures into a mean force per unit length (eq.4.1):

$$F_D = \frac{1}{2} \rho_w C_D D U_\infty^2 \quad (4.1)$$

where D is characteristic cross-section length, here corresponding to the height of the tube, U_∞^2 is the incident current velocity and C_D is the drag coefficient. The latter has to be empirically determined.[Faltinsen, 1990]


4. Rectangle with rounded corners		L/D	R/D	C_D	L/D	R/D	C_D
	0.5	0	2.5	2.0	0	1.6	
		0.021	2.2			1.4	
		0.083	1.9			0.7	
		0.250	1.6			0.4	
		1.0	1.2			0.29	
	1.0	0	2.2	6.0	0.5	0.89	
		0.021	2.0			0.29	
		0.167	1.2				
		0.333	1.0				
$Re \sim 10^5$							

Figure 4.1: Drag coefficient from DNV-RP-C205 (Illustration: NPRA/dr. techn. Olav Olsen, [Engseth et al., 2016]).

For the SFT proposed for the Digernessund, C_D may be determined using DNV-RP-C205. For the cross-sections given in sec. 3.3, C_D can be approximated as 1.0 with reference to fig.4.1. Assuming a current velocity of 1.0 m/s, the corresponding viscous drag force is 7.6 kN/m.[Engseth et al., 2016]

Vortex induced vibrations

Resonance effect caused by vortex-induced vibrations occurs if the vortex shedding period is sufficiently close to the eigenfrequency of the structure. The phenomenon is called lock-in, meaning that the vortex shedding frequency f_v locks onto the natural frequency. For a circular cylinder, the vortex shedding period T_v can be expressed by the Strouhal number (eq. 4.2). The reduced velocity, $U_R = U_c / (f_n D)$ can be used to indicate if VIV resonance may be a problem. f_n represents the natural frequency of the structure, D is the characteristic length and U_c is the incoming current velocity. [Faltinsen, 1990]

$$T_v = \frac{1}{St} \frac{D}{U_c} \quad (4.2)$$

According to [Engseth et al., 2016], the Strouhals number for a rectangular can be assumed 0.15. D is the characteristic dimension, assumed 15m, and U_c is the incoming

current velocity, assumed 1 m/s. Thus, the vortex shedding period is calculated 100s for the SFT.

According to [Engseth et al., 2016], the DNV-RP-F105 give general onset criteria for cross flow and in-line flow vibrations for current induced vibrations. Cross-flow vibrations has onset at $U_R = 2.0$, while in-line vibrations has onset at $U_R = 1.0$. The reduced velocity for cross-flow and in-line flow, using the eigenfrequency for the first mode, is calculated in the following.

$$U_{R,IL} = \frac{U_c}{f_n D} = \frac{1.0m/s}{0.12s^{-1} * 12.2m} = 0.66m/s \quad (4.3)$$

$$U_{R,CF} = \frac{U_c}{f_n D} = \frac{1.0m/s}{0.12s^{-1} * 18.8m} = 0.49m/s \quad (4.4)$$

Thus, based on the onset criteria from DNV-RP-F105, both cross-flow and in-line flow will not cause vortex induced vibrations.[Engseth et al., 2016]

4.2.4 Wind loads

Wind is a time-varying, three-dimensional and random phenomenon consisting of a mean component and a fluctuating (wind gust) component. The mean component decrease with reduced distance to the ground, while the fluctuating component is approximately constant with respect to the distance to the ground.[Myrhaug, 2006] External wind loads are relevant for the bridge types which are above or partly above the free surface. Internal wind loads may also act on internal surfaces of open structures, like SFT. Different design codes provide procedures for calculation of wind loads on structures, like DNV-RP-C205 and NS-EN-1991-4:2005+NA:2009. The first of the two is used in the feasibility study of a SFT for the Sognefjord, [Statens Vegvesen, 2011], while the latter standard is referred to for calculation of wind loads on bridges by N400 [Vegdirektoratet, 2015]. Both static response and resonant response, in the case of excitation close to natural frequencies, due to wind loading should be investigated.[DNV-GL, 2010b]

According to DNV-RP-C205 [DNV-GL, 2010b], the wind load component acting normal to a structural part can be calculated by eq.4.5.

$$F_W = CqSsina \quad (4.5)$$

C is a shape coefficient given in NS-EN-1991-1-4, q is the basic wind pressure given by eq.4.6, S is the projected area of the part normal to the direction of the load and α is the angle between the axis of the part and the wind direction. Lift forces due to wind loads may also be important for design.[DNV-GL, 2010b]

$$q = \frac{1}{2} \rho_a U_{T,z}^2 \quad (4.6)$$

ρ_a is the mass density of air and $U_{T,z}$ is the mean wind velocity averaged over a time T at height z (m) above msl or the ground. $U_{T,z}$ can be estimated based on spectral analysis of long time-series of wind measurements. Thus, site-specific measured wind data should be carried out. It is preferred that the data base covers continuous data for a 10-year period or more.[DNV-GL, 2010b] The DNV-RP-C205 includes various formulations of the wind velocity profile. A common reference used is a height of 10m above ground and a time-averaging interval of 10 minutes.[DNV-GL, 2010b]

Wind loads are not considered relevant for the free-spanning SFT for the Digernesund.[Engseth et al., 2016]

4.2.5 Wave-induced loads

According to chapter 5.4.4 in N400 [Vegdirektoratet, 2015], wave loads should be calculated in either time domain based on linear wave theory or in frequency domain using stochastic methods. For wind-generated waves, the JONSWAP wave spectrum can be used. Wave loads can also be calculated using empirical formulas given in DNV-RP-C205 (2010) or by CFD-analysis. For offshore structures, it is normal to use the wave heights with a return period of 100 years for both wind generated sea and swell sea, to ensure conservatism.[NORSOK, 2007]

First order wave forces are assumed to be important in the spectral peak interval 3 – 24s for marine structures. However, second order wave forces may be important as well. These are mean forces and forces oscillating with difference frequency or sum frequency. With difference or sum frequency it is meant that either the sum or difference of two frequencies is used when describing the wave spectrum. Difference frequency loads are also called slowly-varying loads.[Faltinsen, 1990]

Morison equation

For small scale structures, meaning structures considered much smaller than the wavelength, the Morison's equation can be used to calculate the wave loads acting on the structure.[Vegdirektoratet, 2015] If $\lambda > 5D$, where D is the equivalent diameter of the structure and λ is the wavelength of the incident wave, the structure can be characterized as a small scale structure. The wavelength can for deep water waves be calculated according to eq. 4.7-4.8.[Faltinsen, 1990]

Dispersion relation for deep water (eq.4.7), wave frequency (eq.4.8) and wavelength (eq.4.9) of incoming waves with wave period T :

$$\omega^2 = gk \quad (4.7)$$

$$\omega = \frac{2\pi}{T} \quad (4.8)$$

$$\lambda = \frac{2\pi}{k} \quad (4.9)$$

The wave conditions for the Digernesund were given in sec. 3.5.2. In the following, $T_p = 4.7s$ is used for wind induced waves and $T_p = 14s$ for swell waves. The swell

sea condition corresponds to a wave length roughly 18 times the largest equivalent diameter of the SFT. Thus, the condition for being a small structure is satisfied for swell sea. Therefore, it is assumed that the Morison's equation can be applied for the swell sea condition. Investigating the exponential decay of wave action, fig. 4.2, it is seen that the swell induced waves are also the dominating wave type at the depth of the SFT.

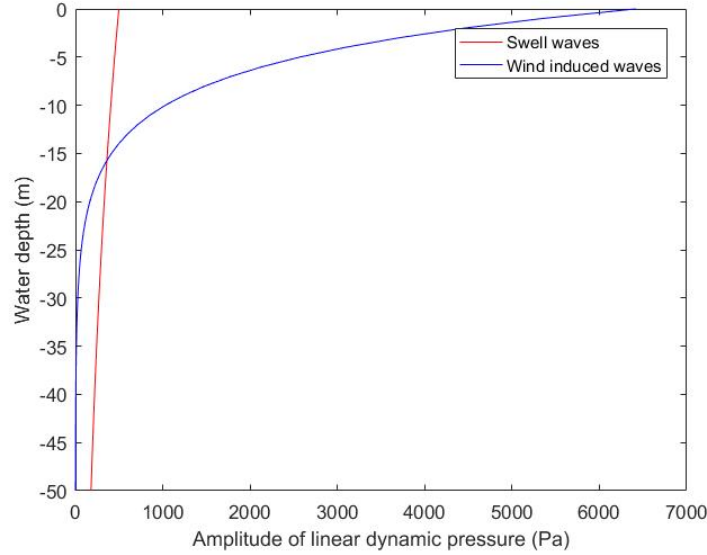


Figure 4.2: Graph showing the decay of wave action for swell and wind induced waves in the Digernessund.

In Faltinsen (1990), two different forms of Morison's equation for a strip of a circular cylinder with length dz are given (eq.4.10-4.11). Both forms includes a mass term proportional to the incident fluid acceleration u , and a drag term. The difference is that the latter form includes a nonlinear drag term, and therefore, the velocity is here the relative velocity between the incident fluid velocity u and the structure velocity $\dot{\eta}$. The latter form has also an additional inertia term proportional to the structure acceleration $\ddot{\eta}$. This expansion of the equation is due to the fact that the latter form applies to a moving structure, while the first form assumes a fixed and rigid one.

$$dF = \rho_w Az C_M a + \frac{\rho_w}{2} C_D D dz |u| u \quad (4.10)$$

$$dF = \frac{1}{2} \rho_w C_D D dz (u - \dot{\eta}) |u - \dot{\eta}| + \rho_w C_M A dz a - \rho_w (C_M - 1) A dz \ddot{\eta} \quad (4.11)$$

where ρ is the water density, D is the diameter of the strip, A is the cross-section area of the strip, C_M is the added mass coefficient and C_D is the drag coefficient. The two coefficients, C_M and C_D have to be empirically determined and are dependent on Reynolds number, Keulegan-Carpenter number, surface roughness ratio, a relative current number, form of the structure, free-surface effects, sea-floor effects. $C_D = 0.7$ is a typical value for smooth surfaces. By inserting the expression for the fluid particle acceleration and velocity in the Morison equation, it can be shown that the mass-force term decays

with the depth with a factor of $e^{\frac{2\pi z}{\lambda}}$, and the drag force term decays with a factor of $e^{\frac{4\pi z}{\lambda}}$. [Faltinsen, 1990]

Wave loads on Large-volume structures

For large scale structures, meaning structures with cross-section dimensions larger than the wavelength, the diffraction effects become important. [Vegdirektoratet, 2015] The procedure for this is given in chapter 7 in DNV-RP-C205.

Similar to wind, waves are time-varying and random, or irregular, by nature. Assuming that linear theory is valid, wave induced loads in irregular sea can be found by linear superposition of loads from regular wave components. Transient effects are neglected by assuming steady state, which also implies that the dynamic response oscillates harmonically with the same frequency as the waves exciting the structure. The response from regular waves is found by looking at two sub-problems: radiation and diffraction. [Faltinsen, 1990]

The radiation problem is associated with no incoming waves and forces and moments on the structure when it is forced to oscillate in a rigid body motion with the wave frequency. This produces the hydrodynamic forces and moments corresponding to added mass and damping loads. The latter is due to the generation of waves because of the forced motion. The forced motion also results in oscillating water pressure acting on the body surface. Thus, integrating the pressure over the body surface give resulting forces and moments. For the harmonic motion η_j the hydrodynamic added mass, damping and restoring loads can be written as eq. 4.12. [Faltinsen, 1990]

$$F_k = -A_{kj} \frac{d^2 \eta_j}{dt^2} - B_{kj} \frac{d\eta_j}{dt} - C_{kj} \eta_j \quad (4.12)$$

A_{kj} is an added mass coefficient, B_{kj} is a damping coefficient and C_{kj} is a restoring coefficient with $k, j = 1, 2, \dots, 6$, meaning for the six degrees of rigid body modes. The added mass and damping coefficients are functions of the structure form and frequency of oscillation.

For the diffraction problem, there are incoming waves exposing the structure to wave excitation loads. The structure is assumed fixed, or restrained from oscillating. This results in two effects, the unsteady pressure induced by the undisturbed waves (Froude-Kriloff) and an additional force due to the structure presence changes the pressure field. The latter produce diffraction forces and moments. [Faltinsen, 1990]

4.3 Deformation loads for concrete structures

4.3.1 Post-tension

According to N400, both the direct and indirect reactions due to tensioning of post-tension cables should be included.

4.3.2 Creep

Creep is an additional deformation of concrete subjected to compression for a long time. The concrete continues to compress beyond the instantaneous deformation of the applied loads. Shrinkage (svinn) is caused by dehydration of the concrete.[Sørensen, 2013] Creep and shrinkage is dependent the humidity of the environments, the cross-section dimensions and the composition of the concrete. Creep is also dependent on the maturity of the concrete when the load is applied, the load level and load duration.[NS-EN1992, 2004] The procedure for calculating creep strain is given in 3.1.4 in [NS-EN1992, 2004].

Shrinkage is composed of two contributions, dehydration shrinkage and autogenous shrinkage. The latter develops together with the concrete strength development, while the dehydration shrinkage is a slow process forced by moisture transfer through the cured concrete. For a given age, the development of shrinkage is given by mathematical formulas in 3.1.4(6) and appendix B in [NS-EN1992, 2004].[Sørensen, 2013]

Creep and shrinkage are not accounted for the SFT in this thesis.

4.3.3 Temperature

Thermal reactions can cause deformations of the structure. Relevant reactions due to temperature differences are calculated according to NS-EN 1991-1-5. According to [Engseth et al., 2016], the temperature variations are $\pm 5^{\circ}\text{C}$ and can thus be neglected for the SFT for the Digernessund.

4.4 Accidental loads

Accidental loads relevant for marine bridges are listed below. The load combinations for accidental limit state can be found in NS-EN1990:2002.[Vegdirektoratet, 2015]

- Accidents with anchors and trawlers
- Fire
- Explosions
- Landslide
- Ship collisions
- Sinking ship and dropping objects
- Flooding
- Abnormal waves
- Earthquake

Part II

Structural analysis of a SFT

Chapter 5

FE-model of the SFT

5.1 Modeling software

In this thesis, two types of softwares are used. The software package Sesam, provided by the DNV-GL, is the main software used. In addition, the results from eigenvalue analysis are compared with results from Abaqus. The latter program is capable of non-linear static analysis, which is not the case for Sesam. The Sesam software package consists of several programs, as shown in the figure 5.1 below. The ones used in this thesis are marked with red circles.

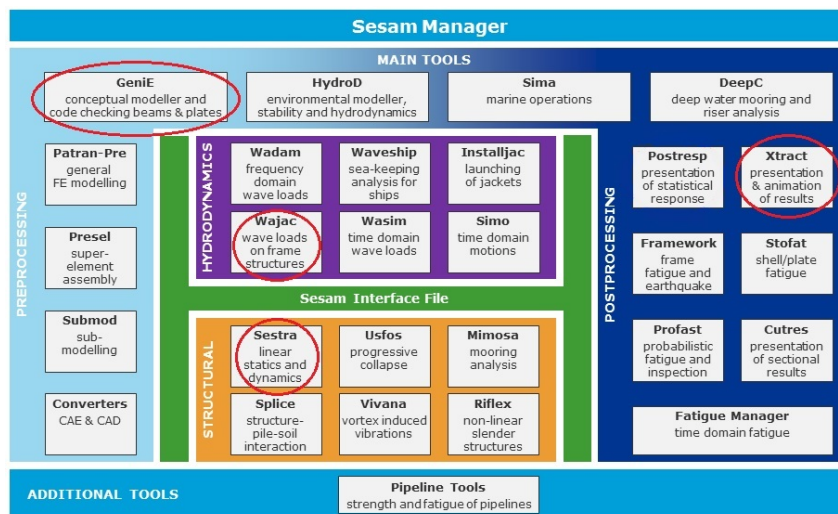


Figure 5.1: Overview of the software package SESAM. Red circles show the programs used in this thesis. Illustration:[DNV-GL software, 2017]

The Sesam Manager is a control program used to set up runs of the different programs in Sesam. GeniE is the modelling software used to establish a finite element model of the bridge. Static loads like traffic load are also be defined here. Sestra is the program for linear static and dynamic analysis, and can be executed from the Sesam Manager. Wajac is the program for calculating wave loads for fixed structures.[DNV-GL software, 2017] Xtract is a program for postprocessing the results from Sestra.

5.2 Global model

Elements

The bridge is modeled by 2-node straight beam elements, which have degrees of freedom per node, 3 translational and 3 rotational, ie. a total of 12 degrees of freedom per element. It is assumed that the cross-section is constant within the element, and the material is assumed isotropic. Axial strain, bending strain and shear strain about the two principal directions of the cross-section are accounted for, and St. Venant torsion is also accounted for in the element formulation.[DNV-GL software, 2014]

Configurations of the bridge

In this thesis, four different configurations of the bridge are investigated for both static and eigenvalue analysis. The first and simplest one is a straight configuration. Three horizontally curved models are also investigated. The first curved model (fig. 5.2), which is the base case in this thesis, has a curve height $C_1 = 24.25m$ and radius $R = 1850m$, which corresponds to the curved model in [Engseth et al., 2016]. The second curved model has a curve height of $C_2 = 53m$ and corresponding radius $R = 867.53m$. The third curved model has a curve height $C_3 = 60m$ and corresponding radius $R = 772.92m$. See app. C for how the curved models are established.



Figure 5.2: Illustration of global model for base case.

5.3 Material

To satisfy the SLS conditions, the concept proposed in [Engseth et al., 2016] is heavily post-tensioned. Thus, minimum reinforcement is sufficient to satisfy ULS and ALS. [Engseth et al., 2016] Because the technical report provides insufficient details regarding the reinforcements, a rough estimate of the minimum reinforcements is provided in this thesis. A resulting sketch of the minimum reinforcements and PT-cables in the longitudinal direction is given in app. E.2. The material density of reinforced concrete is assumed $25kN/m^3$ in agreement with [Engseth et al., 2016].

5.3.1 Reinforcement steel

Instructions for design of reinforcements in concrete bridges are given in N400, page 89 to 91. The instructions will be briefly summarized here. The smallest allowable diameter for reinforcements is 12 mm, according to N400. All cross-sections should have double reinforcement in both directions. For the walls, the vertical and horizontal reinforcement should have centre distance smaller or equal to 200 mm. Longitudinal reinforcements should have diameter higher or equal to 16 mm. For horizontal decks, the centre distance should also be smaller or equal to 200 mm, and the longitudinal reinforcements should have a diameter higher or equal to 16 mm.[Vegdirektoratet, 2015]

Minimum reinforcement requirements are given in [NS-EN1992, 2004]. For the outer and inner walls, point 9.6.2 and 9.6.3, page 161, and NA.9.6.2 and NA.9.6.3, page 16, are used. Point 9.2.1.1 is used for reinforcement in the horizontal bearing. The resulting minimum reinforcements are given in tab.5.1 and total reinforcement areas are given in section. E.1.

Table 5.1: Summary of calculated minimum reinforcement

Section	Type	Diameter	Centre distance
Outer walls	Horizontal, longitudinal	$\phi 25$	c200
Outer walls	Vertical	$\phi 25$	c200
Inner walls	Horizontal, longitudinal	$\phi 16$	c190
Top/bottom slabs	Horizontal, longitudinal	$\phi 16$	c200
Inner slabs	Horizontal, longitudinal	$\phi 16$	c200

Note that this is only an estimate of the minimum longitudinal reinforcements. The objective for estimating these reinforcements is to include the contributions from the reinforcements in the bending stiffness of the structure. In detailed design, a full assessment of the necessary reinforcements should be carried out. A special care has to be taken with respect to the hydrostatic pressure, which is calculated 0.497 MPa at a water depth of 50m.

5.3.2 Post-tension cables

Stressed concrete is defined as concrete subjected to compression to counter-act the external loads to some extent. The compression is induced on the concrete by prestressing steel given an initial strain and tension force. Meaning, the tension in the prestressing steel is transferred to concrete as compression at end anchorage of the prestressing steel or by adhesion between the two materials. The main advantages of using prestressing steel is that cracking reduces, and that displacements reduces because of opposite displacements induced by the prestressing steel and higher bending stiffness.[Sørensen, 2013]

There exists two methods of stressed concrete, pre-tension, using wires, and post-tension, using cables. The latter will in the following be referred to as PT-cables. The

main difference is whether the steel is subjected to a tension force before or after the concrete is cast and cured. When pre-tension wires are used, the steel is given a tension force before casting the concrete. When the concrete reach adequate strength or compactness, the pre-tension wires are cut at the die or at end-anchorage. The PT-cables are carried through ducts in the cast structure and anchored at one of the ends at anchor plates. After giving them a tension force, by a jack for instance, the ducts are injected with injection mortar to ensure adhesion between the concrete and PT-cables. The cables can be given a desired curved path adjusting the post-tension to the moments from the external loads to fit. PT-cables are used for e.g. large bridges, containers, concrete platforms and frame structures cast in situ.[Sørensen, 2013]

PT-cables for the base case

In the technical report [Engseth et al., 2016], it is suggested to use post-tension cables, 6-31 stand Y1860 for the longitudinal cables, as stated in 3.4. The technical report suggests further a centre distance of 700 mm, and a total area of 4650 mm^2 per post-tension cable, for both walls and top and bottom slabs.[Engseth et al., 2016]

However, in order to include the effects of the post-tension cables, the amount of cables is needed. As suggested by Arianna Minoretti, representing the NPRA, the amount of necessary PT-cables for the smallest cross-section is used for all cross-sections in the parts with varying heights as a simplification. In reality, the amount of PT cables may vary across the length of the bridge. Using a centre distance of 700 mm, the amount of PT-cables are approximately 18 in bottom/top slab and 21 in the walls. That is, 78 cables in total. In this thesis, it is assumed that the cables are symmetric and have a centric location in each part of the cross-section.

5.4 Cross-sectional properties

The original model proposed by dr. techn. Olav Olsen in [Engseth et al., 2016] has varying cross-section, as shown in fig. 3.2. Two cross-sections cases are investigated in this thesis. The base case is a simplification of the original model proposed by dr. techn. Olav Olsen in [Engseth et al., 2016]. That is, a simplification of the tapered part using a linear approximation. The next model is a constant average cross-section throughout the structure length.

As earlier stated in section 5.2, the 2-node beam elements in GeniE assume constant cross-sections. To account for the two parts with linearly varying cross-section an approximation has to be made. The part with linearly varying cross-section is divided into 4 parts with different cross-sections. Within each part, the cross-section is constant. The method for finding the cross-sections heights is given in AB.3. Dimensions for the cross-sections in fig. 3.2, together with concrete area and second moment of inertia about z-axis, are given in the feasibility study [Engseth et al., 2016]. These values are the basis for calculating the resulting dimensions. An illustration of the resulting front elevation is given in figure 5.3.

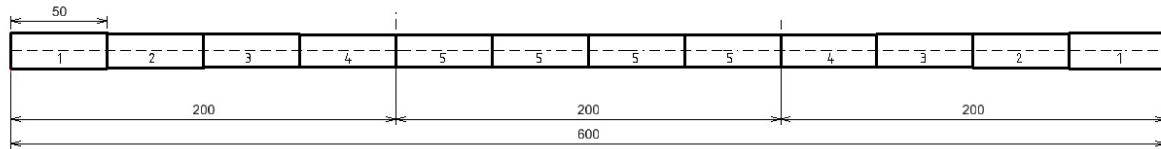


Figure 5.3: Illustration of the model with varying cross-section

For simplicity, the cross-sections are modeled in GeniE as general cross-sections. When creating a general section, the software demands even more cross-section properties which have to be calculated in advance. These are calculated based on the cross-sectional dimension given in fig.3.2. The calculated cross-sectional properties and formulas can be found in appendix B. It is important to note that the cross-section in 3.2 is assumed doubly symmetric. In z -direction, it is assumed that the ballast chambers COG, coincides with the outer structure COG. Also note that when calculating the moments of inertia about y -direction I_y , the brackets are included by adding 2%. This percentage corresponds to the deviation in I_z when calculating I_z without brackets, based on the dimensions given in fig 3.2, compared to the values given in the technical report. For the remaining properties, the brackets are simply not accounted for.

The cross-sectional properties for the case of a constant cross-section are found by taking the average of the given heights, areas and moments of inertia for cross-section 3.2 a and b. Additional properties are calculated from these average values. A complete summary of cross-sectional properties used in the analysis is given in app. B.

5.4.1 Transformed cross-section

When calculating the stresses in concrete in SLS, it is assumed that there is full adhesion between the concrete and the reinforcements, meaning that the materials have the same strain, and that the materials are linearly elastic. The latter refers to Hook's law. The stresses will be affected by the different modulus of elasticity for the different materials. First, we look at the effects of ordinary reinforcements only. By equilibrium considerations, a mutual strain can be expressed as given in eq. 5.1. The derivation of eq. 5.1 can be found in [Sørensen, 2013].

$$\epsilon = \frac{P}{E_c \left[A_c + \left(\frac{E_s}{E_{cm}} \right) A_s \right]} \quad (5.1)$$

Where P is an axial compression force, E_{cm} and E_s are the modulus of elasticity of concrete and reinforcements respectively and A_c and A_s are the cross-section areas of concrete and reinforcements, respectively. The denominator in eq. 5.1 represents the equivalent stiffness of the cross-section. The modulus of elasticity of concrete E_c is multiplied with an equivalent or transformed concrete cross-section, including the effects of the reinforcements.[Sørensen, 2013]

In [Bernhardt, 1975], the effects of PT-cables are included when calculating the transformed concrete area as shown in eq.5.2.

$$A_T = A_c + \eta(A_s + A'_s) + \eta_p A_{sp} \quad (5.2)$$

where A_T represents the transformed concrete area, A_c is the total concrete area, A_s and A'_s are the total ordinary reinforcement areas and A_{sp} represents the total PT-cable area. Here, $\eta = \frac{E_s}{E_c}$ and $\eta_p = \frac{E_p}{E_c}$. In the latter, E_p is the modulus of elasticity for PT-cables.

If the PT-cables have an eccentricity in relation to the COG, the new location of the COG has to be determined.[Bernhardt, 1975]

Transformed area and moment of inertia for the base case

In the following, only the longitudinal reinforcements and post-tension cables are accounted for. Contributions from vertical reinforcements and post-tension cables should also be investigated. In addition, brackets are not included here.

Due to the assumption of symmetric ordinary reinforcements and symmetric amount of PT-cables in both directions, the COG including the reinforcements and PT-cables will coincide with the COG of concrete. However, if there was unsymmetrical number of PT-cables, the COG would have shifted in z-direction. The procedure for calculating the new position of the COG is based on moment equilibrium about the original COG and given in [Sørensen, 2013].

For a rectangular section with post-tension cables in the lower edge, [Sørensen, 2013] defines the transformed moment of inertia as eq. 5.3.[Sørensen, 2013]

$$I_t = \frac{bh^3}{12} + bhy_t^2 + (\eta_p - 1)A_p(e - y_t)^2 \quad (5.3)$$

However, in this particular case we have a box section. To simplify the calculations of the transformed moment of inertia, the contributions from concrete, ordinary reinforcements and PT cables are kept separate. That is:

$$I_t = I_{t,c} + I_{t,s} + I_{t,p} \quad (5.4)$$

where $I_{t,c}$ is the contributions in moment of inertia from concrete area, $I_{t,s}$ is the contributions in moment of inertia from ordinary reinforcements and $I_{t,p}$ is the contributions from post-tension cables. All contributions includes the effects of parallel axis theorem. See appendix.F.2.

5.5 Boundary conditions

By reference to the technical report [Engseth et al., 2016] the bridge is assumed clamped at both ends. That is, that all translations and rotations are fixed at the two ends of the structure. This simulates the connections to the rock tunnels at the two ends of the crossing.

5.6 Ballast

According to the technical report, the bridge should contain permanent ballast consisting of both solid ballast and water ballast. The solid ballast has specific weight $19kN/m^3$. [Engseth et al., 2016]. The ballast chambers has varying height, as seen from fig. 3.2. The total area of the three chambers for the smallest cross-section is $28.3m^2$, while the total area of the three chambers for the largest cross-section is $53.8m^2$. In this thesis, it is assumed that the total ballast chamber area vary linearly between these two areas for the part of the bridge with varying cross-section. The same method for finding the height of the approximated cross-sections, app. B.3, is applied to find the chamber areas for each element in fig. 5.3. In the technical report, the ballast chamber fill is given in percentage for the two cross-section. It is given that the smallest cross-section has ballast fill of 60.4%, while the largest cross-section has ballast fill of 79%. [Engseth et al., 2016] For the part of the bridge with varying cross-section, the same approach of linear approximation is applied. The amount of water and solid ballast is assumed 34% and 66% respectively, of the ballast fill.

In this thesis, the permanent ballast is accounted for by increasing the total material density ρ_0 . This can easily be done by rearranging the equation for mass, eq. 5.5, which corresponds to the mass of concrete plus mass of ballast fill.

$$A_c L \rho_0 = A_{WB} L \rho_{WB} + A_{SB} L \rho_{SB} + A_c L \rho_{RC} \quad (5.5)$$

where RC stands for reinforced concrete, WB stands for water ballast and SB stands for solid ballast. A_{WB} is assumed 34% of the total ballast fill area, while A_{SB} is assumed 66% of the total ballast fill area. Each element in fig 5.3 has individual values for the ballast fill area. Thus, there will be five material densities in total for the case with tapered parts, and one additional density for the case with constant average cross-section. The ballast fill percentages and resulting ballast fill areas for the base case are given in tab.5.2.

Table 5.2: Linearly varying ballast fill, section 1 to 5.

Section	Ballast percent fill	Resulting ballast fill area
1	79%	$42.50 m^2$
2	74.4%	$35.35 m^2$
3	69.7%	$28.79 m^2$
4	65.1%	$22.80 m^2$
5	60.4%	$17.39 m^2$

In both static analysis and eigenvalue analysis, a simplified ballast case is used in addition to the base case. This simplification is made to compare results from the software with simple hand-calculations. The simplified case is a constant average cross-section throughout the structure length, where an average is taken between the two given ballast fills (average between the ballast fill corresponding to the largest and smallest cross-section given in the technical report). The average ballast fill is given in table 5.3.

Table 5.3: Constant average ballast fill, for average cross-section.

Section	Ballast percent fill	Resulting ballast fill area
Average	69.7%	28.79 m ²

5.7 Hydrodynamic coefficients

Added mass and damping coefficients from [Xiang et al., 2017] are based on Frank Close Fit Method. The damping coefficients are close to zero, reflecting that the ability of the structure to generate waves is very small. The added mass coefficients are assumed constant without potential damping.[Xiang et al., 2017] Added mass and damping coefficients are assumed independent of frequency. In Sesam, added mass loads are calculating by executing Wajac. The default is to not calculate added mass and damping, so this has to be checked. The value $C_m = 2.0$, corresponding to added mass coefficient with value 1.0, is used for all elements. The coefficient is specified for force components normal to the members. At each load calculation point, added mass components per unit length are calculated [DNV-GL software, 2017]:

$$m_a = \left[\rho \frac{\pi^2}{4} (C_m - 1) \right] \quad (5.6)$$

Chapter 6

Static response analysis

This chapter concerns a study of the static response of the SFT proposed for the Digernessund. First, the theory for static analysis is given together with finite element formulations for straight and curved beams. The load cases and load combinations used in static analysis are also given. The structural behaviour is investigated in both ultimate limit state and serviceability limit state. The response of static analysis is meant as the resulting bending moments, torsion moments, reaction forces and the displacements of the structure.

The results from static analysis are given in section 6.5. The base case is a curved bridge with a horizontal curve height $C = 24.25m$, in correspondence with the proposed concept in [Engseth et al., 2016]. The model has varying cross-section as described earlier. The result-section also includes a parameter study of the curve height. The results from static analysis with straight configuration ($C = 0$), curved configuration with curve height $C = 53$ and $C = 60$ are compared to the results for the base case.

The effects of the PT-cables and reinforcements on the bending moments were calculated by hand, and are also included in the result section.

6.1 Theory of static analysis

6.1.1 Static analysis

The theory for static response analysis given in this section is gathered from [Moan, 2003a].

Structural analysis using finite element method is based on three fundamental laws. These are equilibrium in all parts of the structure, compatibility in the material and Hook's law for linearly elastic material. Compatibility in the material means that the material is continuous as it deforms, and that all adjacent sections share deformations. In addition, in linear analysis it is assumed that the displacements are small, meaning that the equilibrium equations are established based on the initial configuration. [Moan, 2003a]

For each element, the displacement within the element can be expressed by assumed shape functions. These shape functions are scaled by the node displacements. The relationship between the displacements and forces at the node points are given in eq.6.1.

$$\mathbf{S} = \mathbf{k}\mathbf{v} + \mathbf{S}^o \quad (6.1)$$

where \mathbf{S} is the generalized nodal point forces, \mathbf{k} is the element stiffness matrix, \mathbf{v} is the nodal displacements and \mathbf{S}^o is the external nodal point forces. The element stiffness matrix can be found by energy or work considerations.

Demanding equilibrium for all nodal points, the stiffness relation for the total system is given by eq. 6.2.

$$\mathbf{R} = \mathbf{K}\mathbf{r} + \mathbf{R}^o \quad (6.2)$$

where \mathbf{R} is the nodal load vector, \mathbf{K} is the global stiffness matrix, \mathbf{r} is the unknown nodal displacements and \mathbf{R}^o is the external nodal point forces.

The global stiffness matrix \mathbf{K} can be found by assembling and adding the element stiffness matrices. The nodal load vectors \mathbf{R} and \mathbf{R}^o can also be obtained from the element nodal forces. Applying the boundary conditions, meaning setting nodal displacement equal to known values, the global displacements can be found by rearranging eq. 6.2 and solving eq. 6.3:

$$\mathbf{r} = \mathbf{K}^{-1}(\mathbf{R} - \mathbf{R}^o) \quad (6.3)$$

Knowing the displacements, stresses can be found by Hook's law on matrix form.

Static analysis in Sestra

The method in Sestra is based on a displacement based finite element method which results in a linear system of equilibrium equations (eq. 6.4).

$$\mathbf{K}\mathbf{r} = \mathbf{R} \quad (6.4)$$

where \mathbf{R} represents the nodal load matrix. Application of boundary conditions reduce the system to 6.5:

$$\mathbf{K}_{ii}\mathbf{r}_i = \mathbf{R}_i \quad (6.5)$$

where i represents the dof of the structure.

In Sestra, the solution method for the system equilibrium equation is based on Cholesky factorization. Please note that Sestra is limited to linear theory assuming small displacements.

Nonlinear analysis

The theory in this section is gathered from [Moan, 2003b]. A linear structural analysis gives information about nonlinearities that can be important for the particular problem of interest. Such information can be if and where the stresses exceeds allowable limits, which may imply that elasto-plastic behaviour should be considered. If the structure is loaded with compressive loads, buckling may be an important problem. Code formulations about the ultimate strength can together with the elastic buckling load give information about the ultimate capacity to be expected.[Moan, 2003b]

For ultimate and accidental limit states it can be necessary to include nonlinear structural behaviour for design. Nonlinear structural behaviour can be divided into three different types, geometrical nonlinearity, material nonlinearity and nonlinearity associated with boundary conditions. Geometrical nonlinearity will be the focus in the following, and is the structural behaviour when the deformations cannot be assumed small and the change of geometry is accounted for when calculating strains, stresses and establishing equilibrium equations.

Geometrical nonlinear problems can be classified into small strain GNL problems and large strain GNL problems. The first is associated with small or large rotations. Relevant problems with small rotations can for instance be arches deflected by transverse load. Relevant problems with large rotations can for instance be for deep arches. Large strain GNL problems are complex and associated with manufacturing processes.

Two different formulations for geometrical non-linear problems are the total Lagrange formulation and the updated Lagrange formulation. In the latter formulation, a local system is used to determine the element stiffness relationships, which then is transformed into a fixed, global coordinate system before assembling the global stiffness relation. When the deformations cause the geometry to change the local coordinate systems need to be updated. Thus, the non-linear effects are included by continuously changing the transformation matrices. Here each element is assumed to behave linearly when referred to co-rotational coordinates, and thus small deformations on local level are assumed. The total Lagrange formulation is on the other hand based on a fixed coordinate system. The strain formulation utilized here is the Green's strain. For a plane beam with axial displacements of the neutral axis, the vertical displacement w_x causes additional axial membrane strain, which is recognized as the last term in eq.6.6. If the axial strains are not small, the horizontal displacement u_x cause another additional term, which is recognized as the third term in the same equation. These two additional terms are ignored in linear theory. Thus, as opposite to linear analysis, the axial and lateral behaviour is coupled in non-linear geometrical problems.

$$E_{xx} = u_{,x} - zw_{,xx}(x) + \frac{1}{2}u_{,x}^2 + \frac{1}{2}w_{,x}^2 \quad (6.6)$$

An initial lateral deflection, which is the same as the beam being a shallow arch, will also affect the formulations. When an additional lateral displacement w_x occurs, the resulting arch length is given by eq.6.7 and the resulting Green strain is given by eq.6.8.

$$ds^* = [1 + (\bar{w}_{,x} + w_{,x})^2]^{\frac{1}{2}} dx \approx [1 + \frac{1}{2}(\bar{w}_{,x} + w_{,x})^2] dx \quad (6.7)$$

$$E_{xx} = u_{,x} - zw_{,xx} + \bar{w}_{,x}w_{,x} + \frac{1}{2}w_{,x}^2 \quad (6.8)$$

The equations to be solved in nonlinear structural analysis is given by eq.6.9 and eq.6.10. The displacement vector \mathbf{r} is sought for a given external load \mathbf{R} , and the stiffness matrix is dependent on the displacements and thus given on incremental form (eq.6.11). The equations can be solved by different techniques, such as incremental procedures, iterative procedures or combined methods. See [Moan, 2003b] for more information about the solution methods.

$$\sum_i (\mathbf{a}^i)^T \mathbf{S}^i = \mathbf{R} \quad (6.9)$$

$$\mathbf{K}_I(\mathbf{r})d\mathbf{r} = d\mathbf{R} \quad (6.10)$$

$$\mathbf{K}_I = \mathbf{K}_0 + \mathbf{K}_G + \mathbf{K}_\sigma \quad (6.11)$$

The first term is the contribution from small displacement structural analysis. The second term represents the effect of changing geometry on the stiffness, and the latter term represents the effect of initial member forces.

Initial imperfections and amplification factor

The theory in this section is gathered from [Amdahl, 2013]. For real structures, geometric imperfections exist. Assume that initial imperfections can be described by a sinusoidal (fig. 6.1):

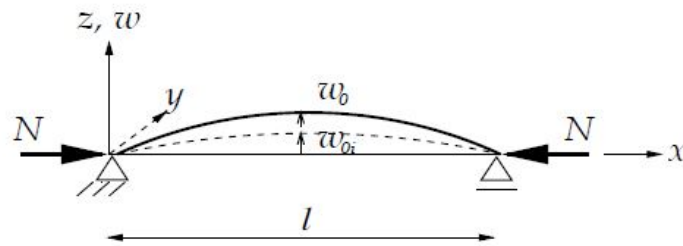


Figure 6.1: Pin-end column under axial compression. Illustration: [Amdahl, 2013]

The total deformation is given by:

$$w = w_0 \sin\left(\frac{\pi x}{l}\right) \quad (6.12)$$

By means of energy methods and the principle of minimum potential energy, an expression for w_0 can be obtained according to [Amdahl, 2013], eq.6.13-6.14:

$$w_o = w_{oi} \frac{1}{1 - \frac{N}{N_E}} \quad (6.13)$$

$$M = M_0 \frac{1}{1 - \frac{N}{N_E}} \quad (6.14)$$

where the latter term represents an amplification factor. Generally, the amplification factor multiplied by the deflection gives a good estimate for the maximal deflection, but is poorer for maximum bending moment. For large axial forces, the discrepancy can be significant. Still, the total stress is dominated by the mean compressive stress and the discrepancy in the total stress will be smaller.[Amdahl, 2013]

The capacity is smaller than the Euler buckling load, N_E , which is approached asymptotically. Increasing initial imperfections results in non-linear response (fig. 6.2).

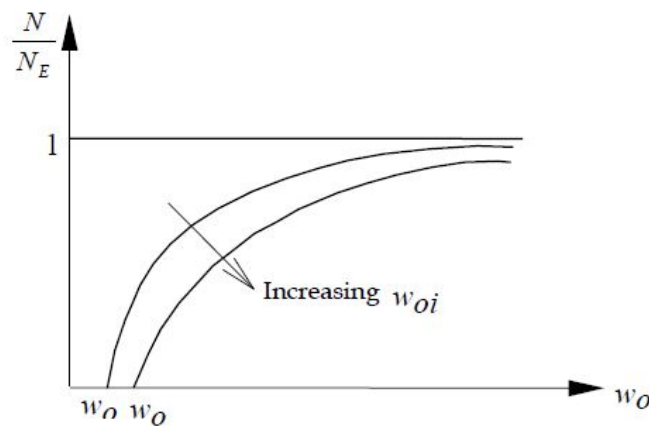


Figure 6.2: Pin-end column under axial compression. Illustration: [Amdahl, 2013]

The Euler buckling load for a straight beam is given by eq.6.15.[Larsen et al., 2009]

$$N_E = \frac{\pi^2 EI}{l_k^2} \quad (6.15)$$

l_k is defined as the buckling length and is dependent on the supports. For a straight beam with both ends fixed, l_k can be approximated as $l_k = 0.5l$, where l is the total length of the beam.[Larsen et al., 2009]

True amplification factor for beam with fixed ends, subjected to axial compression and lateral uniform load (fig. 6.3) are given in eq. 6.16-6.17 [Amdahl, 2013].

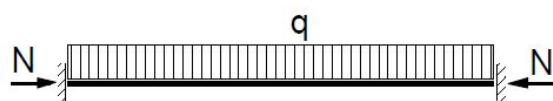


Figure 6.3: Pin-end column under axial compression.[Amdahl, 2013]

$$a = \frac{kl}{2} = \frac{\pi}{2} \sqrt{\frac{N}{\pi^2 EI/l^2}} \quad (6.16)$$

$$f_m = \frac{2}{a^2} \left(\frac{1}{\cos(a)} - 1 \right) \quad (6.17)$$

6.1.2 Finite element formulations

Finite element formulation for a beam element

For a beam element, compatibility is ensured by proper boundary conditions, and describing the displacements by continuous lateral displacement w . Navier's hypothesis is assumed, meaning that it is assumed that the cross-sections remain plane and perpendicular to the beam axis at all times. [Moan, 2003a]

The displacements are assumed expressed by displacement patterns w within the element. The displacement pattern is defined by eq. 6.18:

$$w = \mathbf{N}_q \mathbf{q} \quad (6.18)$$

where \mathbf{q} is defined as a set of generalized displacements, and \mathbf{N}_q is the generalized shape functions.

The nodal displacements \mathbf{v} is related to the generalized displacements \mathbf{q} in eq.6.19.

$$\mathbf{v} = \mathbf{A} \mathbf{q} \quad (6.19)$$

Inserting eq.6.19 into eq. 6.18 we obtain the following:

$$w = \mathbf{N}_q \mathbf{q} = \mathbf{N}_q \mathbf{A}^{-1} \mathbf{v} = \mathbf{N} \mathbf{v} \quad (6.20)$$

The approximated curvature can be calculated by eq.6.21:

$$\kappa = \frac{d^2 w}{dx^2} = \frac{d^2}{dx^2} [\mathbf{N}_q \mathbf{q}] = [\mathbf{B}_q \mathbf{q}] \quad (6.21)$$

Applying the principle of virtual displacement results in eq.6.22:

$$\int_0^L \tilde{\mathbf{v}}^T \mathbf{A}^{-T} \mathbf{B}_q^T (EI) \mathbf{B}_q (\mathbf{A}^{-1}) \tilde{\mathbf{v}} dx = (\tilde{\mathbf{v}})^T \mathbf{S} + \int_0^L (\tilde{\mathbf{v}})^T (\mathbf{N})^T q dx \quad (6.22)$$

For all possible $\tilde{\mathbf{v}}$:

$$\int_0^L [(\mathbf{A})^{-T} \mathbf{B}_q^T (EI) \mathbf{B}_q (\mathbf{A}^{-1}) dx] \mathbf{v} = \mathbf{S} + \int_0^L (\mathbf{N})^T q dx \quad (6.23)$$

resulting in eq. 6.24:

$$\mathbf{S} = \mathbf{k}\mathbf{v} + \mathbf{S}^o \quad (6.24)$$

where $\mathbf{k} = \int_0^L (\mathbf{A})^{-T} \mathbf{B}_q^T (EI) \mathbf{B}_q (\mathbf{A})^{-1} dx = (\mathbf{A})^{-T} \mathbf{k}_q (\mathbf{A})^{-1}$. Here, \mathbf{k}_q is the generalized stiffness matrix.

When the system relation eq. 6.24 is solved, the bending moment in an arbitrary point in the beam can be found by 6.25:

$$M_x = -EIw_{,xx} = -EI \frac{\partial^2}{\partial x^2} (\mathbf{N})\mathbf{v} \quad (6.25)$$

Finite element formulation for curved one-dimensional structures

The theory in this section is gathered from chapter 8 in [Moan, 2003a]. Curved structures carry loads by a combination of bending moments and in-plane forces. The interaction between the bending and membrane behaviour is due to the curved configuration. Fig.6.4 show the definitions of the axial force N , shear force Q and bending moment M for an arc. Considering a infinitesimal element of length ds , 6.4 a, equilibrium equations can be established.

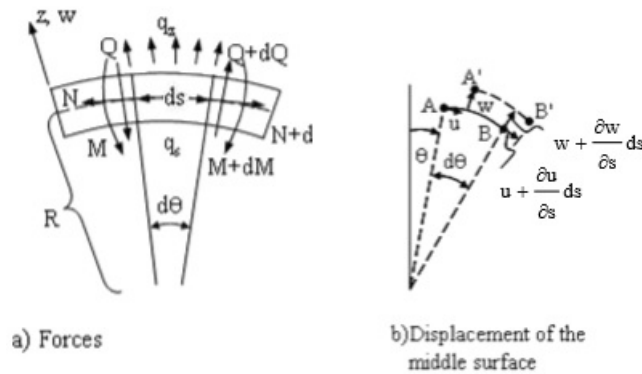


Figure 6.4: Displacements and forces for an arc. (Illustration: [Moan, 2003a])

Requiring equilibrium in s -direction:

$$q_s ds + (N + dN - N) + Q d\theta = 0 \quad (6.26)$$

inserting $d\theta = ds/R$ into eq. 6.26 give:

$$q_s + \frac{\partial N}{\partial s} - \frac{Q}{R} = 0 \quad (6.27)$$

similar in z -direction:

$$q_z + \frac{\partial Q}{\partial s} - \frac{Q}{R} = 0 \quad (6.28)$$

Fig. 6.4b show the displacement of the middle surface when the element deforms because of the applied forces in 6.4a. The total length change Δds due to the deformation is given by:

$$\Delta ds = \frac{\partial u}{\partial s} ds + w ds = \frac{\partial u}{\partial s} ds + \frac{w}{R} ds \quad (6.29)$$

The slope of the middle surface due to the deformation is given by:

$$\theta_s = \frac{dw}{ds} - \frac{u}{R} \quad (6.30)$$

The second term in 6.30 represents the contribution from the arc undergoing pure axial displacement, while the first term is known from straight beams.

Based on eq. 6.30, the curvature is given by:

$$\kappa_s = \frac{d\theta_s}{ds} = \frac{d^2 w}{ds^2} - \frac{du}{R ds} \quad (6.31)$$

The total strain for the arc is given by eq. 6.32:

$$\epsilon_t = \epsilon_m + \epsilon_b = \epsilon_m - z\kappa \quad (6.32)$$

where ϵ_b represents the contribution from bending, and ϵ_m is the contribution from membrane action. The membrane, or axial, strain is defined as following:

$$\epsilon_m = \frac{\Delta ds}{ds} = \frac{\partial u}{\partial s} + \frac{w}{R} \quad (6.33)$$

The stiffness relation can be obtained by principle of virtual displacements, in the same manner as shown for straight beam elements in sec. 6.1.2. The stiffness expression for an arc will however consist of one bending term and one additional term. [Moan, 2003a]

Arc as an assemble of straight beam elements

An arc can be modelled by straight beam elements (fig.6.5). The differences in element orientation result in coupling between axial forces (membrane action) and bending action. The displacements may be assumed cubic and linear for lateral and axial displacements, respectively. [Moan, 2003a]

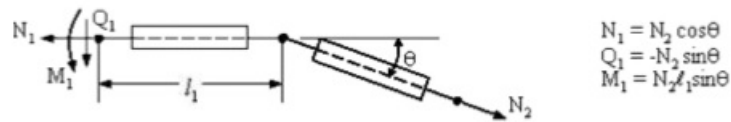


Figure 6.5: Illustration of the coupling between membrane and bending action due to element orientations (Illustration: [Moan, 2003a]).

6.2 Load cases used in static analysis of the SFT

Current

The current load was applied as an uniformly distributed load, or line load. The magnitude was, in accordance with section 4.2.3, set to $7.6kN/m$. Different profiles of the current were investigated in this thesis: uniform distributed current over the full length of the bridge in negative and positive y -direction, asymmetrically distributed current and a uniform distributed current over a mid-section of the bridge.

Traffic

Traffic loads were applied as uniformly distributed loads, or line loads, on each element. These loads were applied in the negative z -direction, meaning in the lateral direction. The magnitude, according to section 4.1.2, was set to $36kN/m$.

Selfweight

A built-in option for the self-weight in GeniE uses the material densities to calculate the total self-weight of the structure. An acceleration field corresponding to gravity is used, and Sestra converts the gravity load to a linearly varying load. [DNV-GL software, 2014] Thus, in addition to the actual material density of concrete, ballast and other weights are added to the material density to be included in the mass-matrix. This is especially important for the eigenvalue analysis in section 7. The material density is therefore adjusted to account for all contributions to the self-weight. This can easily be done by rearranging the equation of mass, eq.5.5, including all contributions.

$$A_e L \rho_{tot} = A_c L \rho_{RC} + m_{ballast} + m_{other} \quad (6.34)$$

The first term corresponds to the mass of concrete, where RC stands for reinforced concrete and A_e is the equivalent area, recall sec.3.3. ρ_{RC} was found based on the specific weight of reinforced concrete, assumed $25kN/m^3$ for the analysis carried out in [Engseth et al., 2016]. $m_{ballast}$ was found in section 5.6 and m_{other} is a sum of all other contributions, meaning pavement, curbstone, fire protection, cables and ducts, signals, call stations, marine growth, extra asphalt and illumination. The magnitude of these mass contributions are calculated according to tab. 4.1. All contributions are multiplied

with corresponding load factor, given in section 6.3. Because of the varying cross-section, there are five total material densities applied to the corresponding sections (see app.D, tab.D.1).

To ensure that the self-weight is applied in a correct manner by using the built-in option in GeniE, a simple calculation of a straight beam with constant average cross-section was carried out, see app. H.1 for calculation and sec. 6.5.1 for the results.

Buoyancy

Buoyancy is modeled using a built-in function in GeniE, executing Wajac. Hydro properties, called "hydro" in GeniE, has to be defined and assigned to the structure. These properties are flooding-properties and buoyancy areas. The environment data needed for the buoyancy calculation is the water density, water depth and waterline Z above the structure. The density of seawater was assumed $9.955kN/m^3$, in accordance with [Engseth et al., 2016] and [Vegdirektoratet, 2015]. The water depth, meaning the location of the seabed, is assumed $z = -200$ meters and the free surface at $z = 0$. The structure is located to a water depth of $z = -50m$.

The flooding property in GeniE tells whether the structure is flooded(=1), meaning filled with water or non-flooded(=0), meaning filled with air. [DNV-GL software, 2017] The straight beam elements are assumed non-flooded with buoyancy area equal to the concrete area plus the area of air inside the structure. Each cross-section of the varying part of the bridge is assigned corresponding buoyancy areas, which are calculated in advance. The buoyancy forces are thus calculated by Wajac as a vertical line load along the member.[DNV-GL software, 2016]

To check that the buoyancy is applied in the correct manner, the results from static analysis with buoyancy only is compared with the results obtained when buoyancy is applied manually as distributed loads. See results in app. H.2.

Axial compression force from PT-cables

In the feasibility study of a SFT for Sognefjorden, the same type of post-tension cables are chosen as for the base case. For Sognefjorden, a loss of post-tension is assumed 10%, giving an effective post-tension force (eq.6.35). [Statens Vegvesen, 2011]

$$P = 0.9 \cdot 0.8f_{p,0.1k}A_p \quad (6.35)$$

Assuming that the amount of post-tension cables for the base case are constant for the whole bridge length, the total effective post-tension force is calculated 428 MN, based on eq. 6.35. Thus, the concrete is subjected to a compression from the PT-cables with magnitude $-428MN$. Note that the compression force from PT-cables is not included in the static analysis in Sestra. However, the compression force is included in the stress calculations for SLS.

6.3 Load combinations

ULS

The load combination "ULS maximum buoyancy", tab. 6.1, is a load combination simulating worst ULS case with minimum weight. Thus, marine growth and variable wearing layer are not accounted for. The load factors are taken from [Engseth et al., 2016]. Because the buoyancy is dominating it is assumed that the most unfavourable is to assume no traffic loads.

Table 6.1: Load combination for ULS max buoyancy

Load	Load factor
Buoyancy	1
Weight of concrete structure	1
Weight of permanent solid ballast	1
Weight of water ballast	1
Sum permanent weights	0.99
Non-structural elements installed in place	0.85
Marine growth	0
Weight of water absorbed	0
Weight of variable wearing layer	-1.35
Post-tension	1.1
	Load factor unfavorable
Traffic	0
Current	1.12

SLS

The load combination "SLS", tab. 6.2, is a load combination for the serviceability limit state simulating the worst case in SLS. The load factors are taken from [Engseth et al., 2016].

Table 6.2: Load combination for SLS

Load	Load factor
Buoyancy	1
Weight of concrete structure	1
Weight of permanent solid ballast	1
Weight of water ballast	1
Sum permanent weights	1
Non-structural elements installed in place	1
Marine growth	1
Weight of water absorbed	1
Weight of variable wearing layer	1
Post-tension	1
	Load factor unfavorable
Traffic	0.7
Current	1

6.4 Stress calculations

This section gives the basis for conducting stress checks to ensure that the base case structure has desirable structural integrity. The theory and practical methods are gathered from [NS-EN1992, 2004], [Sørensen, 2013] and [Statens Vegvesen, 2011]. In the stress calculations it is assumed that tensile stresses are positive, forces are positive in tension and positive bending moments give tension at the underside. This corresponds to the convention in section 6.2 in [Sørensen, 2013]. In the feasibility study of a SFT for the Sognefjorden, it was required that the cross-section of the SFT remain uncracked in SLS to avoid leakage.[Statens Vegvesen, 2011] This requirement is in this thesis also employed for the base case SFT. Thus, for the stress calculations in SLS, the concrete cross-section is assumed uncracked.

Check of compressive stresses in the concrete in SLS

According to [NS-EN1992, 2004] 5.10.2.2, it is important to check for and to avoid local crushing of concrete in the ends of a post-tensioned structure. The compressive stress in the concrete should therefore be checked, to avoid both crushing and cracks in the longitudinal direction. According to 7.2(1), cracks may occur if the stress level for the characteristic load combination exceeds a critical value, which may affect the durability of the structure. The compressive stress in the concrete due to the post-tension force and other loads, which acts when the post-tension is applied, is limited to $\sigma_c \leq 0.6f_{ck}(t)$. $f_{ck}(t)$ is the compressive strength of concrete.[NS-EN1992, 2004]

Recall that in sec. 5.3.2, it was assumed that the number of PT-cables is constant for the whole length of the bridge and symmetrically placed around the neutral axis. See app.

E.2 for sketch of the placement of reinforcements and PT-cables. Moments from longitudinal PT-cables are neglected because the contributions above and below the centre of gravity will cancel each other if the concrete cross-section is assumed uncracked.

The compression stresses in the transformed concrete cross-section are calculated based on the procedure in sec. 6.2 in [Sørensen, 2013]. It is assumed that the axial compression forces from applied current and PT-cables, together with the bending moments due to net vertical forces and current, acts in the reinforced concrete cross-section centre of gravity.

$$\sigma_c = \frac{P}{A_T} + \frac{N_{xx}}{A_T} + \frac{M_{xz}y}{I_{z,t}}f_m + \frac{M_{xy}z}{I_{y,t}}f_m \quad (6.36)$$

The stresses are found by eq. 6.36 by inserting the right signs for the moments, forces and actual value for y and z . The stresses can thus be found at desired locations in the cross-section. P is the axial compression force from the PT-cables, N_{xx} is the axial force from the current acting in the negative y -direction, M_{xz} is the bending moment due to the current acting in the negative y -direction and finally M_{xy} is the bending moment due to net vertical forces (buoyancy, traffic and self-weight). $f_{ck}(t)$ is 55 MPa for the base case. f_m is an amplification factor due to the axial compression from PT-cables.

Equation 6.36 is adapted from [Sørensen, 2013], but include some modifications. First, the equation is modified to include bending moment from the transverse current load. Next, the bending moments are amplified by an amplification factor f_m due to the axial compression from the PT-cables. Recall section 6.1.1.

Check of tensile stresses in the concrete in SLS

According to [NS-EN1992, 2004] 7.1(2), the concrete cross-section should be considered un-cracked in the calculations of stresses, provided that the tensile stresses in the concrete is below f_{ctm} , which is the tensile strength of concrete. If this is not the case, the stress calculations should be carried out based on a cracked cross-section.

$$\sigma_{cs} = \frac{P}{A_T} + \frac{N_{xx}}{A_T} + \frac{M_{xz}y}{I_{z,t}}f_m + \frac{M_{xy}z}{I_{y,t}}f_m \quad (6.37)$$

To find the critical current condition for the base case and the present signs of the different terms in eq.6.37, a sensitivity study of the axial forces for different current conditions were conducted. Results are given in app.G.1.1

6.5 Results from static analysis

6.5.1 Results from Sestra compared to hand-calculations

Table 6.3: Comparison of results for the bending moments about y-axis from hand calculations and SESAM. Straight bridge configuration with constant average cross-section is assumed here.

	Hand calc. (MNm)	SESAM (MNm)
M_{end}	5887	5885
M_{mid}	-2943	-2942

6.5.2 Base case static analysis results

Amplification factor due to axial compression from PT-cables

Table 6.4: Amplification factor for straight bridge configuration with fixed ends and constant average cross-section.

Parameter	Unit	Value
Axial compression from PT-cables	(MN)	428
Euler buckling load	(MN)	7438
Amplification factor	(-)	1.063

Results for ultimate limit state with max buoyancy

Table 6.5: Reaction forces, ULS max buoyancy

	Results
F _x (MN)	-8.988
F _y (MN)	2.553
F _z (MN)	-45.758

Table 6.6: Bending moments and torsion moment, ULS max buoyancy

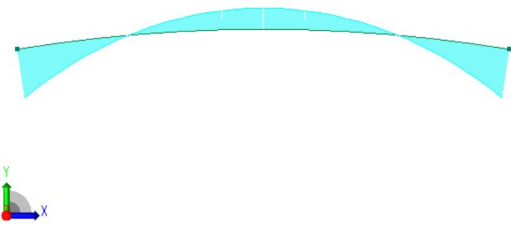
	Results
$M_{xy,ends}$ (GNm)	5.818
$M_{xy,mid}$ (GNm)	-2.955
$M_{xz,ends}$ (GNm)	0.114
$M_{xz,mid}$ (MNm)	-48.773
$N_{xx,max}$ (MN)	9.267

Force: [N], Length: [m]
 Beam Forces - Mxy
 Min: -2.95471e+009
 Max: 5.81799e+009



(a) Net moment distribution of bending moment about y-axis due to forces applied in z-direction.

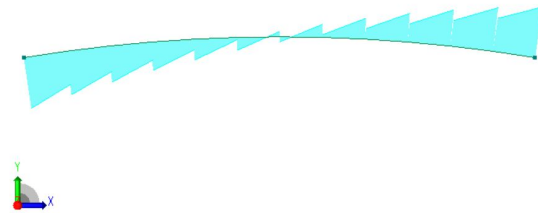
Force: [N], Length: [m]
 Beam Forces - Mxz
 Min: -4.87715e+007
 Max: 1.14365e+008



(b) Bending moment about z-direction due to current applied in positive y-direction.

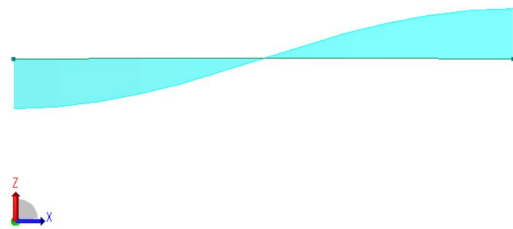
Figure 6.6: Bending moment distribution

Force: [N], Length: [m]
 Beam Forces - Nxy
 Min: -1.19387e+006
 Max: 1.19366e+006



(a) Shear force distribution in y-direction due to current forces applied in positive y-direction.

Force: [N], Length: [m]
 Beam Forces - Nxz
 Min: -4.57576e+007
 Max: 4.57583e+007



(b) Net shear force distribution in z-direction.

Figure 6.7: Shear force distributions

Force: [N], Length: [m]
 Beam Forces - Nxx
 Min: 8.98692e+006
 Max: 9.26661e+006

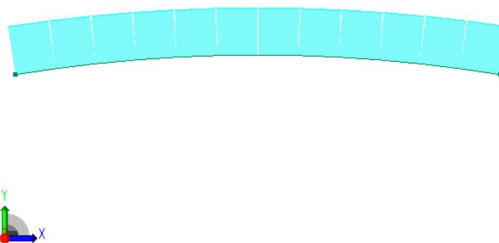


Figure 6.8: Axial force distribution due to current applied in positive y-direction.

Force: [N], Length: [m]
 Beam Forces - Mxx
 Min: -1.69498e+008
 Max: 1.69498e+008

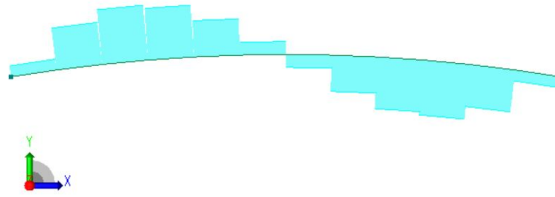


Figure 6.9: Net torsion moment distribution.

Results for serviceability limit state

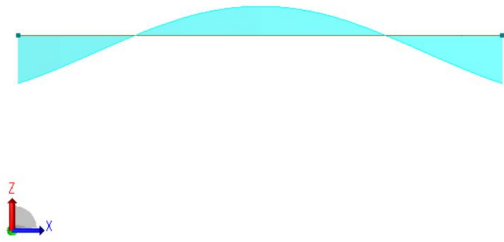
Table 6.7: Bending moments, torsion moment, axial forces and reaction forces for base case, SLS. The bending moments include an amplification factors due to compression force from PT-cables.

	Results Sestra
$M_{xy,ends}$ (GNm)	2.65
$M_{xy,mid}$ (GNm)	-1.59
$M_{xz,ends}$ (MNm)	108.54
$M_{xz,mid}$ (MNm)	-46.29
$M_{xx,max}$ (MNm)	81.32
N_{xx} (MN)	8.274
F_x (MN)	-8.025
F_y (MN)	2.279
F_z (MN)	-13.59

Table 6.8: Displacements for base case, SLS. Including amplification factor due to compression force from PT-cables.

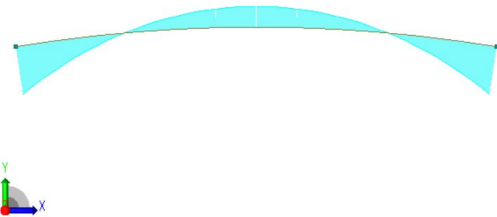
	Results
u (mm)	0.28
v (mm)	13.51
w (m)	0.52

Force: [N], Length: [m]
 Beam Forces - Mxy
 Min: -1.49502e+009
 Max: 2.49761e+009



(a) Moment distribution about y-axis

Force: [N], Length: [m]
 Beam Forces - Mxz
 Min: -4.3546e+007
 Max: 1.02112e+008



(b) Net moment distribution about z-axis

Figure 6.10: Bending moment distributions

Force: [N], Length: [m]
 Beam Forces - Nxx
 Min: 8.02403e+006
 Max: 8.27376e+006

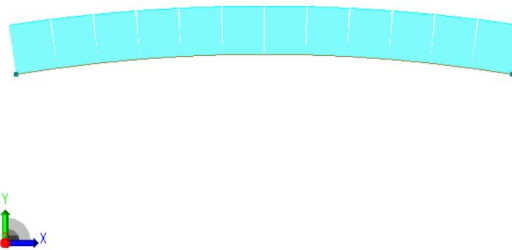
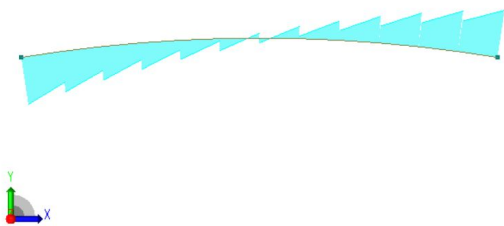


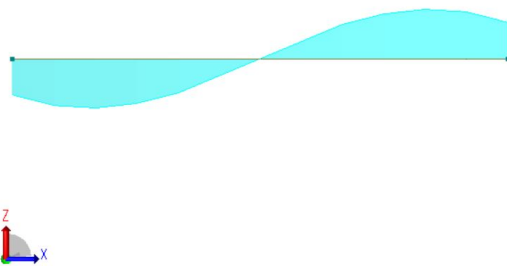
Figure 6.11: Axial force due to current applied in positive y-direction.

Force: [N], Length: [m]
 Beam Forces - Nxy
 Min: -1.06593e+006
 Max: 1.06593e+006



(a) Distribution of shear force in y-direction

Force: [N], Length: [m]
 Beam Forces - Nxz
 Min: -1.86851e+007
 Max: 1.86851e+007



(b) Distribution of net shear force in z-direction

Figure 6.12: Shear force distributions

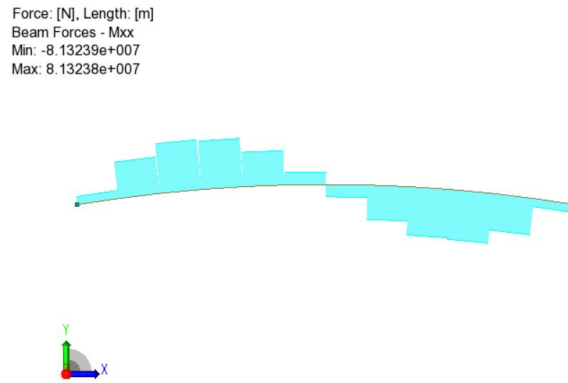


Figure 6.13: Net torsion moment about x-axis

6.5.3 Results from stress calculations for base case

Check of compression stress in concrete in SLS

Table 6.9: Calculated maximum compression stresses in concrete σ_c for SLS. The results are given in N/mm^2 and in percent of the compression strength of the base case bridge.

Location	σ_c (N/mm^2)	Utilization (%)
At bridge ends	-19.24	58.3
At midspan	-16.813	50.9

Check of tensile stress in concrete in SLS

Table 6.10: Calculated maximum tensile stresses in concrete σ_{cs} for SLS. The results are given in N/mm^2 and in percent of the tensile strength of the base case bridge.

Location	σ_{cs} (N/mm^2)	Utilization (%)
At bridge ends	5.70	135.7
At midspan	2.26	53.8

6.5.4 Results from parameter study with curve height

The results below does not include effects from PT-cables and reinforcements for simplicity. Thus, I_y and I_z are used.

Table 6.11: The curve heights used in the parameter study with associated element lengths and total bridge length. The number of elements are 12 for all curve heights.

C (m)	L_e (m)	L_{bridge} (m)
0	49.7666	597.2
24.25	50.0000	600.0
53	50.7917	609.6
60	51.0719	612.9

Table 6.12: SLS reaction forces, bending moments and axial forces for different curve heights with the case of a negative current applied to the full length of the bridge.

Curve height	0m	24.25m	53.0m	60m
$M_{xy,ends}$ (GNm)	2.605	2.500	2.628	2.672
$M_{xy,mid}$ (GNm)	-1.572	-1.492	-1.526	-1.538
$M_{xz,ends}$ (MNm)	-237.36	-100.09	-31.16	-24.65
$M_{xz,mid}$ (MNm)	101.45	42.57	14.41	12.05
$M_{xx,max}$ (MNm)	0	81.08	177.03	200.20
N_{xx} (MN)	0	-8.397	-6.075	-5.63
F_x (MN)	0	8.15	5.63	5.14
F_y (MN)	2.26	2.28	2.32	2.33
F_z (MN)	-14.43	-13.59	-13.82	-13.89

Table 6.13: SLS displacements for different curve heights.

Curve height	0m	24.25m	53.0m	60m
u (mm)	0	0.28	0.19	0.17
v (mm)	-30.4	-12.9	-4.29	-3.5
w (m)	0.524	0.508	0.553	0.570

6.6 Discussion of static analysis results

Hand calculations compared to results from Sestra

The results from Sestra are similar to those obtained from hand calculations of the self-weight, tab.6.3. Note again that this calculation was done with a straight model of the bridge with constant average cross-section for simplicity. The FEM-solution slightly underestimates the bending moments and forces. Since the results from Sesam deviates from the hand-calculations with less than one percent it is assumed that the deviations are a result of round-off errors. It is concluded that the FEM-model give reasonable results when the bridge is subjected to the self-weight of reinforced concrete.

Discussion of static analysis results for base case

The load combinations and load factors were chosen based on the chart given in [Engseth et al., 2016], see app.A.1. Two load combinations were investigated in this thesis, the serviceability limit state case and the ultimate limit state case with maximum buoyancy. Other load combinations should also be investigated, like the case of minimum buoyancy, maximum weight and traffic for instance. For the SLS combination, the load factor for traffic loads was set to 0.7, according to the chart. With the ballast amount used for the base case, the net vertical loads were dominated by buoyancy. An even worse scenario in the SLS combination will thus be no traffic loads.

Figures 6.6a and 6.7b show the net moment distribution for bending moment about y-axis and corresponding shear forces in z-direction. The largest values of the bending moments are located at the two ends of the bridge, giving tension on the underside. At midspan the value is approximately half the value at the ends, and give tension on the upper side. This is similar to the moment distribution for a simple straight beam with clamped support, subjected to uniform distributed load. It is observed that buoyancy is dominating for this load combination. The maximum bending moment is 5.818 GPa , which is a relatively high value. To avoid cracking of the concrete due to bending moments and shear forces, an assessment of necessary reinforcements should be carried out. The procedure for this is described in [Sørensen, 2013]. The bending moments can also be lowered by optimizing the cross-section and ballast amount. Increasing e.g. the cross-section thicknesses will increase the mass, which again will counter-act the buoyancy and result in lower bending moments and shear forces.

The reaction forces in x-direction and y-direction are results from applying current loads in y-direction. Because the bridge is curved, the current loads will have components in both x- and y-direction because of the eccentricities of the straight beam elements. The applied current loads produces both axial forces in the bridge and bending moments about z-direction, which is illustrated in figures 6.6b and 6.8. The corresponding shear force distribution in y-direction is given in fig.6.7a. As earlier explained in section 6.1.2, the transverse loads are carried by both membrane and bending action due to the horizontally curved configuration.

Fig.6.9 show the moment distribution for torsion moment about z-axis. The torsion moment is due to the fact that the bridge is curved. The gravity and other inertia loads act in the centre of gravity. If the centre of gravity does not coincide with the shear centre the consequence is torsion.[DNV-GL software, 2014] Torsion moments on concrete structures may result in cracking of the concrete.[Sørensen, 2013] Therefore, an assessment checking whether it is necessary with torsion reinforcement should be carried out. The procedure for this is given in [Sørensen, 2013].

The tables 6.7 and 6.8 show results from static analysis with the SLS load combination. Because of the applied current load, there are small displacements in x- and y-direction. The limitation of short time deflections in the horizontal direction was set to $L/200$, corresponding to 3 m.[Engseth et al., 2016] Thus, the horizontal displacements are within the limitation and therefore acceptable. The lateral displacement is 0.52 m. The limitation of short time deflection in vertical direction was set to $L/350$, corresponding to 1.71 m.[Engseth et al., 2016] Thus, the vertical displacement calculated from Sestra is also acceptable according to the limitations.

Fig.6.10a shows the bending moment about y-axis due to applied forces in z-direction. Fig.6.10b shows the bending moment distribution about z-axis, due to applied forces in y-direction. The shape of the bending moment distributions are similar to those in the ULS maximum buoyancy load combination. Compared to the results from SLS, tab.6.7, the bending moment about y-axis is nearly doubled in ULS maximum buoyancy. Recall that the SLS load combination includes a traffic load with load factor 0.7. The traffic loads are applied in negative z-direction which unloads the dominating buoyancy in contrast to the ULS maximum buoyancy load combination. The torsion moment distribution given in fig 6.13 for SLS is also similar to that of the ULS maximum buoyancy, but the maximum values are lowered due to the applied traffic loads

and higher weights. However, the positive vertical displacement of $0.52m$ and the moment distribution about y-axis show that the buoyancy is still the dominating load in z-direction.

Fig 6.11 show the axial force distribution when the current is applied in positive y-direction. The result is a constant tension force in the structure. This seems reasonable, because the current is applied at the underside of the arc, forcing the arc to stretch and thus resulting in tension forces. It is not favourable to have tensile forces in a concrete structure, because the concrete is sensitive to tensile forces, which may result in cracking. It is therefore important that the structure is reinforced with adequate post-tension cables and reinforcement to carry tensile forces.

For both ULS and SLS conditions, the current loads can be applied in both positive and negative y-direction. The results from the sensitivity study of current direction and profiles can be found in app. G.1.1. If the current is applied in the negative y-direction the bending moment about z-axis gives tension at the upper side at the bridge ends, and tension at the underside at midspan (fig.G.1). The current loads now produces compression in the structure (fig.G.1a). This seem reasonable, because the current is applied at the upper side of the arc, forcing the arc to compress, which again results in compression forces. High compression forces in a concrete structure may result in crushing. A check should therefore be carried out, checking whether this might be a problem.

The main finding of the sensitivity study is that uniform current applied over the whole bridge length gives the highest bending moments and axial forces from current in the structure. This was as expected. However, an asymmetrically distributed current produces a more complicated bending moment (fig. G.3) giving tension at the upper side at one end, and compression at the underside at the other. The current forces also produces axial forces where one part of the structure is given an axial compression and another part tension.

Influence of PT-cables on static response

The average increase of moment of inertia, when accounting for reinforcements and PT-cables in transformed concrete cross-sections, is 3.89% for I_z and 3.24% for I_y . The results from static analysis discussed in the latter section were based on a transformed concrete cross-section. Thus, the contributions from reinforcements and PT-cables were included in the bending stiffness. However, the tension force in the PT-cables produce axial compression forces in the concrete. With a post-tension force loss of 10% and a total amount of 78 longitudinal cables the total axial tension force in the cables was calculated $428MN$ (tab.6.4). Thus, the concrete is subjected to a compression force with magnitude $428MN$.

If the compression force is too high, global buckling can be a problem. The euler buckling load for a straight beam was calculated according to section 6.1.1. It was found that the compression force due to the PT-cables was 5.75% of the euler buckling load. Thus, it is further assumed that global buckling is not a relevant problem for the base case structure. In the stress calculations, the influence of the PT-cables on the stresses is accounted for by including the compressive stresses from the PT-cables and by mul-

tipling the bending moments with an amplification factor. The highest amplification factor due to the axial compression from PT-cables was calculated according to eq.6.17 in section 6.1.1. The result was an amplification factor of 1.063 (tab.6.4). The amplification factor was calculated based on a straight configuration of the bridge with a constant average cross-section (see sec.6.1.1). That is, the euler buckling load was calculated based on a simple straight beam model rather than a curved model. For a better accuracy of the amplification factor, the euler buckling load should be calculated based on a curved beam model rather than a straight one.

Check of concrete stresses in SLS

A check of compression stresses was carried out at the most critical regions with respect to compression at supports and at mid-span. Based on the bending moments about y- and z-directions (fig. 6.10a and 6.10b), the most critical region at the supports, with respect to compression, was found in the upper right corner of the cross-section. In similar way, the most critical region was for the midspan found in the left corner in the lower slab.

The results from check of compressive stresses in concrete are given in tab.6.9. The maximal compressive stress in the concrete was calculated $\sigma_c = -19.24 \text{ N/mm}^2$ at bridge ends, which corresponds to 58.3% of the allowable value. The check of tensile stresses was carried out for the most critical current condition with respect to tension. For the base case, the critical condition is a current applied in the positive y-direction, which results in axial tension N_{xx} (see. G.2a.). It also results in a bending moment giving tension on the right side of the cross-section at the two ends (see. G.2). The results from the check of tensile stresses in concrete are given in tab.6.10. The maximal tensile stress was calculated $\sigma = 5.7 \text{ N/mm}^2$ at bridge ends, which is 35.7% higher than the characteristic tensile strength of the concrete. At midspan, the maximal tensile stress was calculated 2.26 N/mm^2 , which corresponds to 53.8% of the characteristic tensile strength. Since the maximal tensile stress exceeds the allowable value at bridge ends, the stress calculations at this location should be based on a cracked cross-section. However, one of the requirements for SLS was that the concrete cross-section should remain uncracked to avoid leakage. By investigating the terms in eq.6.37 it was observed that the contribution from bending moment about y-axis was the dominating one. Thus, the net vertical forces should be lowered to avoid cracking of the concrete.

N400 states that for structures carried by or partly by buoyancy, the specific weight of reinforced concrete shall be calculated based on the amount of reinforcements, which is added to the specific weight of mass concrete (24 kN/m^3). The technical report [Engseth et al., 2016] does not provide sufficient information about the reinforcements, and an estimate of the minimum reinforcements were therefore estimated in this thesis to account for the reinforcements when calculating the transformed concrete area. However, only the minimum longitudinal reinforcements were calculated. To have the correct specific weight of reinforced concrete for this case, a full assessment of all the reinforcements should be carried out. In the technical report, they used 26.5 kN/m^3 for the specific weight in their hand-calculations, but 25 kN/m^3 for the analysis. Based on the amount of longitudinal reinforcements that I have calculated, it is assumed in this thesis that the correct specific weight of reinforced concrete will be somewhere be-

tween $25\text{kN}/\text{m}^3$ and $26.5\text{kN}/\text{m}^3$. The static analysis was therefore rerun with a specific weight of $26.5\text{kN}/\text{m}^3$, giving the results in app.G.1.2.

If a specific weight of concrete of $26.5\text{kN}/\text{m}^3$ is used, the net bending moments due to vertical loads are reduced with a factor of ten in SLS. In contrast to the base case, the largest bending moment is here located at midspan. With a positive current load, the concrete stresses were calculated at the most critical location with respect to tension at midspan. Here, the maximal concrete stress was calculated $-5.160\text{N}/\text{mm}^2$. Thus, the concrete is in compression even though the bridge is subjected to an axial tension force due to the current loads.

An alternative way to balance the buoyancy is to increase the ballast amount or the wall thickness of the concrete section. To investigate the sensitivity of the tensile stresses in concrete to the ballast amount, two other ballast cases were investigated, see app.G.1.3. One of the two ballast cases considered was a ballast percent increase of 3%. The resulting maximal tensile stresses at the bridge ends was calculated $\sigma = 4.11\text{ N}/\text{mm}^2$, corresponding to 97.9% of the characteristic tensile strength of the concrete. Thus, by increasing the ballast percent by 3%, the maximal tensile stresses in the concrete is just below the allowable value.

Parameter study with curve height

The objective of this parameter study was to investigate the influence of introducing a curve height with respect to the static response. Recall section 6.1.2. Note that increasing the curve height will also increase the length of the bridge. Keeping the airline-distance between the abutments constant equal to 598.6m, the total length of the bridge for curve heights are given in tab.6.11. Three curve heights were investigated in Sestra, in addition to a straight bridge model with zero curve height. The results from parameter study with curve height with respect to static response are given in tables 6.12 and 6.13. It is observed, from the first table, that the net bending moments about y-axis reduces when the first curve height is introduced, compared to the straight bridge. This was unexpected. However, the net bending moment increases as the curve height is increased further. Increasing the curve height also means increasing the length of the bridge, which again increases buoyancy and weight.

The same table gives the results for bending moments about z-axis and axial forces. The bending moment reduces as the curve height increases. For the straight bridge, there are no axial forces due to transverse loads. When introducing a curve height, it is observed that axial forces due to the transverse loads are present. This is a result of curving the structure, because the transverse loads are carried by both axial forces and bending moments (fig. 6.5). When the curve height is increased further, the axial forces reduces. When the curve height increase, so does the angle between the normal component of the current force and the axial forces in the beams, and the result is decreased axial forces.

However, the torsional moment increases with increasing curve height. When introducing a curve height, the total centre of gravity is translated in y-direction. When the curve height is increased, the centre of gravity translates further in y-direction. This causes increased torsion-arm and thus higher torsion moments. The reaction forces

are also given in tab.6.12. As for the bending moment about y-axis, the reaction forces in z-direction reduces as a curve height is introduced compared to the straight bridge. Increasing the curve height results in slightly increased reaction forces in z-direction. This is also the case for the displacement in z-direction (tab.6.13). Meaning, the introduction of a curve height reduces the displacement in z-direction, but when increasing the curve height further the displacements are increased. For the straight configuration, there are no reaction forces in x-direction due to no difference in the element orientation. When introducing a curve height, reaction forces in x-direction becomes present due to the applied transverse current loads and the difference in element orientation. This is also the case for the displacement in x-direction. The reaction force in y-direction increases with increasing curve height. The displacement in y-direction is however reduced for increasing curve height.

Chapter 7

Eigenvalue analysis

This chapter concerns an extensive study of the natural frequencies and mode shapes of the SFT proposed for the Digernessund. First, the theory for vibrating beams are given. That is, analytical solutions of the eigenfrequencies for straight beams, curved beams and beams subjected to axial loading. These solutions are calculated to check if the results from the analytical solutions coincides with the numerical results in GeniE and Abaqus.

The results of the eigenvalue analyses are given in section 7.4. First, the results for a straight configuration of the bridge with a constant average cross-section are given. The results from a convergence test are also included here. Next, the results for a horizontally curved bridge, with constant average cross-section, are given. This curved configuration corresponds to the configuration of the bridge given in the technical report [Engseth et al., 2016], with a curve height of $c = 24.25m$.

The result section also includes results from a parameter study of the curve height. The curve height for which the first and second horizontal mode shape change order was first calculated analytically. This was done by setting eq. 7.3 equal to eq.7.1, with the values for fixed supports and $n = 2$, and then solve for the curve height \bar{C} . Then, a parameter study for the curve height was carries out in both GeniE and Abaqus to see if the analytically calculated curve height coincides with the numerical results. Five different curve heights were investigated in the two programs to find the changing point. These were 50m, 52.5m, 53m, 55m and 56m. The results for the curve heights $C = 24.25m$, $C = 53m$ and $C = 56m$ are given in the result section.

The influence of the PT-cables and reinforcements on the eigenfrequencies is also included in the results. The reductions in percentage of the eigenfrequencies are first calculated analytically, according to section 7.1. An analysis in Abaqus was then carried out to compare the results with the analytical solution (see app.G.2.4).

The last result-section includes the numerical results from Sestra for a more realistic model of the SFT, which also is the base case. That is, a curved configuration with $c = 24.5m$, varying cross-section and including the effects of the PT-cables and reinforcements by transformed moments of inertia. Here, the mode shapes are also given. The results are shown for element size 50m.

7.1 Analytical solutions for eigenvalue analysis

7.1.1 Oscillating beam

For a simply supported beam with a constant cross-section, the angular frequency ω_n^0 is given by eq.7.1 [Larsen, 2014]. The values $\bar{\omega}_n$ needed for a beam with fixed ends, and for a beam with simply supported ends, are given in tab. 7.1.

$$\omega_n^0 = \bar{\omega}_n \sqrt{\frac{EI}{ml^4}} \quad (7.1)$$

Table 7.1: Eigenvalues used in equation 7.1.[Larsen, 2014]

Support	n=1	n=2	n=3	n>3
Simply supported	0	9.872	39.48	$(n-1)^2\pi^2$
Fixed	22.37	61.67	120.9	$(\frac{2n+1}{2}\pi)^2$

For the case of simply support, the equation 7.1 represents the exact solution to the differential equation, while the other case is an approximation.

7.1.2 Oscillating curved beams

The theory in this section is gathered from [A. R. Reinertsen, 1988]. The derivation of natural frequencies in sway for curved beams can be found in chapter 3 in the mentioned reference. It is based on energy principles and takes advantage of the Hamilton's principle.

Curved beam with rotation free ends

A curved beam with rotation free ends is illustrated in figure 7.1. The first and second mode shapes are sketched in figure 7.2. In figure 7.2a, \bar{C} represents the initial curve height and C is the variation of the curve height during oscillation.

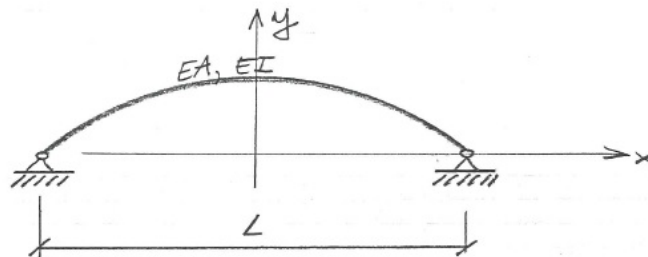
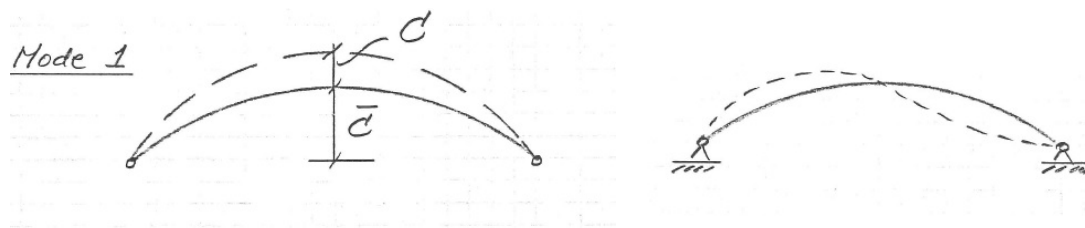


Figure 7.1: Sketch of a curved beam with rotation free ends. Illustration:[A. R. Reinertsen, 1988]



(a) First mode shape in sway.

(b) Second mode shape in sway.

Figure 7.2: First and second mode shape for curved beam with rotation free ends. Illustrations:[A. R. Reinertsen, 1988]

For a curved bridge with rotation free ends, the eigenfrequency for the first horizontal mode can be estimated by eq.7.2.

$$\omega = \frac{\pi^2}{L^2} \sqrt{\frac{EI_z}{m}} \cdot \sqrt{1 + \frac{\bar{C}^2}{2i_r^2}} \quad (7.2)$$

where $i_r = \sqrt{\frac{I_z}{A}}$ is the radius of gyration and \bar{C} is the curve height in the horizontal plane. For mode 2, 3, ..., the membrane action in the curve will not be activated. [A. R. Reinertsen, 1988] Thus, the eigenfrequencies for modes 2, 3, ... can be estimated by eq.7.1.

Curved beam with fixed ends

A curved beam with fixed ends is illustrated in figure 7.3. The first and second mode shapes are sketched in figure 7.4. In figure 7.4a, \bar{C} again represents the initial curve height and C is the variation of the curve height during oscillation.

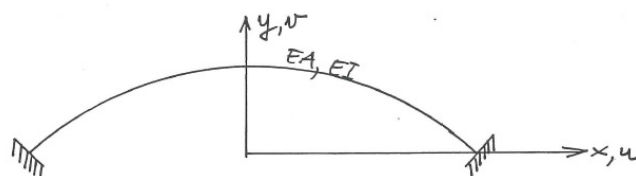


Figure 7.3: Sketch of a curved beam with fixed ends. Illustration:[A. R. Reinertsen, 1988]

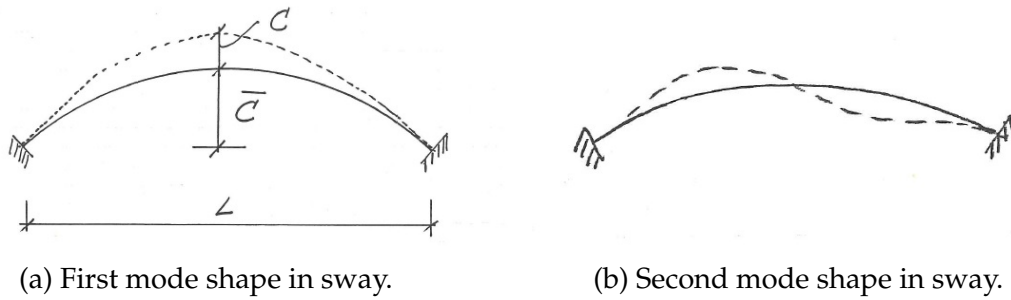


Figure 7.4: First and second mode shape for curved beam with fixed ends. Illustrations:[A. R. Reinertsen, 1988]

For a curved bridge with fixed ends, the eigenfrequency for the first horizontal mode can be estimated by eq. 7.3. [A. R. Reinertsen, 1988]:

$$\omega = \frac{\pi^2}{L^2} \sqrt{\frac{16EI_z}{3m}} \cdot \sqrt{1 + 0.100 \frac{\bar{C}^2}{i_r^2}} \quad (7.3)$$

Eigenfrequencies for modes 2, 3, ... for curved beam with fixed ends are similar to those of curved beam with rotation free ends (eq.7.1).

7.1.3 Influence of axial forces on oscillating beams

Axial forces can be important for transverse vibration of beams. According to [Clough and Penzien, 2003], both frequency and the vibration mode shapes are generally modified by an axial load. The structure can be evaluated in the same way as for a system without axial forces. However, the geometric stiffness due to axial loading has to be included in the equation of motion. In the case of a compression force, the effect is a reduction of the effective stiffness of the structure and thus reduction of the vibration frequency. [Clough and Penzien, 2003]

Derivation of eigenfrequency for beams subjected to axial forces (eq. 7.4) can be found in section 3.4.4 in [Bergan et al., 1981]. Here, axial force N is considered positive for compression, and is assumed to be constant over the beam length.

$$\omega_n = \omega_n^0 \sqrt{1 - \frac{1}{n^2} \frac{N}{N_E}} \quad (7.4)$$

where ω_n^0 is the angular frequency for a system without axial force N , and N_E is the euler buckling load. This formula is not exact for all beam conditions but can be used as a good approximation.[Bergan et al., 1981] This equation is especially relevant when including the effects of PT-cables. The PT-cables and ordinary reinforcement are included by transformed moment of inertia. In addition, the beam is subjected to a compression force simulating the action on the concrete from PT-cables.

7.2 Modal analysis

The theory in this section is gathered from chapter 4 in [Langen and Sigbjornsson, 1979]. The dynamic equilibrium equation can be expressed by eq. 7.5.

$$\mathbf{M}\ddot{r} + \mathbf{C}\dot{r} + \mathbf{K}r = \mathbf{Q}(t) \quad (7.5)$$

with \mathbf{M} , \mathbf{C} and \mathbf{K} representing mass, damping and stiffness matrices respectively of a given structure. $\mathbf{Q}(t)$ represents external forces applied on the structure. r , \dot{r} and \ddot{r} represents the nodal response (displacement, velocity and acceleration respectively) to the applied external force. The dynamic equilibrium equation will be further explained and investigated in section 8.1.

For free undamped vibration we assume that there are no damping or external forces acting on the structure, i.e. $\mathbf{C} = 0$ and $\mathbf{Q}(t) = 0$.

Then, eq. 7.5 can be written:

$$\mathbf{M}\ddot{r} + \mathbf{K}r = 0 \quad (7.6)$$

It can be assumed that the vibration is harmonic, that is, that all points vibrate in the phase with the same frequency. Then, the motion can be expressed as $r = \phi \sin(\omega t)$. Inserting this into eq. 7.6 the general eigenvalue problem is obtained:

$$(\mathbf{K} - \omega^2 \mathbf{M})\phi = 0 \quad (7.7)$$

ϕ represents the eigenvector, which determines the mode of vibration, while ω is the angular frequency for the undamped, free and harmonic vibration. \mathbf{K} and \mathbf{M} are both symmetric and commonly positive. The mass matrix is either banded (for consistent mass) or diagonal (for concentrated mass). [Langen and Sigbjornsson, 1979]

7.3 Eigenvalue problem in Sestra

Sestra offers different alternative eigenvalue solvers. The Lanczos method is well suited for solving moderate sized to big problems when a few up to some hundred eigenvalues are desired. The aim of this method is to find the lowest frequencies and corresponding eigenvectors. [DNV-GL software, 2014] This eigenvalue solver is used for the present case.

The eigenvalues and eigenvectors described in section 7.2 have to satisfy the equation 7.8:

$$\mathbf{K}\Phi_i = \lambda_i \mathbf{M}\Phi_i \quad (7.8)$$

where \mathbf{K} is the global stiffness matrix, \mathbf{M} in the global mass matrix, λ_i is the eigenvalues and Φ_i is the eigenvectors or mode shapes for $i = 1, \dots, n$. n is the number of degrees of

freedom. Thus, the number of solutions to the general eigenvalue problem is equal to the number of degrees of freedom of the system. The eigenfrequencies, ω_i , of the finite element model can be found by taking the square root of the eigenvalues. The natural periods, or eigenperiods T_i may be found by:

$$T_i = \frac{1}{f_i} = \frac{2\pi}{\omega_i} \quad (7.9)$$

The eigenvectors are normalized with respect to the mass matrix, ie. $\Phi_i^T \mathbf{M} \Phi_i = 1$ for all i .

7.4 Results from eigenvalue analysis

7.4.1 Effects of PT-cables and reinforcements

Table 7.2: Reduction of eigenfrequency because of axial compression due to PT-cables.

Mode	w_n^0 (rad/s)	Reduction factor	w_n (rad/s)	Reduction (%)
1	0.687	0.9720	0.668	-2.825
2	1.895	0.9930	1.882	-0.699
3	3.715	0.9969	3.704	-0.310
4	6.135	0.9983	6.125	-0.174
5	9.165	0.9989	9.155	-0.111

7.4.2 Eigenvalue analysis results for base case

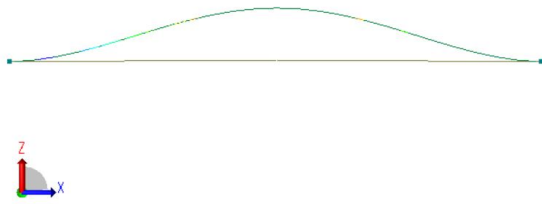
Table 7.3: Eigenfrequencies and periods for curved model, varying cross-section, obtained with Sestra and Abaqus. The deviations between the results from the two softwares are also given.

Mode	Sestra		Abaqus		Dev (%)
	f_n (1/s)	T_n (s)	f_n (1/s)	T_n (s)	
1	0.113	8.881	0.114	8.788	-1.05
2	0.194	5.160	0.195	5.134	-0.51
3	0.299	3.342	0.307	3.260	-2.44
4	0.333	2.999	0.345	2.901	-3.26
5	0.572	1.748	0.596	1.677	-4.05
6	0.639	1.564	0.673	1.486	-5.02
7	0.924	1.082	0.983	1.018	-5.94
8	1.023	0.977	1.093	0.915	-6.38
9	1.353	0.739	1.471	0.680	-8.05
10	1.489	0.672	1.647	0.607	-9.57

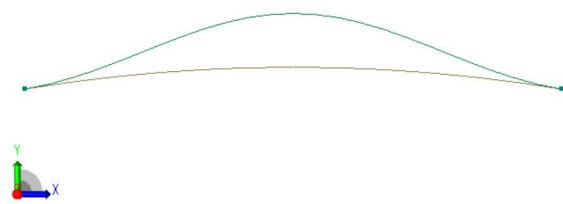
Table 7.4: Eigenperiod and frequency for the first mode for base case, including analytically calculated reduction factor due to PT-cables.

Mode	Sestra		Abaqus	
	f_n (1/s)	T_n (s)	f_n (1/s)	T_n (s)
1	0.109	9.137	0.111	9.041

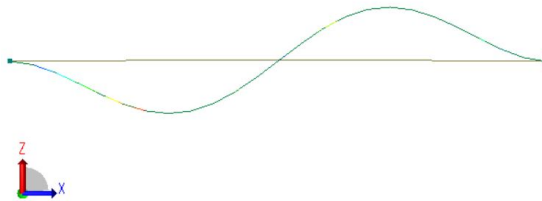
The ten first mode shapes are given in the figures 7.5 a-j below.



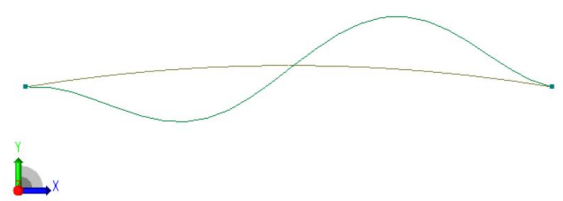
(a) Mode shape 1, vertical



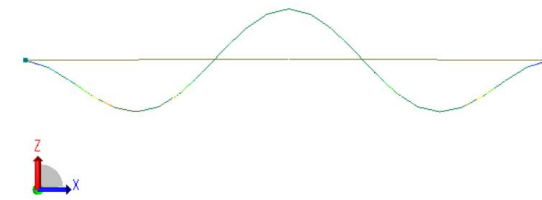
(b) Mode shape 2, horizontal



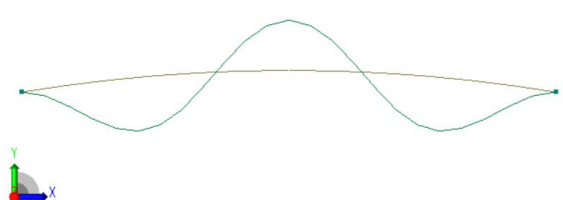
(c) Mode shape 3, vertical



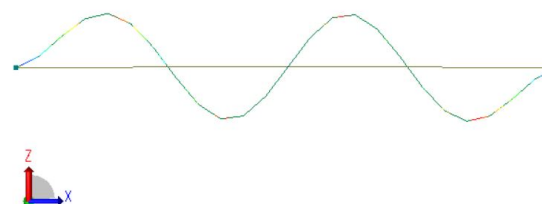
(d) Mode shape 4, horizontal



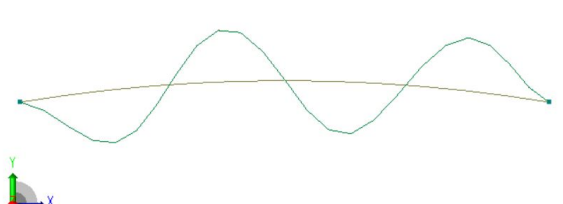
(e) Mode shape 5, vertical



(f) Mode shape 6, horizontal



(g) Mode shape 7, vertical



(h) Mode shape 8, horizontal

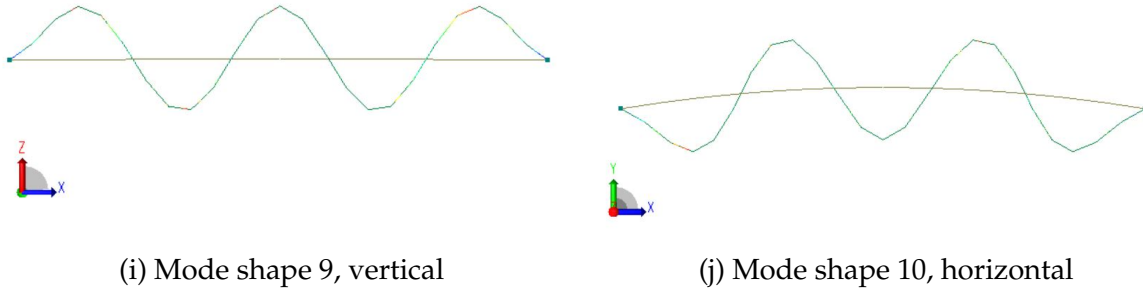


Figure 7.5: Mode shapes for base case.

7.4.3 Results from parameter study with curve height

Table 7.5: Curve heights in-which the order of the first and second horizontal mode shapes changes. f_2 corresponds to the first horizontal natural frequency.

Solution method	\bar{C} (m)	f_2 (1/s)	L_{tot} (m)
Analytical	49	0.331	608.4
GeniE	53	0.313	609.6
Abaqus	56	0.326	611.5

7.5 Discussion of eigenvalue analysis results

The results of eigenvalue analysis for the straight bridge model are given in app. G.2.1. As shown in tab. G.5 the numerical results from Sestra and Abaqus seem to coincide with the analytical results for the first five modes, with deviations less than \pm five percent. The deviations of eigenperiods from the analytical results (termed D_{an} in the table), do however increase for increasing mode number for both Sestra and Abaqus. With reference to the analytical results, Sestra slightly overestimates the eigenperiods, while Abaqus slightly underestimates them. The aim of the eigenvalue solver used in both programs is to find the lowest eigenfrequencies, and thus the highest eigenperiods. It can therefore be assumed that Sestra provides the most conservative results for the straight bridge model.

A convergence test was conducted for the straight bridge model. The results are given in app.G.2.1 tab.G.6. The eigenperiods seem to converge for reduced element size for all ten modes. The convergence rate is however higher for the first modes than for higher modes. This is expected, because higher modes are more sensitive to element size than lower modes. One of the reasons for that is that higher mode shapes is associated with higher amount of halfwaves to be represented. To represent the higher mode shapes accurately, there must be enough elements per halfwaves. The deviations from analytical solution for all element sizes are given in the same table. For the first six modes, the deviations from analytical solution are under five percent, and thus the results from Sestra seem to coincide with the analytical solutions for the six first eigenperiods. For higher modes, the deviations are higher than five percent and increases for increasing mode. The deviation for the higher modes also increases for

lower element sizes. As explained in the previous paragraph, the higher modes are more sensitive to element size. The analytical solution for $n > 3$ give approximated solutions, which may explain why the higher modes calculated by Sestra deviate more from the analytical solution than the first modes.

Influence of a curved model on eigenvalue analysis

In app.G.2.2, the results of eigenvalue analysis for curved bridge model with constant cross-section are given. As for the straight bridge results, both Sestra and Abaqus seem to coincide with the analytical results for the first modes. The exception here is the second mode, which is recognized as the first horizontal mode. Both Sestra and Abaqus underestimates this eigenfrequency compared to the analytical result. The second mode from Abaqus is however slightly closer to the analytical solution than the result from Sestra. The second mode of the curved model has increased eigenfrequency and thus reduced period compared to the second mode of the straight model. This is a consequence of the curved configuration of the bridge and thus membrane action in the curve, as described by [A. R. Reinertsen, 1988]. In the same reference, it is stated that the membrane action will not be activated for the following modes. This is observed when comparing the eigenfrequencies for the next modes from the curved model with the ones for the straight model, as they are quite similar.

Discussion of parameter study with curve height

The results from the parameter study of curve height are given in tab.7.5. The main objective of the parameter study with curve height was to investigate when the first and second horizontal mode shape changes order (fig. 7.5b and 7.5d). It was assumed that if the curve height was high enough, the first horizontal mode should include two halfwaves. Analytically, this curve height was found 49m. In Sestra, the curve height giving two halfwaves for the first horizontal mode was 53m, while in Abaqus the result was 56m. The six first modes for a curved SFT with a constant average cross-section are given in app.G.2.3, tab.G.9. From tab.G.9 it is observed that the eigenperiod increases for increasing curve height.

Influence of PT-cables

In table 7.2 ω_n^0 is given for the straight bridge model. This is the angular eigenfrequency including transformed moment of inertia for a system without axial force P. It is observed that these eigenfrequencies are higher than those without the contribution in bending stiffness from the PT-cables and reinforcements, given in tab. G.4. The increased eigenfrequencies are a result of using the transformed moment of inertias (see sec. 5.4.1 and app. F). The transformed moment of inertias contain contributions from the reinforcements and PT-cables, which also results in increased bending stiffness as described in sec.6.6. The increased eigenfrequencies due to the transformed moment of inertia can be explained by looking at eq. 7.1. From this, it is clear that increasing the bending stiffness will increase the eigenfrequency.

Table 7.2 also give the results for ω_n , which in this case includes a reduction factor due to the compression forces from the PT-cables. The eigenfrequencies are generally modified by this axial force, as explained in sec. 7.1.3. Here, it was stated that a compressive axial force will reduce the effective stiffness of the structure and thus reduce the vibration frequency. From tab.7.2, it is observed that the reduction for the first eigenfrequency is -2.83%. For the following modes, the reduction is smaller than -1%. It is therefore assumed that for higher modes, the reduction due to the compression force can be neglected. By investigating eq.7.4, it is observed that the reduction of the effective stiffness and the eigenfrequency is reduced for increasing mode number, which is also observed in table 7.2.

Discussion of results for base case

The results from eigenvalue analysis for the base case are given in section 7.4.2. The eigenfrequencies and periods calculated from both Sestra and Abaqus are given in tab.7.3. The results for the eigenperiods from Abaqus deviates from the results from Sestra. The deviations increase for increasing mode number. However, for the first five modes, the deviations are below five percent. Abaqus slightly underestimates the periods, compared to the results from Sestra. As for the case of a straight bridge, Sestra is thus assumed to give the most conservative results for the eigenperiods. The eigenfrequency for the first mode is multiplied by a reduction factor to account for the influence of the compression force from the PT-cables (tab.7.4). The first eigenperiod for the base case was thus calculated 9.14s. The second, corresponding to a horizontal mode with one half-wave, was calculated 5.16s by Sestra. The third and fourth, corresponding to vertical and horizontal mode with two half-waves respectively, were calculated 3.34s and 3.00s by Sestra. For increasing mode number, the eigenfrequencies are close.

The results from the eigenvalue analyses are different from the results calculated by the NPRA (tab.A.1). The eigenperiods calculated by Sestra and Abaqus deviates from the calculations by the NPRA by about 10-20%. Some of the reasons for this can be differences in the modeling, assumptions and rounding off. The information regarding the basis for the eigenvalue analysis in [Engseth et al., 2016], meaning assumptions and information about the FE-model used, are limited. By correspondence with Arianna Minoretti, representing the NPRA, it was found that the eigenvalue analysis done by the dr. techn Olav Olsen is based on a simplified model with a constant cross-section and no influence of the PT-cables and reinforcements. Because the results for the base case in this thesis are based on a model with varying cross-section, varying ballast and influence of PT-cables, it is expected that the results will deviate from the results calculated by the NPRA and dr. techn Olav Olsen.

Associated mode shapes from the analysis in Sestra are given in fig.7.5. The first mode shape represents a vertical mode according to the [Engseth et al., 2016], see fig. (A.2a). This is also the case for the first mode shape obtained in Sestra, fig. 7.5a. This is as expected, because the bending stiffness about y-direction (EI_y) is weak compared to the bending stiffness about z-direction (EI_z) for the SFT. The next mode shape represents a horizontal mode both in the technical report (fig.A.2b) and in Sestra (fig.7.5b). For increasing mode number (fig.7.5c-7.5j), the number of half-waves increases.

Recall the tables 3.7 and 3.8, which gives the data for wind and swell generated waves

estimated by the NPRA. The third and fourth eigenperiods of the structure (tab. 7.3) are within the ranges of the estimated peak periods for wind generated sea. These sea states are assumed to exhibit low energy levels [Xiang et al., 2017]. The two first eigenperiods are also within the range of common wave periods for ocean waves (recall section 4.2.5). The dynamic response excited by waves with wave periods close to these eigenperiods should be investigated to avoid resonance.

Chapter 8

Dynamic response analysis

The theory in this section is gathered from [Langen and Sigbjornsson, 1979]. In dynamic response analysis, also called vibration analysis, the response due to time-varying loads are investigated. The response can here be the motion or velocity of the structure due to the time-varying loads for instance, or bending moments.

This section includes method for dynamic response analysis, a brief introduction to solution methods of the dynamic equilibrium equation and an example of a time-varying load relevant for marine bridges, meaning wave loads. The properties of a vibrating system is also described, meaning mass, stiffness and damping.

8.1 Theory of dynamic analysis

8.1.1 Dynamic equilibrium equation

If the motion of the structure is sufficiently large, inertia and damping loads have to be accounted for.[Moan, 2003a] Considering a rigid body with one translational degree-of-freedom (dof) u and mass m , the dynamic equilibrium equation for a one degree-of-freedom system is given by eq. 8.1 [Langen and Sigbjornsson, 1979]:

$$m\ddot{u} + c\dot{u} + ku = Q(t) \quad (8.1)$$

The first term on the left hand side represents the inertia load, the second term represents the damping load and the third term represent the stiffness known from static analysis. \dot{u} is the velocity of the system, \ddot{u} is the acceleration, c is the viscous damping coefficient of the system, k is the stiffness of the system and Q is the external loads.[Langen and Sigbjornsson, 1979]

The number of dofs is equal to the number of translations and rotations needed to describe the deformation state of the system. For a dynamic system, the dofs must be chosen such that the inertia forces can be represented accurately enough.[Langen and Sigbjornsson, 1979] As described in [Larsen, 2014], an example of a system with more

than one degree-of-freedom is a vibrating beam. It has infinitely number of degrees-of-freedoms because the deformation of the beam is described by a continuous function, which again is calculated based on infinitely number of points. The continuous system has to be transformed into a discrete system with a finite number of degrees-of-freedoms to solve the dynamic equilibrium equation. [Larsen, 2014] This can be done by means of two different methods, discretizing the structure into finite elements with concentrated mass, or by expressing the deformations by one or more assumed shape functions $\phi(x)$. The latter method, generalized dofs, depends on how accurate the assumed displacement shape is, and is employed by the finite element method and the Rayleigh-Ritz method.[Langen and Sigbjornsson, 1979]

Dynamic equilibrium equation for a multi-dof system is given by :

$$\mathbf{M}\ddot{\mathbf{r}} + \mathbf{C}\dot{\mathbf{r}} + \mathbf{K}\mathbf{r} = \mathbf{Q}(t) \quad (8.2)$$

For each node i , the displacements are collected in a displacement vector r_i and the total load can be written on matrix form:

$$\mathbf{M}_i\ddot{r}_i + \mathbf{C}_i\dot{r}_i + \mathbf{K}_i r_i = \mathbf{Q}_i(t) \quad (8.3)$$

8.1.2 Mass matrix

The mass matrix is either consistent(banded) or concentrated(diagonal), and includes the effect of inertia forces due to hydrodynamic mass. The consistent mass matrix is based on the same interpolation polynomials as the stiffness matrix. The concentrated mass matrix is based on collecting the mass at the nodes of the structure based on equilibrium considerations. The rotation mass is commonly neglected, which may cause problems for eigenvalue calculations.[Langen and Sigbjornsson, 1979] Remedies for this is static condensation, which is described in chapter 6 in [Langen and Sigbjornsson, 1979].

8.1.3 Damping

The damping term in the equation motion, eq. 8.1, represents the structures ability to dissipate kinetic energy. That is, to transform it into other forms of energy. Damping will always be present for a real vibrating system, and is generally difficult to model correctly. For many applications, simplified models of the damping will give satisfactory results. Such models are e.g. linear and nonlinear viscous damping, structural damping and coulomb damping.[Langen and Sigbjornsson, 1979].

The damping sources can be divided into two main groups, internal damping in the structure and external damping due to interactions between the structure and its surroundings. In addition, for some types of structures like ships for instance, the most important damping source can be friction in the load. The load damping can be a mixture of the three damping models mentioned above.[Langen and Sigbjornsson, 1979]

The internal damping in the structure, also known as structural damping, is related to the internal friction of the material and the connections between the structure elements. Damping related to the connections between the structure elements is often modelled as Coulomb damping. Damping related to the internal friction of the material is characterized by the hysteresis curve of the material, see chapter 9 in [Langen and Sigbjornsson, 1979]. Typical values of the equivalent critical damping ratio is 0.5 – 0.8% for steel structures, and up to 1.2% in concrete structures.[Langen and Sigbjornsson, 1979] The offshore standard OS-C502 app. B A401 states that the damping should be less than 3.0% of the critical damping.[DNV-GL, 2010a]

The damping related to energy loss to the surroundings is typically due to interactions between the structure and a fluid (water/air) or between the structure and its foundation. The first can be divided into hydrodynamic damping, if the fluid is water, and aerodynamic damping, if the fluid is air. Both phenomenon is due to the fact that parts of the fluid pressure are in-phase with the velocity of the structure. Hydrodynamic and aerodynamic damping has two main contributions, one proportional to the velocity and related to the fact that the structural vibrations generates waves propagating away from the structure. This damping is frequently described by a linear viscous model. The second contribution is a non-linear one, related to viscous effects in the water, e.g. vortex shedding. It is often assumed proportional to the square of the relative velocity between the structure and the fluid.[Langen and Sigbjornsson, 1979]

The damping related to interactions between the structure and its foundation has two contributions. The first is geometrical damping, a result of wave energy propagating away from the foundation. This contribution is described by equivalent linear viscous damping model. The second is internal damping in the foundation material. This contribution is described by *hysteresis-loop* obtained by cyclic deformation of the foundation.[Bergan et al., 1981]

Modal damping

Modal damping is defined as damping associated with mode shapes. Structural damping can be described by means of modal damping if we know the logarithmic decrement δ , the loss coefficient η or the damping ratio λ for the mode shapes. These values applies usually only to a few of the lowest modes, and can be found by exciting the structure in resonance. They can be employed directly in the uncoupled dynamic equilibrium equations. For coupled systems, direct solution by frequency-response method demands that the damping is given as a damping matrix \mathbf{C} . [Langen and Sigbjornsson, 1979] Methods for determining \mathbf{C} from modal damping can be found in section 9.5 in [Langen and Sigbjornsson, 1979].

Commonly, for direct integration of the equation of motion, the damping matrix is expressed as a linear combination of \mathbf{M} or \mathbf{K} , or directly from modal damping data. [Langen and Sigbjornsson, 1979]

Rayleigh-damping

Rayleigh-damping, or proportional damping, assumes a distributed damping force proportional to the velocity of mass and to the strain velocity, at each point. Thus, \mathbf{C} is a linear combination of \mathbf{M} and \mathbf{K} [Langen and Sigbjornsson, 1979]:

$$\mathbf{C} = \alpha\mathbf{M} + \beta\mathbf{K} \quad (8.4)$$

\mathbf{C} has the same orthogonality properties as \mathbf{M} and \mathbf{K} , meaning:

$$\phi_i \mathbf{C} \phi_j = \alpha \phi_i^T \mathbf{M} \phi_j + \beta \phi_i^T \mathbf{K} \phi_j = 0 \quad (8.5)$$

for $i \neq j$. Thus, the modal damping coefficients are given by eq.8.6 found in [Langen and Sigbjornsson, 1979, Bergan et al., 1981]:

$$\bar{c}_i = \phi_i^T \mathbf{C} \phi_i = \alpha \bar{m}_i + \beta \bar{k}_i \quad (8.6)$$

The damping ratios are given by eq. 8.7 [Bergan et al., 1981]:

$$\xi_i = \frac{\bar{c}_i}{\bar{c}_{i,cr}} = \frac{1}{2} \left(\alpha \frac{1}{\omega_i} + \beta \omega_i \right) \quad (8.7)$$

with critical damping:

$$\bar{c}_{i,cr} = 2\bar{m}_i \omega_i \quad (8.8)$$

α introduces damping inversely proportional to the angular frequency ω_i , and thus damps out the lower vibration modes. β introduces damping proportional to ω_i and damps out the higher vibration modes.[Bergan et al., 1981]

For desired damping ratios ξ_i and ξ_j for two eigenfrequencies ω_i and ω_j , α and β can be found by substitution to eq. 8.7 [Bergan et al., 1981]:

$$\alpha = \frac{2\omega_i \omega_j (\xi_j \omega_i - \xi_i \omega_j)}{\omega_i^2 - \omega_j^2} \quad (8.9)$$

$$\beta = \frac{2(\xi_i \omega_i - \xi_j \omega_j)}{\omega_i^2 - \omega_j^2} \quad (8.10)$$

8.1.4 Stiffness matrix

The stiffness matrix is assumed linear in this thesis, and equal to that of the static analysis. Thus, nonlinear geometric effects are neglected also for the dynamic response analysis. The structure does not have any water-plane area due to the submergence, and the stiffness is thus provided by axial stiffness and bending stiffness only.

8.2 Wave theory and wave load model used in the dynamic analysis

When investigating the response of a structure due to wave loads, it is interesting to look at the response to the maximum wave height expected at the site. This section gives a brief description of how to estimate the maximum wave height, how to calculate first order wave loads in Sesam and the wave model used in this thesis. Recall section 4.2.5 in the load theory chapter.

8.2.1 Stochastic wave theory

In design of offshore structures it is important to investigate the worst possible sea state to ensure that the structure can survive it. For this purpose the sea state with return period of 100 years is often used. It is assumed that the significant wave height, corresponding to average of the $\frac{1}{3}$ highest waves, is constant within a sea state. The 100 year value of H_s is defined as the value that on average occurs only once during 100 years. The parameters corresponding to this sea state can then be used in a standardized wave spectrum.[Myrhaug, 2007]

When the worst sea state is found we seek the individual wave height H , in that sea state, which is exceeded once during m years, here 100 years. Before this can be found, we need to look at the behaviour of the individual wave heights.

Short term statistics

The short term distribution of wave heights for a given sea state is defined as the probability distribution of the wave heights in that sea state. It is mathematically difficult to find the probability distribution of wave heights of a given wave record. A simplified probability distribution can be obtained by assuming that the wave elevation is stationary, narrow-banded and a Gaussian distributed stochastic process. The assumption of a stationary wave elevation means that the average wave height and variance are constant within the duration of the wave process.[Myrhaug, 2007] Narrow-banded process means that there are only positive maxima and there are only one maxima per positive zero-crossing.[Myrhaug, 2005] The name narrow-banded process comes from the fact that its spectral density occupies a narrow band of frequencies.[Newland, 1993] See the realization of a general and a narrow-banded stochastic process below.

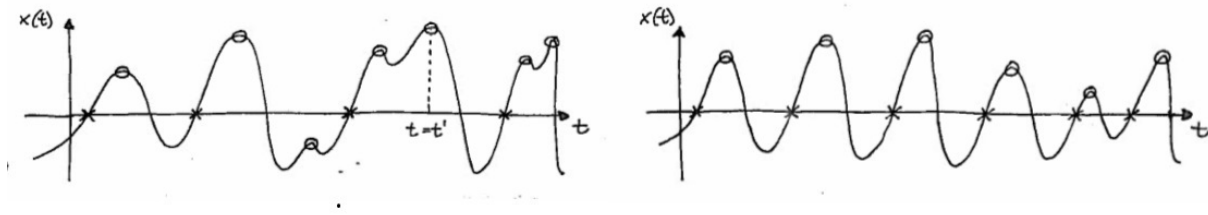


Figure 8.1: To the left: an example of a realization of a general stochastic process. To the right: an example of a realization of a narrow-banded stochastic process. Illustration: [Myrhaug, 2007]

The wave elevation was also assumed Gaussian distributed. It is further assumed that the wave elevation has zero mean value, corresponding to the mean free surface, and a variance σ^2 . [Myrhaug, 2007] The Gaussian distribution, also called normal distribution, is a common probabilistic model in which the variable under consideration is of additive type, i.e. expressed as a sum. This is a result from the central limit theorem, which states: "If the number of variables in a sum approaches a large number, the distribution of the sum will approach the normal distribution under very general conditions". [Leira, 2010] For this to be fulfilled, the most common requirement is that the variables must be independent and identically distributed. See page 5.12 in [Leira, 2010] for other categories of requirements for the central limit theorem.

For an idealized wave process which is stationary, narrow-banded and Gaussian distributed, the individual maximal values of the wave elevation can be approximately described by the Rayleigh distribution. [Myrhaug, 2007]

In [Myrhaug, 2007] it is shown that if the wave maximas are Rayleigh distributed, then the significant wave height can be estimated as $H_s = H_{m0} = 4\sqrt{m_0}$. Rearranging this gives m_0 :

$$m_0 = \frac{H_{m0}^2}{16} \quad (8.11)$$

Thus, the Rayleigh distribution of the maximas can be written [Myrhaug, 2007]:

$$f_H(h) = \frac{4h}{H_{m0}^2} \exp\left(-2\left(\frac{h}{H_{m0}}\right)^2\right) \quad (8.12)$$

$$F_H(h) = 1 - \exp\left(-2\left(\frac{h}{H_{m0}}\right)^2\right) \quad (8.13)$$

Extreme value distribution

The theory in this section is gathered from [Myrhaug, 2007, Myrhaug, 2005]. The aim of extreme value statistics is to estimate the expected largest or smallest among N outcomes in a given time interval. With a given sample of maximas $(H_1 \dots H_N)$,

which is assumed identically Rayleigh distributed ($F_H(h)$) and statistically independent, the distribution of the largest maxima, here called H_{max} , can be derived as follows [Myrhaug, 2007]:

$$\begin{aligned} F_{H_{max}}(h) &= P[H_{max} \leq h] = P[(H_1 \leq h) \cap \dots \cap (H_N \leq h)] \\ &= P(H_1 \leq h) \cdot P(H_2 \leq h) \cdot \dots \cdot P(H_N \leq h) \\ &= [P(H_i \leq h)]^N = [F_H(h)]^N \end{aligned} \quad (8.14)$$

From the distribution of the largest maxima, the expected largest can be estimated in three different ways. The derivation of the three values can be found in [Myrhaug, 2005]:

The expected largest wave height, for large N:

$$E[H_{max}] = \int_0^{\infty} h \cdot f_{H_{max}}(h) dh \approx H_{m0} \left\{ \sqrt{\frac{\ln N}{2}} + \frac{0.2886}{\sqrt{2 \ln N}} \right\} \quad (8.15)$$

The most probable largest wave height H_M , also known as the characteristic wave height:

$$\left[\frac{d}{dh} f_{H_{max}}(h) \right]_{h=H_M} = 0 \quad (8.16)$$

which for large N can be approximated by:

$$H_M = H_{m0} \sqrt{\frac{\ln N}{2}} \quad (8.17)$$

The definition of the characteristic wave height is the value, out of N values, that is only exceeded by one value. Thus, H_M can also be estimated by:

$$(1 - F_H(H_M)) = \frac{1}{N} \quad (8.18)$$

Thus, for all methods, the uncertainty is dominated by the number of maxima in the given sea state. If the duration D of the sea state and zero crossing period T_z is known, then the number of wave heights in the sea state is:

$$N = \frac{D}{T_z} \quad (8.19)$$

8.2.2 Design swell model

The swell waves are in this thesis modeled as regular waves, with a constant wave height equal to the estimated maximal wave height. The response is assumed linear, meaning that harmonic loads results in harmonic responses. It is also assumed that

the maximal response occurs at the maximal wave height. The wave period and wave direction is varied. The sea states investigated in this thesis are given in table 8.1.

Table 8.1: Overview of the sea states investigated in this thesis.

Sea state	T(s)	H_{max} (m)	β^0 (deg)
1	8.9	0.19	110°
2	14	0.19	110°
3	8.9	0.19	140°
4	14	0.19	140°

8.2.3 Wajac

As earlier stated, Wajac is a program in the Sesam system that calculates wave and current loads on fixed and rigid frame structures. It is limited to structures with structural members of relatively small cross-section compared to the wave lengths. Morison's equation is used for calculation of wave loads. The loads calculated by Wajac can be transferred for structural analysis by Sestra.[DNV-GL software, 2017]

There are three different approaches for load calculations in Wajac, deterministic load calculation in the time domain, calculation of force transfer function in the frequency domain and time domain simulations of wave loads for given short-term seastates. The first is the one used in this thesis. In the deterministic load calculation, the structure is subjected to an unidirectional periodic wave. The loads are calculated at given time instants. Different wave models are available, and the one used in this thesis is the Airy wave theory.[DNV-GL software, 2017]

Description of environment in Wajac

The periodic surface waves are described by a wave period T , wave height H , wave propagation angle β^0 , measured counter-clockwise from the global positive x -axis to the propagation direction of the waves, and the mathematical model of the waves. This makes up the specified sea condition, or in Wajac called sea state.

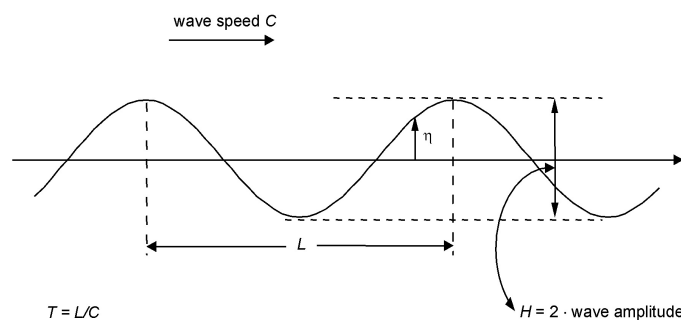


Figure 8.2: Description of surface waves. Illustration:[DNV-GL software, 2017]

Load calculation in Wajac

As earlier mentioned, the Morison's equation with non-linear drag formulation is used to calculate the hydrodynamic forces (eq. 8.20). Recall section 4.2.5 in the load theory chapter.

$$F_n(r, t) = \rho \frac{\pi D^2}{4} C_m a_n(r, t) + \frac{1}{2} \rho D C_d v_n(r, t) |v_n(r, t)| \quad (8.20)$$

where ρ is the density of water, D is the equivalent diameter of the structure, C_m is the inertia coefficient matrix, C_d is the drag coefficient matrix, $v_n(r, t)$ is the undisturbed velocity component of the fluid particles normal to the member at the time and point instant, $a_n(r, t)$ is the undisturbed acceleration component of the fluid normal to the member and r is the global coordinate of the point of load calculation.

The transverse components are given as linearly varying line loads. For each time step, the loads are calculated for each specified sea state. The distributed loads are saved for subsequent structural analysis in Sestra. In addition, another result file, called the S-file, is produced by Wajac. This file needs to be manually modified for dynamic analysis in Sestra, see [DNV GL, 2018].

Wajac calculates the wave loads as if the structure was a circular cylinder. The equivalent diameters are thus calculated by setting the area of a rectangular cross-section equal to the area of a circular cylinder and solve for the diameter (eq.8.21).

$$D = \sqrt{4bh/\pi} \quad (8.21)$$

Limitations of Wajac

- Assumes that the structure is fixed in space.
- Assumes that there are no diffraction effects, meaning that the structure does not have any influence on the fluid.
- Hydrodynamic coefficients are assumed frequency independent.
- The structure is modeled as a circular cylinder for the wave load calculation, with an equivalent diameter.

8.3 Solution methods of the dynamic equilibrium equation

The dynamic equation, eq. 8.2, can be solved either in the time-domain, ie. assuming a deterministic system, or in the frequency domain. The latter is commonly used for response due to stochastic loads. Time-varying loads like wave loads are often random and can be described by assumed probabilistic models. However, the response

of a stochastic load will be stochastic, and therefore, it is only possible to give statements about the response magnitude, or the probability that it will not exceed a certain value.[Langen and Sigbjornsson, 1979]

Direct solution method, in either time or frequency domain, is meant as the solution for the coupled equation system. The alternative is to transform the coupled equation system into an uncoupled system and then solve separately.[Langen and Sigbjornsson, 1979]

Solution obtained in the frequency domain

An arbitrary time-varying loading can be described by a sum of harmonic contributions. Mathematically, this is expressed by the Fourier-transformation. Each single harmonic component is a function of the frequency ω . Thus, the sum represents excitation in the frequency domain. Similarly, the response can be transformed to the time domain. Thus, solving the dynamic equilibrium equation in the frequency domain means solving eq. 8.2 for harmonic loading for different frequencies. By this, the solution directly shows the sensitivity of a structure to load frequency. [Langen and Sigbjornsson, 1979]

Modal analysis and modal superposition

In dynamic analysis it is common to express the displacements in terms of the mode shapes, which were described and found in sec. 7. Because the n eigenvectors ϕ_i are linearly independent, a linear combination of these can be used to express an arbitrary displacement r of a structure (eq. 8.22).[Langen and Sigbjornsson, 1979] See figure 8.3 for an illustration of the method.

$$r = \sum_{i=1}^n \phi_i y_i(t) = \phi y \quad (8.22)$$

The matrix ϕ represents the matrix of vibration modes and contains the mode shapes $\phi = [\phi_1 \phi_2 \dots \phi_n]$ and y is the vector of displacement amplitudes designated normal coordinates:

$$y = \begin{bmatrix} y_1 \\ y_2 \\ \vdots \\ y_m \end{bmatrix} \quad (8.23)$$

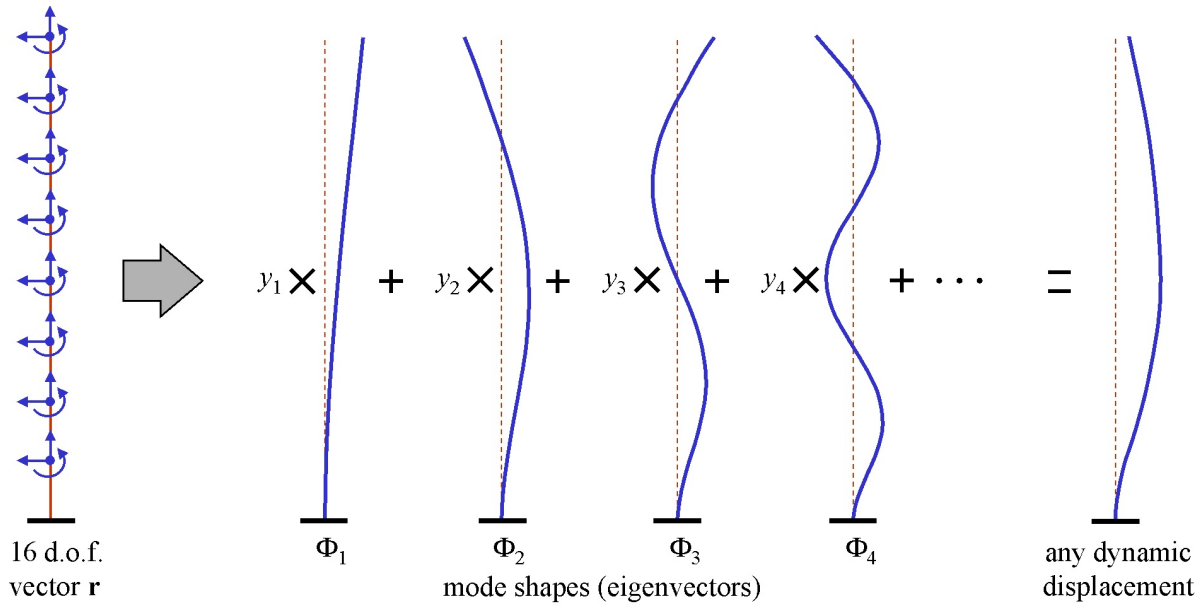


Figure 8.3: Illustration of the concept of modal superposition. [DNV-GL software, 2014]

Solution obtained in the time domain

The response to an arbitrary load history can be obtained by expressing the load history as a series of short impulses, and then superimpose the responses to get the total response. A method for finding the response of a multi-degree of freedom system is direct numerical integration of the dynamic equilibrium equation. The dynamic response is thus found as values at discrete time instants rather than a continuous function. However, the accuracy of the numerical solution is limited by the calculation method used and the step size for time-integration.[Larsen, 2014]

One method described in [Larsen, 2014], for finding the response by numerical integration, is the Newmarks β -method. The general integration equations in this method are given in eq.8.24-8.26. By using these equations together with the equation of motion (eq.8.27), the resulting displacement, velocity and acceleration can be found. γ is a parameter controlling the numerical damping, and is often set to $\gamma = \frac{1}{2}$, which represents no numerical damping.[Larsen, 2014] The parameter β is different for the different Newmark-family methods, see [Larsen, 2014].

$$u_{i+1} = u_i + h\dot{u}_i + \left(\frac{1}{2} - \beta\right)h^2\ddot{u}_i + \beta h^2\ddot{u}_{i+1} \quad (8.24)$$

$$\dot{u}_{i+1} = \dot{u}_i + (1 - \gamma)h\ddot{u}_i + \gamma h\ddot{u}_{i+1} \quad (8.25)$$

$$\ddot{u}_{i+1} = \frac{1}{\beta h^2}u_{i+1} - \left(\frac{1}{2\beta} - 1\right)\ddot{u}_i - \frac{1}{\beta h}\dot{u}_i - \frac{1}{\beta h^2}u_i \quad (8.26)$$

$$\begin{aligned}
\left[\frac{1}{\beta h^2}m + \frac{\gamma}{\beta h}c + k\right]u_{i+1} &= P_{i+1} + \left[m\left(\frac{1}{2\beta} - 1\right) + h\left(\frac{\gamma}{2\beta} - 1\right)c\right]\ddot{u}_i \\
&+ \left[\frac{1}{\beta h}m + \left(\frac{\gamma}{\beta} - 1\right)c\right]\dot{u}_i + \left[\frac{1}{\beta h^2}m + \frac{\gamma}{\beta h}c\right]u_i
\end{aligned}
\tag{8.27}$$

Sestra takes advantage of a generalization of the Newmarks method for discretising the equation of motion in time. See Sestra User manual [DNV GL, 2018] for more information about the different generalization methods available in Sestra. In this thesis, Newmark method with $\beta = \frac{1}{4}$ and $\gamma = \frac{1}{2}$ is used to ensure a conditionally stable solution. Thus, constant average acceleration is assumed. This is according to [Larsen, 2014] one of the most applied methods for time integration.

8.4 Results of dynamic analysis

8.4.1 Estimation of Rayleigh-damping coefficients

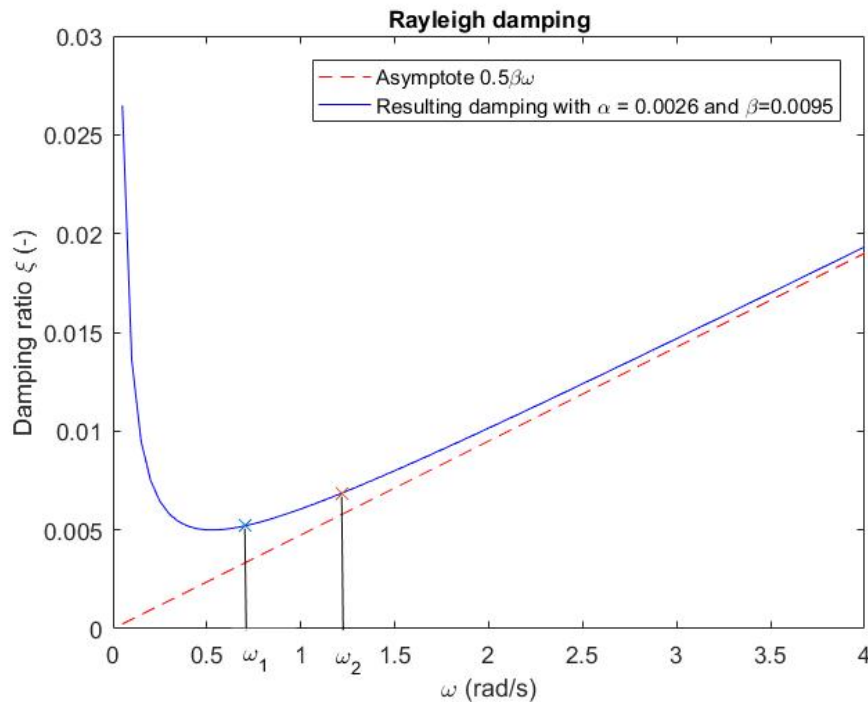


Figure 8.4: Damping ratio versus angular frequency. $\xi_i = 0.5\%$ and $\xi_j = 0.8\%$.

Table 8.2: Rayleigh-damping coefficients for different damping ratios.

Damping Ratios		Rayleigh coefficients	
ξ_i	ξ_j	α	β
0.5%	0.8%	0.0026	0.0095
0.8%	1.5%	0.0034	0.0185
1.5%	3.0%	0.0056	0.0375

8.4.2 Estimation of maximum wave height

Table 8.3: Estimation of maximum wave height for the given 100 year sea state.

Parameter	Result (m)
$E[H_{max}]$	0.1902
H_M	0.1823

8.4.3 Response due to swell sea

Note that the results are given for the direction and wave period giving the maximal results for the respective variable.

Maximal displacements and accelerations

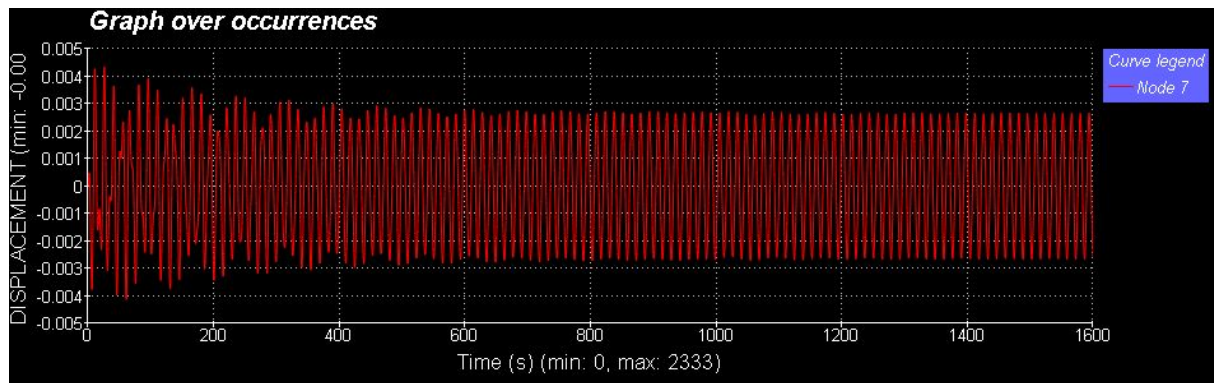


Figure 8.5: Time record of vertical displacement amplitudes due to regular swell wave $T_p = 14s$, $\beta^0 = 110^\circ$.

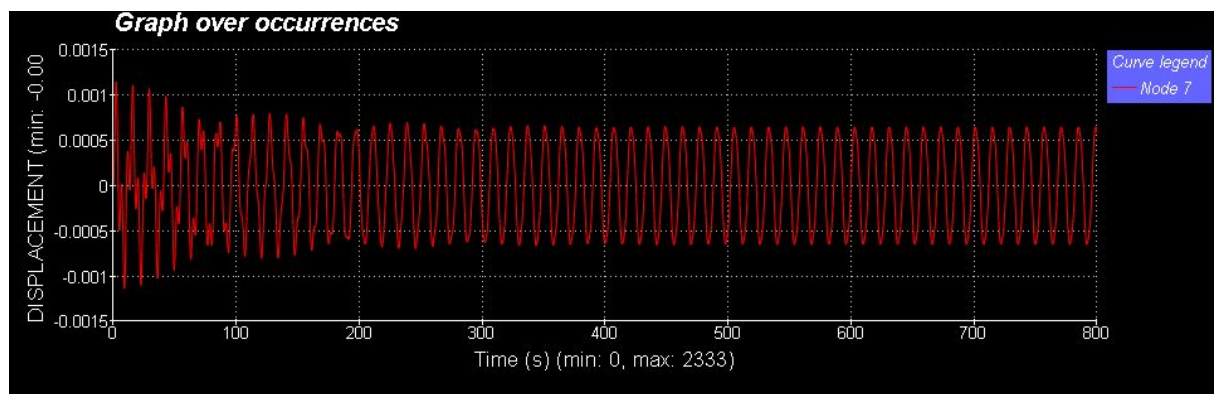


Figure 8.6: Time record of transverse displacement amplitudes due to regular swell wave $T_p = 14s$, $\beta^0 = 110^\circ$.

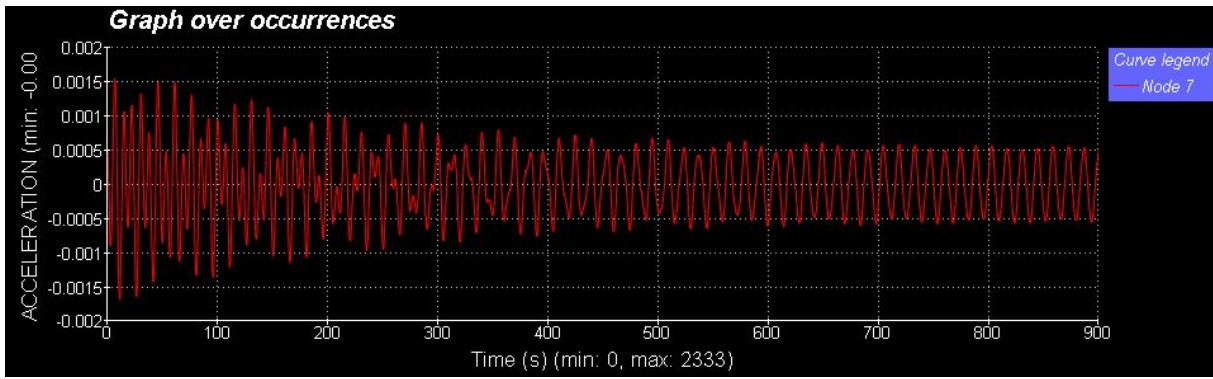


Figure 8.7: Time record of vertical acceleration amplitudes due to regular swell wave $T_p = 14s, \beta^0 = 110^\circ$.

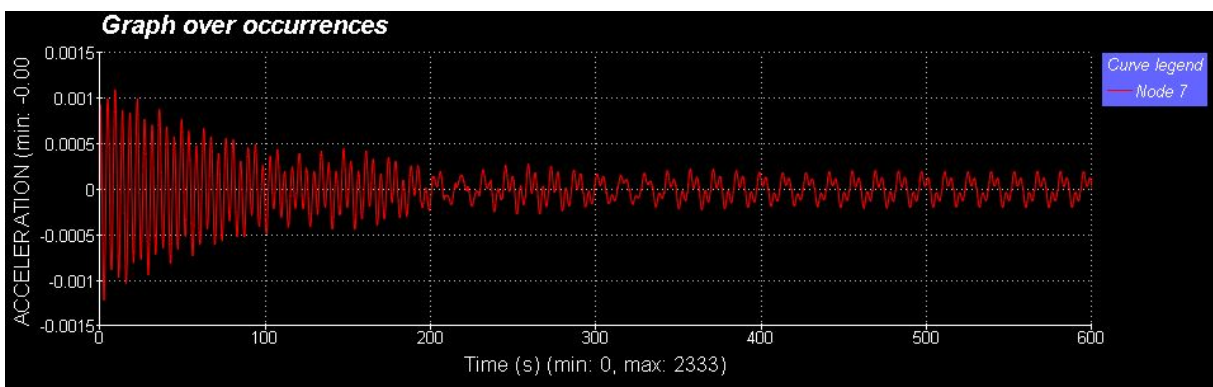
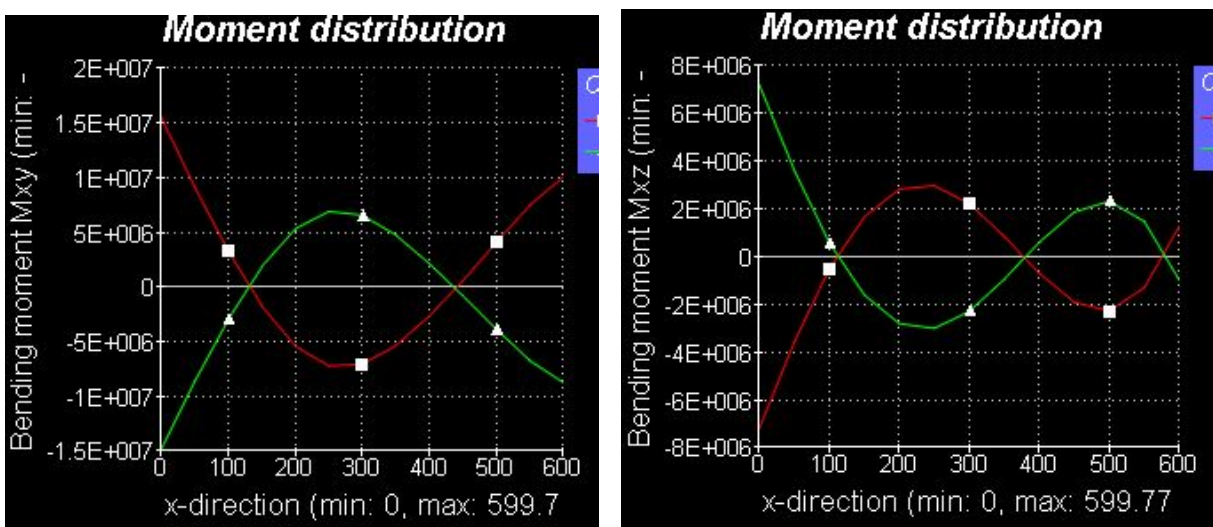


Figure 8.8: Time record of transverse acceleration amplitudes due to regular swell wave $T_p = 14s, \beta^0 = 110^\circ$.

Envelopes of maximal bending moments



(a) M_{xy} , bending moment about z-axis.

(b) M_{xz} , bending moment about y-axis.

Figure 8.9: Envelopes of maximal bending moments due to regular swell sea with $T_p = 14s, \beta^0 = 110^\circ$.

8.5 Discussion of results from dynamic analysis

Discussion of damping model and added mass coefficient

The viscous damping is considered small due to low ability to generate waves at the water depth of the SFT.[Xiang et al., 2017] It is assumed that there exists some structural damping in the concrete, which is modeled as Rayleigh damping. The Rayleigh coefficients were found for three different damping ratios in tab.8.2. The lowest coefficients, meaning the coefficients corresponding to damping ratios of 0.5 – 0.8% were used in further analysis. From the table, it is evident that the damping is dominated by damping proportional to the stiffness. There is a small contribution in damping proportional to the inertia. When increasing the damping ratios, the graph over damping versus frequency (fig.8.4) gets steeper, see app.G.3. Higher damping ratios results in higher Rayleigh damping coefficients. The desired region, for the structure eigenfrequency to be, is in the lower part of the blue graph. For all damping ratios, both the first and second eigenfrequency lay in the desired region.

Added mass and damping coefficients were assumed independent of direction, frequency and Reynolds number. In reality, this is not the case. The frequency dependence of the coefficients should be investigated.

Discussion of maximum wave height estimation

The maximal wave height estimation was based on stochastic theory. The estimated maximal wave height was found as the expected largest, with a magnitude of 0.1902 m (tab.8.3). Thus, the expected maximal was larger than the most probable largest maximal as expected. The expected value and the characteristic value was based on the assumption of N , meaning the number of wave heights, being large. That assumption is dependent on the sample of wave heights. The number of wave heights was calculated based on the duration of the sea state and the zero-crossing period, which was assumed equal to the peak period for simplicity. To ensure that the maximal wave heights are captured, the sample must be large enough. According to [Engseth et al., 2016], hindcast data didn't give good results for the site, and the wave heights were estimated based on SWAN analysis. An alternative could be measurements at site. However, this will be time consuming as the sample need to be large enough to be able to capture the maximal response. It is therefore important to note that the maximal wave height estimate is an rough estimate.

Discussion of the use of Wajac for wave load calculation

By investigating the exponential decay of wave action, it was found that swell sea is dominating at the depth of the SFT (fig.4.2). A peak period of 14s corresponded to a wave length which was roughly 18 times the largest equivalent diameter of the SFT. It was therefore assumed that the structure was small compared to the swell waves, and thereby that Morison's equation was applicable. Wave load calculation in Wajac is based on the assumption of no diffraction effects [DNV-GL software, 2017]. This is unphysical, because the presence of the structure will affect the water.[Faltinsen, 1990]

However, because the response of the structure is found to be small at the depth of the SFT, it can be argued if the diffraction effects can be neglected.

Note that the wave load calculation in Wajac is carried out as if the structure was a circular cylinder, which simplifies the wave load calculations. The cross-sections were modeled as circular cylinders with equivalent diameters D . According to [Faltinsen, 1990], Morison equation calculates the wave loads in the direction of the incoming wave. However, the equivalent diameters were assumed constant for the two wave headings investigated in this thesis. For more realistic results, the equivalent diameters should be representative for the wave heading of interest. In addition, the same equivalent diameters are used for both terms in the Morisons equation. The first term, representing the inertia term, should be based on the correct area for a rectangular cross-section, while the latter term, representing the drag term, should be based on the height of the rectangular. Due to the many limitations of Wajac, other software like SIMA/Riflex or ANSYS should be used to obtain a better and more realistic representation of the wave loads acting on the structure. The results from Wajac should only be used as an rough estimate.

Discussion of the design swell model

The swell sea is modeled as regular waves. In reality, waves in general are irregular by nature. The results based on regular waves is therefore a rough estimate of the maximal response. Sending a regular wave through the structure, with a constant wave height equal the estimated maximal wave height, is conservative. According to [Myrhaug, 2005], the characteristic largest wave height, H_M , corresponds to the value which is only exceeded once among a sample of N wave heights. It is unlikely that the largest wave height will occur multiple times in a row. A better model of the design swell wave can for instance be based on New-wave theory.

The assumption of linear response can also be questioned. In this thesis, it is assumed that the maximal response occurs at the maximal wave height. This is not necessarily true. Using Morison's equation will introduce non-linear effects on the response due to the non-linear drag-term. To have a clear picture of the occurrence of maximal response, a full analysis with actual wave data or a simulation of the wave elevation should be done. This thesis gives approximated results of the response only.

Discussion of the response due to swell waves

It was chosen to investigate the response from four different sea states with the objective to estimate the maximal dynamic response which can be expected at site (tab.8.2.3). Two sea states with peak period 8.9s were investigated, with different respective directions. The peak period of 8.9s was chosen with the objective to investigate possible resonance, as it is close to the first eigenfrequency of the base case without influence of the compression force from the PT-cables.

The sea state with $T_p = 14s$ and direction $\beta = 110^\circ$ gave the highest displacements and accelerations in z-direction. The time record of the vertical displacement amplitudes are shown in fig.8.5. It is seen from the time record that the response in this case builds

up towards an amplitude of 2.67 mm when t is large. The response seem to converge to a harmonic response after 900s. Compared to the vertical displacement due to static loads, which was found to be 0.52 m (tab.6.8), the vertical displacement due to wave loads is considered negligible. The time record for the vertical acceleration is shown in fig.8.7. As for the vertical displacement, the time record shows that the response builds up towards an harmonic response. The amplitude of the harmonic response for the acceleration is about $0.0005m/s^2$. Compared to the limit for maximal vertical acceleration, which was set to $0.5m/s^2$, the vertical vibrations due to waves are also negligible.

The highest displacements and accelerations in y -direction due to swell waves were found for the sea state with $T_p = 14s$ and wave direction 110° . The time record of the transverse displacement amplitudes is shown in fig.8.6. After 400s, the response seem to stabilize and converge to a harmonic response with an amplitude of about 0.6 mm. Recall that the transverse displacement due to static loads was 13.51 mm (tab.6.8). Thus, the transverse displacements due to swell waves are considered negligible compared to the static response. The time record of the transverse acceleration is given in figure 8.8. The numerical solution does not converge towards a regular response, but the solution stabilizes after 350s with an maximal amplitude of $0.0002 m/s^2$. Recall that the limit for maximal horizontal vibration was set to $0.3m/s^2$ [Engseth et al., 2016]. The horizontal vibrations due to the swell waves are also considered negligible compared to the limitation.

Recall the equations for linear waves in deep water in sec.4.2.5. By investigating the exponential decay for wave action it is found that a wave period of 8.9s results in wave action, at the depth of the SFT, which is only 7.9% of the wave action at the free surface. For a wave period of 14s, the wave action at the depth of the SFT is 35.8% of the wave action at the free surface. It is therefore expected that the sea states with a wave period of 14s give the highest wave loads. This is also what is observed by looking at the envelopes of bending moments for all the sea states considered. The maximal bending moments were found for the sea state with $T_p = 14s$ and wave direction 110° . The envelope for maximal bending moment about y -axis due to swell waves is shown in fig.8.9a. The highest bending moments are located at the bridge ends, with a magnitude of 15 MNm, which is approximately 5.7% of the maximal bending moment due to the static loads in SLS. The envelope for maximal bending moment about z -axis due to swell waves is shown in fig.8.9b. The highest bending moments are located at the bridge end to the left, with a magnitude of 7 MNm. This is approximately 6.4% of the bending moment at the bridge ends due to the static current loads in SLS. Because the bending moments due to swell sea were found approximately 6% of the bending moment from net static loads, it can be debated if they can be neglected. To ensure conservatism, they should be included in both the check of max allowable stresses and moment capacity.

Further discussion the equivalent diameter

The first dynamic response analyses were carried out with an equivalent diameter equal to the diagonal of the rectangular. This was the definition of the equivalent diameter for a rectangular in the Wajac user manual, [DNV-GL software, 2017]. However, it

is assumed that a circular cylinder with diameter equal to the diagonal of the rectangular will overestimate the dimensions of the tube for beam sea. Based on recommendations from the supervisor, Bernt J. Leira, the equivalent diameters were reconsidered. Recall from section 4.2.5 (gathered from [Faltinsen, 1990]) that the inertia term in the Morison equation decays with $e^{\frac{2\pi z}{\lambda}}$ and the drag term decays with a factor of $e^{\frac{4\pi z}{\lambda}}$. Due to the high submergence of the SFT, the inertia term is the dominating force in the Morison equation. The equivalent diameters for wave headings $\beta_0 = 110^\circ - 140^\circ$ were therefore estimated based on setting the area of the circumferenced rectangle equal to the area of a circular cylinder (eq.8.21, sec.8.2.3).

The results for the maximal dynamic response, from the first runs of dynamic analysis, are given in app.G.3. These runs were based on an equivalent diameter equal to the diagonal of the rectangular. These equivalent diameters are approximately 30.7% higher than the diameters for the base case. Investigating the terms in Morison's equation (eq.8.20), it is found that the diameter increase should result in approximately 70.8% higher inertia term, and 30.7% higher drag term, than for the base case.

The time records of the vertical displacement and acceleration are given in fig.G.10 and G.12. Contrary to the base case, the maximal response with respect to the vertical displacement and acceleration were found for the sea state with $T_p = 8.9s$ and $\beta_0 = 110^\circ$. For the case of increased equivalent diameter, both the results for vertical displacement and acceleration start to oscillate, and the oscillation amplitude increases linearly towards the harmonic solution obtained after 650s. For the base case, the start-up of the response, for the vertical displacement and acceleration, is unstable and unexpected. In addition, the numerical solution for the base case stabilizes after longer time than for the case of increased equivalent diameter. The harmonic response amplitude of the maximal vertical displacement is approximately 87% higher than that of the base case. The time record of the transverse displacement for the case of increased equivalent diameter is given in fig.G.11. The start-up of the response is unstable for both diameter cases. For the base case, the numerical solution for the transverse displacement seem to stabilize after approximately 400s, whereas the numerical solution for the increased equivalent diameter seem to stabilize after approximately 350s. Thus, it is concluded that the numerical solution in Sestra is dependent on the size of the structure. Higher equivalent diameters give faster stabilization of the solution. The harmonic response amplitude for the maximal transverse displacement for the case of increased equivalent diameter is approximately 57% higher than the result from the base case. The response of the transverse acceleration for both diameter cases is unstable, and do not seem to converge to harmonic response.

The envelopes of maximal bending moments for the case of increased equivalent diameter are given in figure G.14. The maximal bending moment about y-axis is 2 times the result of the base case (fig.8.9a). The maximal bending moment about the z-axis is 1.57 times for that of the base case (fig.8.9b).

Chapter 9

Concluding remarks

With a specific weight of reinforced concrete of $25\text{kN}/\text{m}^3$, the buoyancy is the dominating load in the vertical direction. This results in high reaction forces to be transferred to the abutments and high bending moments. The stress calculations showed that the maximal total compressive stresses were below $0.6f_{ck}$. The tensile stresses from the characteristic loads exceed the tensile strength of concrete and the cross-section should be considered cracked. One of the requirements in SLS was that the cross-section should remain uncracked to avoid leakage. Thus, the weight should be increased to balance the buoyancy. A full calculation of the amount of reinforcements should be carried out and its contribution included in the weight calculations. In addition, it is possible to increase the ballast chamber fill percentage to increase the weight.

The transverse reactions are dependent on the current direction and profile. Uniform distributed current loads applied to the full length of the bridge in either positive or negative y -direction resulted in tension and compression forces in the bridge respectively. These cases were found to give the highest bending moments and axial forces in the structure compared to the two other current load cases. When calculating the maximal total stresses in the concrete at critical sections with respect to tension or compression, it was found that the contributions in stress from axial forces and bending moments due to current loads are small compared to the contributions from PT-cables and the net vertical forces.

Increasing curve height influences the static response, the eigenfrequencies and the mode shapes. When a curve height is introduced, axial forces are present due to transverse loading. As the curve height is further increased, the axial forces and bending moments due to transverse loading decrease. However, the torsional moments increase with increasing curve height. This is due to the centre of gravity translating as the curve height increases. For the eigenvalue analysis, the eigenfrequency of the first horizontal mode is of interest when introducing a curve height. For the straight bridge model, the eigenfrequency of the first horizontal mode is 0.120 Hz. Introducing a curve height of 24.25m, which is the base case, the eigenfrequency of the first horizontal mode is 0.189 Hz. Increasing the curve height further results in further increased eigenfrequency of the first horizontal mode. The curve height where the first and second mode shape changes order was found 49m analytically, 53m in Sestra and 56m in Abaqus.

The influence of reinforcements and post-tension cables were accounted for in the bending stiffness of the structure, in the stress calculations and in the eigenvalue analysis. The average increase of moment of inertia, when accounting for reinforcements and PT-cables in transformed concrete cross-sections, are 3.89% for I_z and 3.24% for I_y . The axial compression from the PT-cables on the concrete was calculated 428 MN, corresponding to 5.75% of the Euler buckling load. This gave an amplification factor of 1.063 to multiply with the bending moments in the stress calculations. In the eigenvalue analysis, the PT-cables were accounted for by reducing the eigenfrequencies. The reduction for the first mode was -2.83%. For higher mode number, the reductions were calculated less than one percent and are thus neglected.

The eigenvalue analysis in Sestra and Abaqus gave different results for the base case. For the first five modes, the deviations are below five percent. For increasing mode number, the deviations increase. Sestra gave the lowest eigenfrequencies, and are thus assumed to give the most conservative results compared to Abaqus. The eigenperiods calculated by Sestra and Abaqus deviates from the calculations by the NPRA by about 10-20%. It is assumed that this deviations is a result of differences in modeling and assumptions for the eigenvalue analysis. Accounting for the reduction factor due to compression force from PT-cables, the first eigenperiod for the base case was calculated 9.14s. The second, corresponding to a horizontal mode with one half-wave, was calculated 5.16s by Sestra. The third and fourth, corresponding to vertical and horizontal mode with two half-waves respectively, were calculated 3.34s and 3.00s by Sestra. For increasing mode number, the eigenfrequencies are close.

The second, third and fourth eigenfrequency are close to, or in the range of, the peak periods for wind generated sea at site. However, these sea state are assumed to exhibit low energy levels, especially at the depth of the SFT. Swell sea was found to be the dominating wave type at the depth of the SFT. However, the dynamic response from first order swell waves was found to be of second importance compared to the response from static loads. Displacements due to the swell waves investigated in this thesis were found negligible compared to the results from static analysis. The submergence of the tunnel provides shelter from the wave loads as the wave action at the depth of the SFT is 35.8% of the wave action at the free surface. The bending moments due to swell waves were calculated roughly 6% of the bending moment from net static loads. To ensure conservatism in stress calculations, the bending moments from wave loads should be included.

Chapter 10

Recommendations for further work

Topics that can be investigated are listed below.

- Calculate the weight for correct amount of reinforcements and post-tension cables, and include weight of emergency exits.
- Check moment and shear capacity in ultimate limit state.
- Create a general input file for GeniE to effectively edit the dimensions of the model and generation of new nodal points.
- Model the bridge with both vertical and horizontal alignment.
- Dynamic response analysis due to irregular waves.
- Dynamic response analysis for the towing and installation phase.
- Convergence studies of the static results when increasing the curve height.
- Dynamic response analysis in the frequency domain.
- Investigate other wave models, like Stokes 5th or new wave theory.
- Assessment of necessary post-tension cables and reinforcements.
- Parameter studies with variation with respect to geometry, ballast, supporting system etc.
- Compare with a model with tethers at the mid-span, modeled as a spring-support.
- Investigate damaged configuration, i.e. cracks.
- Optimize amount of permanent ballast.
- Investigate the hydrodynamic coefficients
- Model the bridge with other element, e.g. shell elements.
- Investigate the response to non-linear wave loads.
- Accidental limit state analysis.
- VIV analysis.

Bibliography

- [A. R. Reinertsen, 1988] A. R. Reinertsen (1988). Analysegrunnlag fytebroer. Håndskrevne notater. Kapittel 3 - Analytisk dynamisk løsning.
- [Amdahl, 2013] Amdahl, J. (2013). TMR4205 Buckling and Ultimate Strength of Marine Structures. Chapter 2: Buckling of bars and frames.
- [Bergan et al., 1981] Bergan, P. G., Mollestad, E., and Larsen, P. K. (1981). Svingning av konstruksjoner. Tapir, Trondheim.
- [Bernhardt, 1975] Bernhardt, C. J. (1975). Spennbetong del 1 - del 2 Forelesninger. Institutt for betongkonstruksjoner, NTH, Trondheim.
- [Broer.no, 2017] Broer.no (2017). Helgelandsbrua. Available at <http://broer.no/bro/index.php?ID=39>. Accessed 20.09.2017.
- [broer.no, 2018] broer.no (2018). Hardangerbrua. Broer.no. <http://broer.no/bro/index.php?ID=106>.
- [Clough and Penzien, 2003] Clough, R. W. and Penzien, J. (2003). Dynamics of structures. Computers & Structures, Inc., USA, 3 edition.
- [DNV-GL, 2010a] DNV-GL (2010a). Dnv-os – c502 offshore concrete structures.
- [DNV-GL, 2010b] DNV-GL (2010b). Environmental conditions and environmental loads. recommended practice. DNV-RP-C205.
- [DNV GL, 2018] DNV GL (2018). SESAM UM - SESTRA Finite element analysis solver, version 10.3.1. Sesam User Manual.
- [DNV-GL software, 2014] DNV-GL software (2014). SESTRA Superelement Structural Analysis version 8.6. DNV GL, 13 edition. Sesam User Manual.
- [DNV-GL software, 2016] DNV-GL software (2016). SESAM UM Genie - vol2 Wave and structure-pile-soil analysis. DNV-GL. Sesam User Manual.
- [DNV-GL software, 2017] DNV-GL software (2017). SESAM UM Wajac - Wave and current loads on fixed rigid frame structures. Version 7.1. Sesam User Manual.
- [DNV-GLsoftware, 2015] DNV-GLsoftware (2015). SESAM UM GeniE Tutorial - Modelling an arched steel-building frame. DNV-GL. Sesam User Manual.
- [Engseth et al., 2016] Engseth, M., Maurset, H., Gallala, J., and Rasmussen, S. (2016). E39 digernessundet sftb technical report. Technical report, Dr. techn. Olav Olsen AS.

- [Faltinsen, 1990] Faltinsen, O. M. (1990). Sea loads on ship and offshore structures. Cambridge University Press.
- [Irgens, 2006] Irgens, F. (2006). Fasthetslære. Tapir Akademisk Forlag, Trondheim, 7 edition.
- [Johansen, 2017] Johansen, H. (2017). Calculation guidelines for pt concrete bridges. NPRA reports 668, NPRA.
- [KAA, 2016] KAA (2016). Bjørnafjorden suspension bridge - k1 & k2 design summary. Technical report, Statens Vegvesen, Aas-Jakobsen, TDA, COWI, Johs. Holt, Moss-maritime, NGI, Plan. Available at https://www.vegvesen.no/_attachment/1607159/binary/1145772?fast_title=Bj%C3%B8rnafjorden+Supension+Bridge+%28TLP%29+K1+%26K2+Design+Summary.pdf. Accessed 25.09.2017.
- [Kystverket, 2014] Kystverket (2014). Farledsnormalen. Instruks for Kystverkets planlegging, prosjektering og vurdering av arealbehov for farleder. Available at <http://www.kystverket.no/contentassets/3793b93c665a4816a26c698c37c295a4/farledsnormalen-v01.pdf>. Accessed 02.06.18.
- [Langen and Sigbjornsson, 1979] Langen, I. and Sigbjornsson, R. (1979). Dynamisk analyse av konstruksjoner, chapter 4 - Free vibration, pages 4.1–4.2. Tapir.
- [Larsen, 2014] Larsen, C. M. (2014). TMR4182 Marin dynamikk kompendium. Akademika forlag, 2014-edition edition.
- [Larsen et al., 2009] Larsen, C. M., Syvertsen, K., and Amdahl, J. (2009). TMR4167 Marin teknikk 2 kompendium. Department of Marine Technology, Faculty of Engineering, NTNU.
- [Leira, 2010] Leira, B. J. (2010). TMR4235 Stochastic theory of sealoading - Probabilistic modelling and estimation. Department of Marine Technology, NTNU.
- [Leira, 2014] Leira, B. J. (2014). TMR4170 Marine Structures Basic Course. Akademika forlag. NTNU Dept. Marine Technology.
- [Lwin, 2000] Lwin, M. M. (2000). Bridge Engineering Handbook, chapter Floating Bridges, pages 22.1–22.19. CRC Press.
- [Moan, 2003a] Moan, T. (2003a). TMR4190 - Finite element modeling and analysis of marine structures. Akademika forlag.
- [Moan, 2003b] Moan, T. (2003b). TMR4190 Finite element modelling and analysis of marine structures, chapter 12 Nonlinear analysis, page 118.
- [Moe et al., 1995] Moe, S., Allen, H. M., Høysæter, E., Wilhelmsen, T., and Hordaland, S. V. (1995). Nordhordland Bridge: Europe's longest floating bridge crosses the Salhus Fjord. Available at <http://www.nb.no/nbsok/nb/40eeca6b03c2a1e66940309894b9c335.nbdigital?lang=no#0>. Accessed 5.10.2017.

- [Myrhaug, 2005] Myrhaug, D. (2005). TMR4235 Stochastic theory of sealoads - Statistics of Narrow Band Process and Equivalent Linearization. Department of Marine Technology NTNU.
- [Myrhaug, 2006] Myrhaug, D. (2006). TMR4230 Oceanography, wind, waves. Akademika forlag.
- [Myrhaug, 2007] Myrhaug, D. (2007). TMR4180 Marine dynamics - Irregular sea. Akademika forlag. Department of Marine Technology NTNU.
- [Newland, 1993] Newland, D. E. (1993). An introduction to Random vibrations, spectral and wavelet analysis. Longman Scientific & Technical.
- [NORSOK, 2007] NORSOK (2007). N-003 actions and action effects.
- [NPRA, 2012] NPRA (2012). Delprosjekt fjordkryssing. Available at https://www.vegvesen.no/_attachment/435447/binary/731803. Accessed 26.09.2017.
- [NPRA, 2016] NPRA (2016). Multispan suspension bridge on floating foundation - technology development status. Available at https://www.vegvesen.no/_attachment/1545457/binary/1135151?fast_title=17+Flerspenns+hengebru+p%C3%A5+flytende+fundament.pdf. Accessed 25.09.2017.
- [NS-EN1992, 2004] NS-EN1992 (2004). Eurocode 2: Design of concrete structures - part 1-1: General rules and rules for buildings.
- [Olsen, 2008] Olsen, S. M. (2008). Broer i Norge. Vigmostad og Bjørke AS.
- [Project group, 2016] Project group, d. b. P. N. L. (2016). Straight bridge - navigation channel in south. Technical report, Aas-Jakobsen, COWI, Johs. Holt AS, Global Maritime.
- [Reiso et al., 2017] Reiso, M., Bjerkås, M., Søreide, T. H., Kolbjørn Høyland, T. F., Hasle, M., Furu, T., and Bjuhr, J. (2017). Artificial seabed; a mooring concept for crossing long and deep waterways. Structural Engineering International. Available at https://www.researchgate.net/publication/320197658_Artificial_seabed_a_mooring_concept_for_crossing_long_and_deep_waterways.
- [Riksantikvaren, Hovedkontor, 2008] Riksantikvaren, Hovedkontor (2008). Bergsøy-sundbrua - 153 svv nvp brunr 15-2221. Available at <https://kulturminnesok.no/minne/?queryString=https://data.kulturminne.no/askeladden/lokalitet/110598>. Accessed 03.10.2017.
- [Sande kommune, 2016] Sande kommune (2016). Kommunedelplan rovdefjordbrua - slutthandsaming og godkjenning. In Saksdokument Sak K-11/16. Sande kommune. Available at [www.sande-mr.kommune.no/files/documents/2016%2001%2026%20Kst%2011-16%20Kommunedelplan%20Rovdefjordbrua,%20slutthandsaming%20og%20godkjenning\(1\).pdf](http://www.sande-mr.kommune.no/files/documents/2016%2001%2026%20Kst%2011-16%20Kommunedelplan%20Rovdefjordbrua,%20slutthandsaming%20og%20godkjenning(1).pdf). Accessed 13.02.2018.
- [Snøhetta, 2016a] Snøhetta (2016a). Artificial seabed. Available at <https://snohetta.com/projects/203-artificial-seabed>.
- [Snøhetta, 2016b] Snøhetta (2016b). Kjøreopplevelse. Available at [https://www.vegvesen.no/_attachment/\\$1609942\\$/binary/\\$1145961\\$?](https://www.vegvesen.no/_attachment/1609942/binary/1145961?)

- fast_title=Kj%C\$3\$%B\$8\$reopplevelse+--+Julie+Aars.pdf. Accessed 12.02.2018.
- [Statens Vegvesen, 2011] Statens Vegvesen (2011). Mulighetsstudie - kryssning av sognefjorden. Technical report, Statens Vegvesen.
- [Statens Vegvesen, 2017] Statens Vegvesen (2017). Illustrations. Available at <https://www.vegvesen.no/vegprosjekter/ferjefrie39/illustrasjoner>. Accessed 06.10.2017.
- [Sørensen, 2013] Sørensen, S. I. (2013). Betongkonstruksjoner - Beregning og dimensjonering etter Eurokode 2. Fagbokforlaget. Del 2 - Spennbetong.
- [Vegdirektoratet, 2015] Vegdirektoratet (2015). Bruprojektering N400. N400 i Statens Vegvesens haandbokserie. Statens Vegvesen.
- [Xiang et al., 2017] Xiang, X., Eidem, M. E., Minoretti, T. E., Belsvik, K. H., and Vodolazkin, M. (2017). Simplified hydrodynamic design procedure of a submerged floating tube bridge across the digernessund of norway. page 11, OMAE2017-61189 Trondheim, Norway.
- [Øderud and Nordahl, 2017] Øderud, H. T. and Nordahl, R. S. (2017). Store Norske Leksikon, chapter Broer. Available at <https://snl.no/bro>. Accessed 20.09.2017.

Appendix A

Additional information about the SFT for the Digernessund gathered from the technical report

A.1 Load factors

Chart of load factors and load combinations

> Table 5-2 Load factors and load combinations for ultimate limit state (ULS)

Dominating variable load	Permanent loads						Post tension		Variable loads					
	Self-weight G ₁		Self-weight G ₂		Self-weight G ₃		Unfavourable	Favourable	Traffic		Wind, wave, current		Other variable loads	
	Max Buoy	Min Buoy	Max Buoy	Min Buoy	Max Buoy	Min Buoy			γ _Q	ψ ₀	γ _Q	ψ ₀	γ _Q	ψ ₀
Traffic	0.99	1.01	0.85	1.15	0	1.35	1.1	0.9	1.35	0.7	1.6	0.7	1.5	0.7
Wind, wave, current	0.99	1.01	0.85	1.15	0	1.35	1.1	0.9	1.35	0.7	1.6	0.7	1.5	0.7
Other variable loads	0.99	1.01	0.85	1.15	0	1.35	1.1	0.9	1.35	0.7	1.6	0.7	1.5	0.7

Dominerende variabel last	Permanente laster						Forspenning		Variable laster					
	Egenvekt G ₁		Egenvekt G ₂		Egenvekt G ₃		Risset tv. snitt		Trafikk		Vind, belge, strøm		Øvrige var. laster	
	Max Buoy	Min Buoy	Max Buoy	Min Buoy	Max Buoy	Min Buoy	Ugunstig	Gunstig	Ugunstig	Gunstig	Ugunstig	Gunstig	Ugunstig	Gunstig
Trafikk	0.99	1.01	0.9	1.15	0	1.35	1.1	0.9	0.945	0.00	1.12	0.00	1.05	0.00
Vind, belge, strøm	0.99	1.01	0.9	1.15	0	1.35	1.1	0.9	0.945	0.00	1.12	0.00	1.05	0.00
Øvrige variable	0.99	1.01	0.9	1.15	0	1.35	1.1	0.9	0.945	0.00	1.12	0.00	1.05	0.00

> Table 5-3 Load factor and load combinations for service limit state (SLS) when checking for membrane compression. Characteristic combination is assumed conservatively

Dominating variable load	Permanent loads						Post tension		Variable loads					
	Self-weight G ₁		Self-weight G ₂		Self-weight G ₃		Unfavourable	Favourable	Traffic		Wind, wave, current		Other variable loads	
	Max Buoy	Min Buoy	Max Buoy	Min Buoy	Max Buoy	Min Buoy			γ _{Q,1}	ψ _{0,1}	γ _{Q,1}	ψ _{0,1}	γ _{Q,1}	ψ _{0,1}
Traffic	1.0	1.0	1.0	1.0	1.0	1.0	1.0	1.0	1.0	0.7	1.0	0.7	1.0	0.7
Wind, wave, current	1.0	1.0	1.0	1.0	1.0	1.0	1.0	1.0	1.0	0.7	1.0	0.7	1.0	0.7
Other variable loads	1.0	1.0	1.0	1.0	1.0	1.0	1.0	1.0	1.0	0.7	1.0	0.7	1.0	0.7

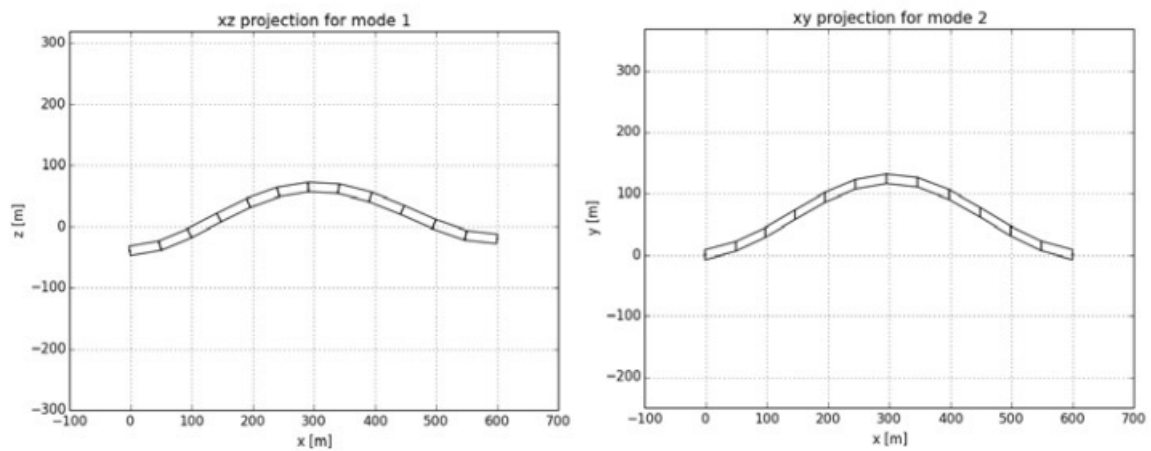
Figure A.1: Chart of load factors and load combinations used in the feasibility study of a SFT for Digernessund. [Engseth et al., 2016]

A.2 Eigenperiods calculated by the NPRA

The eigenperiods for mode 1-3 given in table A.1 are collected from [Engseth et al., 2016]. Eigenperiods for mode 4-10 were distributed by the NPRA [Minoretti, 2018]. The mode shapes for the first and second modes are given in fig. A.2.

Table A.1: Eigenperiods and frequencies calculated by the NPRA and dr. techn. Olav Olsen.[Engseth et al., 2016]

Mode	f_n (1/s)	T_n (s)
1	0.124	8.07
2	0.170	5.87
3	0.240	4.16
4	0.268	3.73
5	0.532	1.88
6	0.523	1.88
7	0.893	1.12
8	0.901	1.11
9	1.149	0.87
10	1.370	0.73



(a) Mode shape 1, vertical.

(b) Mode shape 2, horizontal.

Figure A.2: First and second mode shape calculated by dr. techn Olav Olsen. Illustrations: [Engseth et al., 2016]

Appendix B

Section properties

B.1 Summary of section properties

Table B.1: Summary of section properties for section 1-5 and average section

Parameters	Unit	1	2	3	4	5	Average section
h_1	m	18.49	17.86	17.24	16.61	16.3	17.55
h_2	m	5.19	4.56	3.93	3.31	3.00	4.254
b_1	m	12.2	12.2	12.2	12.2	12.2	12.2
b_2	m	10.6	10.6	10.6	10.6	10.6	10.6
t_1	m	0.8	0.8	0.8	0.8	0.8	0.8
t_2	m	1.0	1.0	1.0	1.0	1.0	0.8
t_3	m	0.3	0.3	0.3	0.3	0.3	0.3
A_c	m^2	61.30	60.30	59.30	58.30	57.8	59.8
I_z	m^4	2580	2379	2179	1978	1878	2279
I_y	m^4	1972	1851	1730	1640	1548	1790
I_t	m^4	6037	5769	5503	5238	5107	5636
W_z	m^3	422.91	390.04	357.17	324.30	307.87	381
W_y	m^3	207.48	207.22	200.67	197.43	189.91	203
W_t	m^3	360.88	348.68	336.48	324.28	318.18	343
S_y	m^3	104.04	98.99	94.05	89.24	86.34	95
S_z	m^3	87.03	83.32	80.67	77.49	75.90	83
$A_{sc,y}$	m^2	30.76	30.76	30.76	30.76	30.76	30.76
$A_{sc,z}$	m^2	32.69	31.32	29.94	28.57	27.88	30.63
c_y	m	0	0	0	0	0	0
c_z	m	0	0	0	0	0	0

B.2 Calculation of section properties

Moment of inertia

The general formula for moment of inertia I_y , adapted from [Irgens, 2006] (page. 413), is given in eq. B.1:

$$I_y = \int_A z^2 dA \quad (\text{B.1})$$

For simplifying the calculations of I_y , the cross-section of the SFT can be divided into i rectangles or "sub-elements", disregarding the brackets. The moment of inertia for rectangle i is given in eq. B.2, adapted from [Irgens, 2006] (page. 555).

$$I_{y,i} = \frac{h_i b_i^3}{12} \quad (\text{B.2})$$

When calculating the moment of inertia for a cross-section divided into i sub-elements, Steiners theorem has to be accounted for. According to [Irgens, 2006] (page. 198), Steiners theorem states the following:

$$I' = I + b^2 A \quad (\text{B.3})$$

I' is the total moment of inertia, including the effect of Steiners contribution, I is the moment of inertia for sub-part i , calculated according to eq. B.2, b is the distance between the COG of sub-element i and the total cross-section COG and A is the area of sub-element i .

Product of inertia about y - and z -axis I_{yz} , adapted from [Irgens, 2006] (page.413):

$$I_{yz} = I_{zy} = \int_A yz dA \quad (\text{B.4})$$

According to [Irgens, 2006], I_{yz} is zero if at least one of the axes is symmetric. It can be seen from 3.2 that the cross-section of the SFT is symmetric about y -axis. Thus, I_{yz} is zero.

Torsion moment of inertia I_t for thin-walled sections, corresponding to (IV.53) on page IV.30 in [Leira, 2014]:

$$I_t = \frac{4A_0^2}{\int_s \frac{ds}{t}} \quad (\text{B.5})$$

where t is the thickness, ds is a small element length and the A_0 is the circumscribed area of the cross-section.

However, the cross-section of the SFT in this thesis is not a thin-walled one. Prof. Bernt Leira recommended to increase the torsion moment of inertia by 20 – 50% due to the fact that the SFT is not thin-walled.

Static area moment

Static area moment about y- and z-axis [Irgens, 2006] (page.421).

$$S_z = \int_{A'} y dA \quad (\text{B.6})$$

Static area moment about z-axis

$$S_y = \int_{A'} z dA \quad (\text{B.7})$$

where A' is the area of a sub-element, and y and z represents the distance from the sub-element COG to the element COG.

Section modulus

Minimum section modulus W_y and W_z , about y- and z-axis respectively, adapted from [Irgens, 2006] (p.194-196):

$$W_y = \frac{I_y}{z} \quad (\text{B.8})$$

$$W_z = \frac{I_z}{y} \quad (\text{B.9})$$

I_y and I_z represents the moment of inertia about y- and z-axis, respectively. z and y represents the largest distances from the outer fibers of the cross-section to the neutral axis.

Minimum torsional section modulus about shear center W_t , for an arbitrary cross-section, adapted from [Irgens, 2006] (p.485-486):

$$W_t = 2 \sum_{i=1}^n \bar{A}_i t_i \quad (\text{B.10})$$

Eq. B.10 is based on the idea of dividing the cross-section into n rings. Each ring forms a sub-cross-section with constant thickness t_i and \bar{A}_i . The latter is the area enclosed by the ring. [Irgens, 2006]

Shear center

In the case of doubly symmetric cross-sections, the shear center is located at the intersection point between the two axes of symmetry ([Leira, 2014] p.17).

B.3 Method for approximation of varying cross-section

The idea of the approximation is to have elements with constant cross-sections.

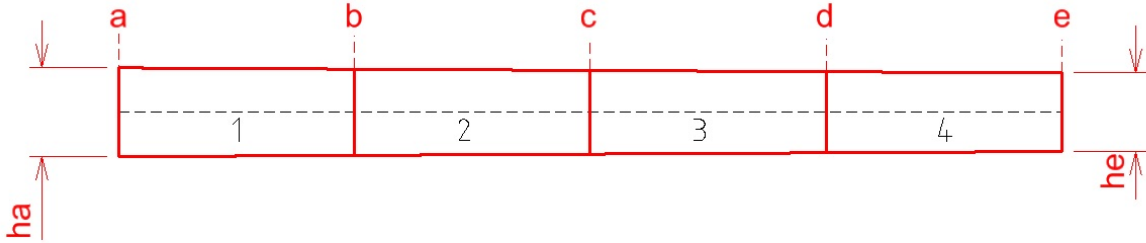


Figure B.1: Illustration of the part with linearly varying cross-section

The figure B.1 show that the part with linearly varying cross-section is divided into 4 elements with equal length. Each element has an varying cross-section, e.g. for element 1, the cross-section vary form a to b.

The outer heights (h_1) for cross-sections a and e are known from [Engseth et al., 2016], ie. 3.2 ii and i respectively. The height for cross-section c, h_{c1} is then assumed by taking the average of h_a and h_e :

$$h_{c1} = \frac{h_a + h_e}{2} \quad (\text{B.11})$$

When h_{c1} is known, the heights for the cross-sections b and d can be found in similar way.

Having the height for all cross-sections a, b, c, d and e, the heights for the approximated elements can be found by taking the average of the two heights at the ends of the element, e.g. for element 1:

$$h_1 = \frac{h_a + h_b}{2} \quad (\text{B.12})$$

Appendix C

Curved model

A sketch of the curved bridge model, corresponding to the red dotted line, is given in fig. C.1. Note again that this curved configuration is in the horizontal plane. In the technical report [Engseth et al., 2016], the radius was given $R = 1850m$ and total span of the bridge $L = 600m$. By trigonometry and geometric considerations, the length of the crossing (air line) between the abutments is thus $597.16m$.

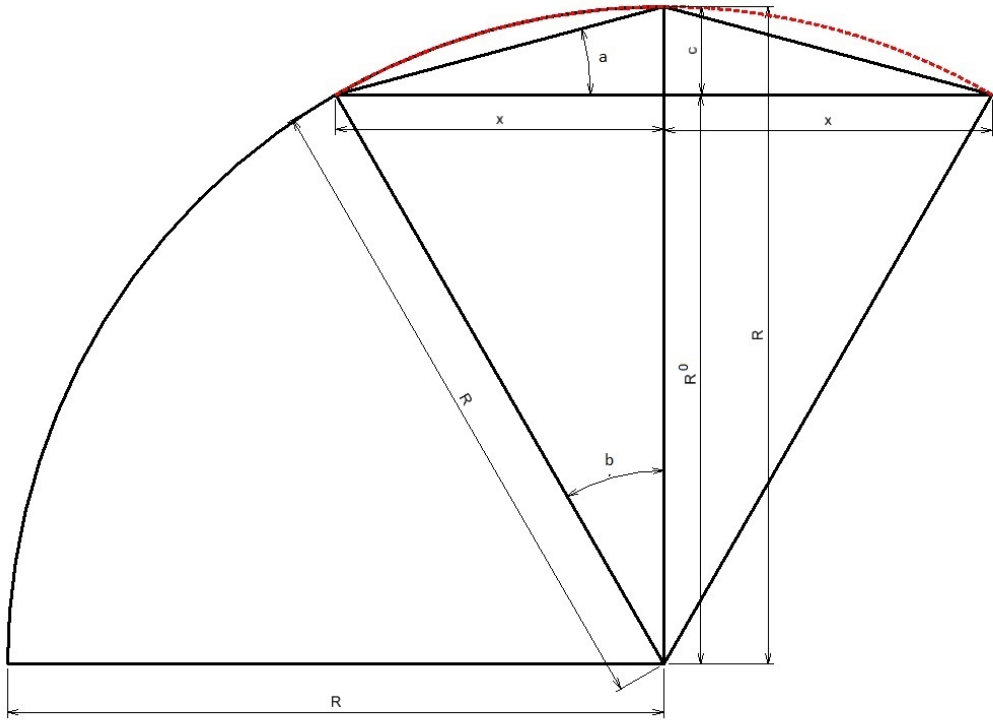


Figure C.1

In the second curve model another curve height was investigated. Keeping the length of the crossing between the abutments constant, the new radius can be found by Pythagorean theorem eq.C.1. Rearranging the equation give the radius (eq.C.2).

$$R^2 = x^2 + (R - c)^2 \tag{C.1}$$

$$R = \frac{x^2 + c^2}{2c} \quad (C.2)$$

When the new radius is known, angle b can be found by trigonometry. This angle is needed to establish the curve in GeniE/Abaqus. The angle b can be divided into n angles, where n is the number of times the centerline is rotated (see the subsection below). Thus, n is also the number of elements for half the bridge.

Establishing a curved model in GeniE

Fig. C.2 show the geometrical model used to find the location of the bridge elements and thus how to establish the global model of the bridge. This figure show one half of the bridge due to symmetry. The bridge is modeled as an arc consisting of n straight beam elements with equal length of L_e m. The straight beam elements are represented as the red lines in the figure. The radius of the arc, corresponding to horizontal alignment, is represented as R .

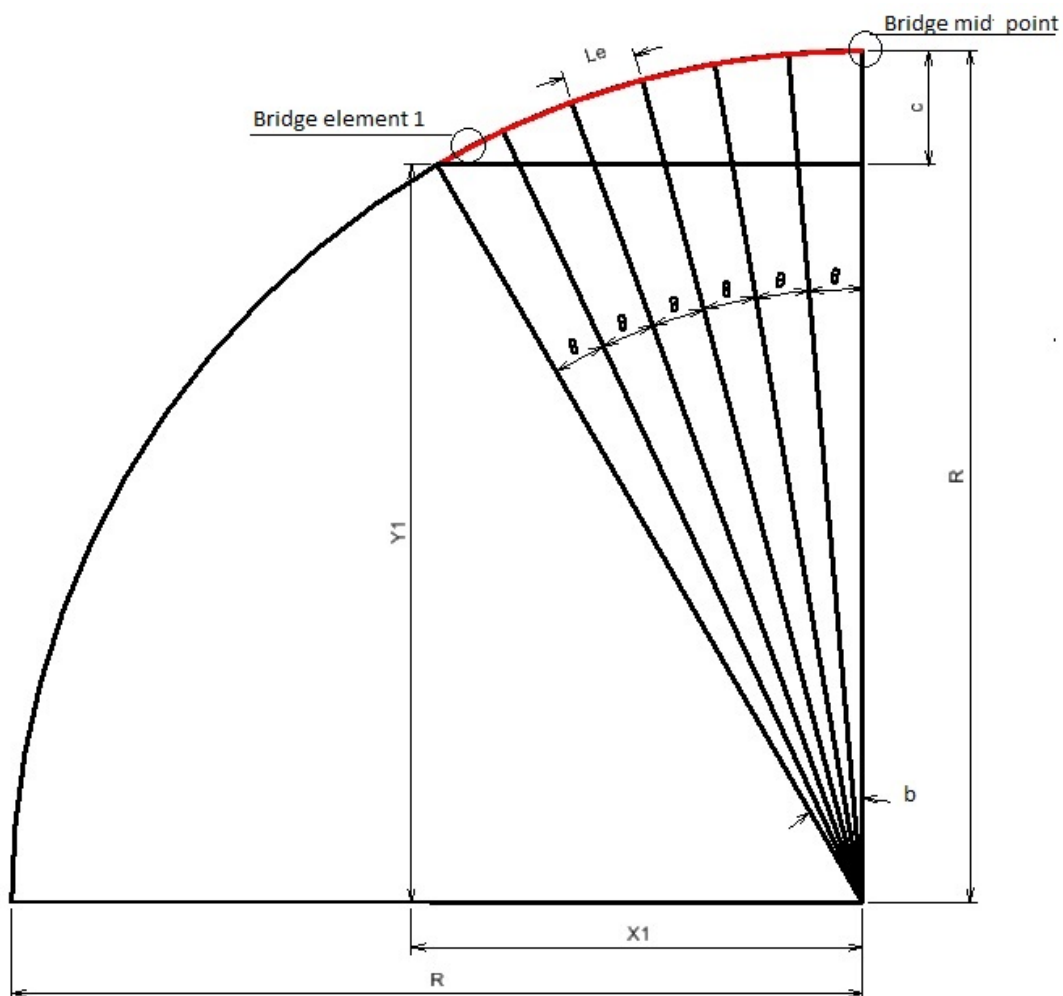


Figure C.2: Arc model showing how the positions of the bridge elements are found.

In GeniE, the arc was established using GeniE user manual tutorials, [DNV-GLsoftware, 2015], which gives a step-wise introduction to modeling of arcs in GeniE. Fig. C.3 show how the curved model is established by defining guiding plane and lines. When establishing the curve, half of the bridge is considered. Because of symmetry, the model can be mirrored to get the total arc.

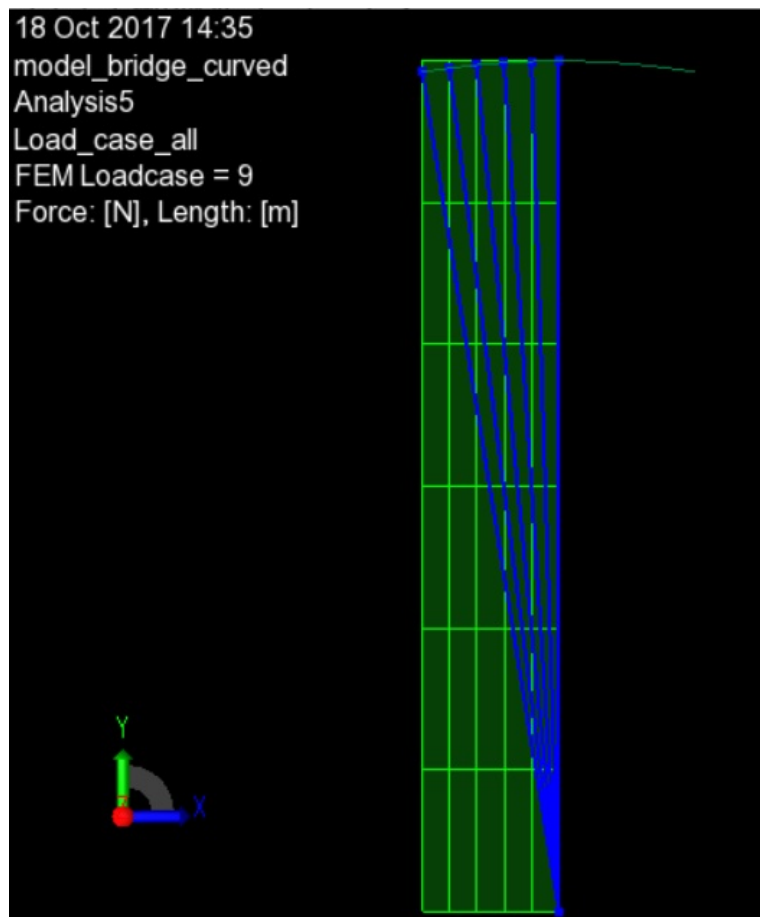


Figure C.3: Establishing curved model

The green lines represents the guiding plane, which has height equal to the radius of the arc. The width of the guiding plane, corresponding to X1 in fig. C.2, has to be found by geometrical considerations.

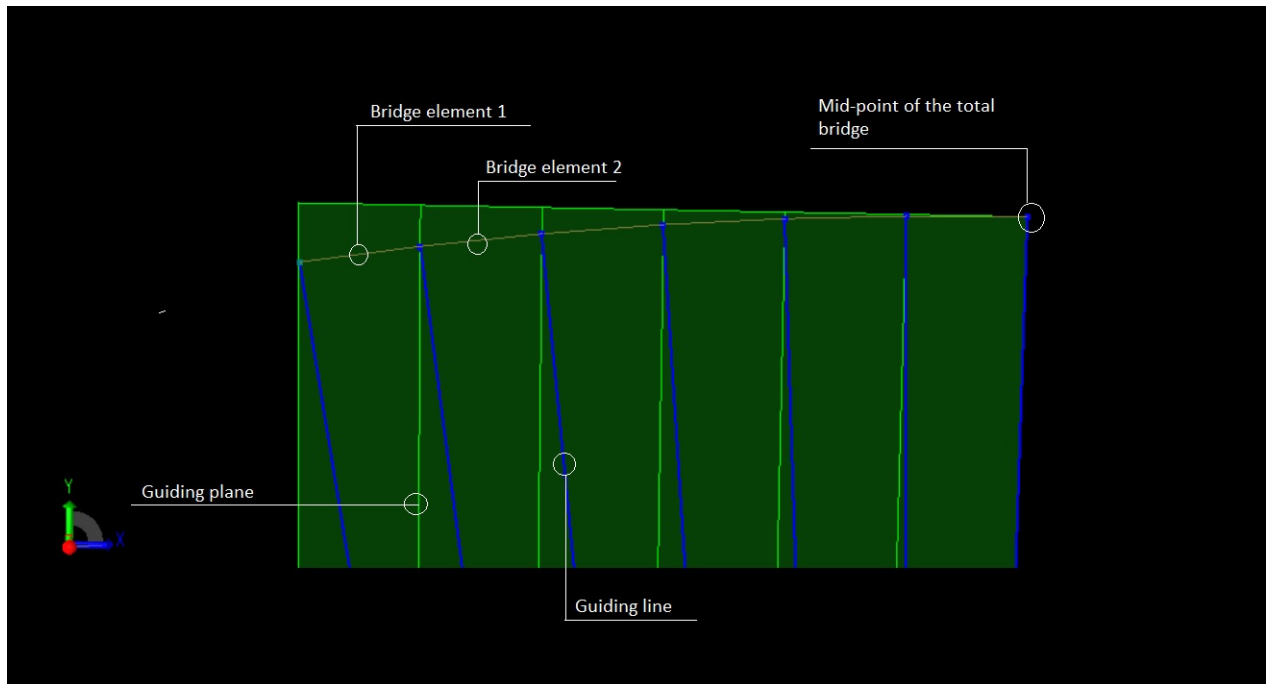


Figure C.4: Cut-out of the curve-model in GeniE, showing half the bridge

Before establishing the arc, some helping lines (blue) are drew. The top points of these helping lines corresponds to the location of the nodes for the straight beam elements. The upper right corner of the guiding plane, and the top point of the first guiding line from the right, corresponds to the mid point of the total bridge. To find the location of the next nodes, the blue guiding line is rotated an angle of θ n times. θ is found by trigonometric considerations. Then, straight beam elements are drew between the upper points of the blue guiding lines, resulting in half of the total arc. Finally, the arc can be mirrored about the mid point of the bridge to achieve the total model (fig.C.5).



Figure C.5: Global model, xy-plane

Appendix D

Material densities

Table D.1: Total material densities for section 1 to 5, with linearly varying ballast

Section	SLS ρ (kg/m ³)	ULS max buoyancy ρ_{maxb} (kg/m ³)
1	3826	3684
2	3655	3513
3	3494	3352
4	3343	3202
5	3199	3058

For the case with constant average cross-section throughout the structure length, an average is taken between the two given ballast fills (average between the ballast fill corresponding to the largest and smallest cross-section given in the technical report). The average ballast fill is given in table 5.3. Table D.2 show the resulting material densities for the case with average constant cross-section, including the contribution from ballast and all other weights. Load factors, which are given in section 6.3, are applied to all respective contributions to achieve the correct mass of the structure.

Table D.2: Total material densities for average section and section 5, with constant ballast

Section	SLS ρ (kg/m ³)	ULS max buoyancy ρ_{maxb} (kg/m ³)
Average	3486	3345

Appendix E

Reinforcements and PT-cables

E.1 Summary of ordinary reinforcements

Table E.1: Total minimum longitudinal reinforcement areas mm^2 for section 1 to 5

Section	Type	1	2	3	4	5
Outer walls	Horizontal	161867.68	155731.68	14595.68	143459.69	140391.68
	Vertical	161864.38	155728.5	149592.63	143456.76	140388.82
Inner walls	Horizontal	21961.96	19316.96	16671.96	14026.96	12704.72
Top/bottom slab	Horizontal	49058.64	49058.64	49058.64	49058.64	49058.64
Inner slab	Horizontal	42624.72	42624.72	42624.72	42624.72	42634.72

E.2 Sketch of reinforcements and PT-cables

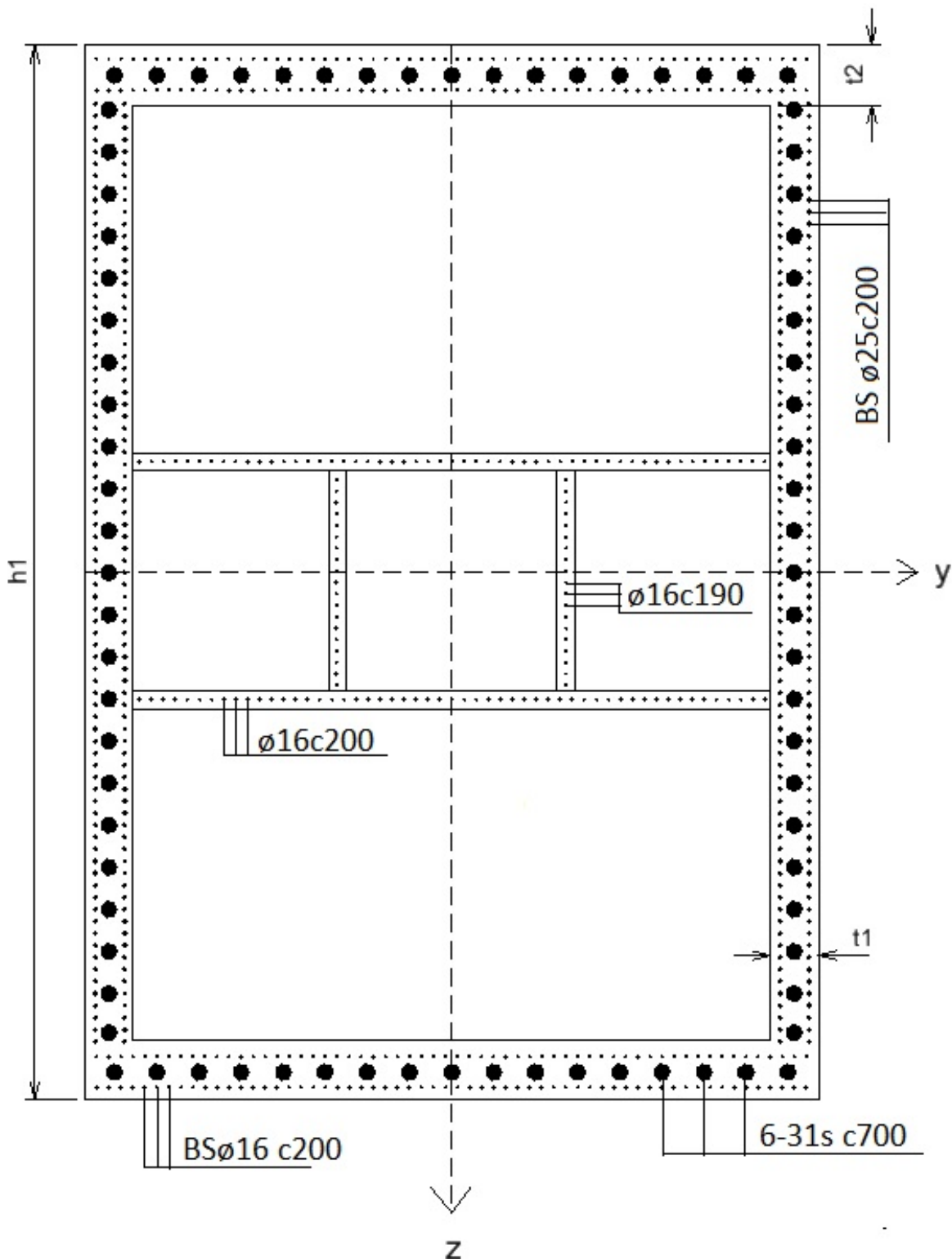


Figure E.1: Sketch of cross-section with minimum reinforcements and PT-cables. Only the longitudinal reinforcements are included for simplicity.

Appendix F

Transformed cross-section

F.1 Summary of transformed cross-section properties

Table F.1: Calculated transformed moment of inertia and transformed area for section 1 to 5

Section	1	2	3	4	5
$I_{tz} (m^4)$	2673.5	2463.3	2267.5	2059.3	1955.3
$I_{ty} (m^4)$	2029.9	1907.9	1785.8	1695.3	1602.8
$A_v m^2$	63.20	62.17	61.13	60.09	59.57

Table F.2: Calculated transformed moment of inertia for average section

Section	Average section
$I_{tz} (m^4)$	2369.8
$I_{ty} (m^4)$	1846.3

F.2 Transformed moment of inertia calculations

F.2.1 Transformed moment of inertia about z-axis

$$I_{t,z} = I_{z,bet} + I_{z,s} + I_{z,p} \quad (F.1)$$

As described in section 5.4.1, the transformed moment of inertia about z-direction, $I_{t,z}$, includes contributions from concrete, $I_{z,bet}$, ordinary reinforcements, $I_{z,s}$, and PT-cables, $I_{z,p}$. These contributions are kept separate when calculated below.

Total contribution from ordinary reinforcements

For the horizontal decks:

$$I_{z,s1} = 2(\eta - 1)A_{s1}e_1^2 + 2(\eta - 1)A_{s3}e_2^2 \quad (F.2)$$

where A_{s1} is the total area for horizontal reinforcements per deck (bottom or top slab), whereas A_{s3} is the total area for horizontal reinforcements per inner deck. e_1 and e_2 is the vertical distances from the reinforcements COG to the cross section COG.

For vertical walls (both outer and inner walls):

$$I_{z,s2} = 2 * 2 * (\eta - 1) \left(\frac{A_{s2}}{2} \right) e_3^2 + 2 * 2 * (\eta - 1) \left(\frac{A_{s4}}{2} \right) e_4^2 \quad (\text{F.3})$$

where A_{s2} is the total area of horizontal reinforcements per outer wall, whereas A_{s4} is the total area of horizontal reinforcements per inner wall. To account for the horizontal reinforcements in the walls a simplification is made. Each wall is divided in two parts. It is assumed, for each part of the wall, that the position of the local COG, corresponding to the horizontal reinforcements in the respective part, is placed halfway. The vertical distances from the reinforcement COG to the cross-section COG is therefore e_3 and e_4 for the respective parts. See definitions below.

Total contribution from PT-cables

For the horizontal decks:

$$I_{z,p1} = 2(\eta_p - 1)A_{p1}e_1^2 \quad (\text{F.4})$$

where A_{p1} is the total area of longitudinal PT-cables per slab (bottom or top). e_1 represents the vertical distance from PT-cables COG to the cross-section COG.

For the vertical outer walls:

$$I_{z,p2} = 2 * 2(\eta_p - 1) \left(\frac{A_{p2}}{2} \right) e_3^2 \quad (\text{F.5})$$

Here, A_{p2} is the total area of longitudinal PT-cables per wall. The same simplification, as described above for the ordinary reinforcements, is made for the longitudinal PT-cables in the walls.

The vertical distances e_1, e_2, e_3 and e_4 to the cross-section COG are defined below.

$$e_1 = \frac{h_1}{2} + \frac{t_2}{2} \quad (\text{F.6})$$

$$e_2 = \frac{3.002}{2} + \frac{t_3}{2} \quad (\text{F.7})$$

$$e_3 = \frac{h_1}{4} \quad (\text{F.8})$$

$$e_4 = \frac{3.002}{4} \quad (\text{F.9})$$

F.2.2 Transformed moment of inertia about y-axis

The same simplification, as described in sec.F.2.1, is made in this section for the reinforcements and PT-cables in the horizontal decks. Thus, the decks are here divided into two parts, and the COG of the reinforcements or PT-cables is halfway in each of the deck-parts.

Total contributions from ordinary reinforcements

For horizontal deck/slab:

$$I_{y,s1} = 2 * 2 * (\eta - 1) \frac{A_{s1}}{2} a_3^2 + 2 * 2 * (\eta - 1) \frac{A_{s3}}{2} a_3^2 \quad (\text{F.10})$$

A_{s1} and A_{s2} were defined in section F.2.1. a_3 is the horizontal distance between the reinforcements COG and the cross-section COG. See definitions below.

For the vertical walls:

$$I_{y,s2} = 2(\eta - 1) A_{s2} a_1^2 + 2(\eta - 1) A_{s4} a_2^2 \quad (\text{F.11})$$

A_{s2} and A_{s4} were also defined in section F.2.1. a_1 and a_2 are horizontal distances from the reinforcements COG to the cross-section COG.

Total contributions from PT-cables

For horizontal decks:

$$I_{y,p1} = 2 * 2(\eta_p - 1) \frac{A_{p1}}{2} a_3^2 \quad (\text{F.12})$$

$$I_{y,p2} = 2(\eta_p - 1) A_{p2} a_1^2 \quad (\text{F.13})$$

A_{p1} and A_{p2} were defined in section F.2.1.

The horizontal distances a_1 , a_2 and a_3 to the cross-section COG is defined below.

$$a_1 = \frac{b_1}{2} - \frac{t_1}{2} \quad (\text{F.14})$$

$$a_2 = \frac{3.2}{2} + \frac{t_3}{2} \quad (\text{F.15})$$

$$a_3 = \frac{b_1}{4} \quad (\text{F.16})$$

Appendix G

Additional results from structural analysis

G.1 Additional static analysis results

G.1.1 Sensitivity study of current direction in SLS condition.

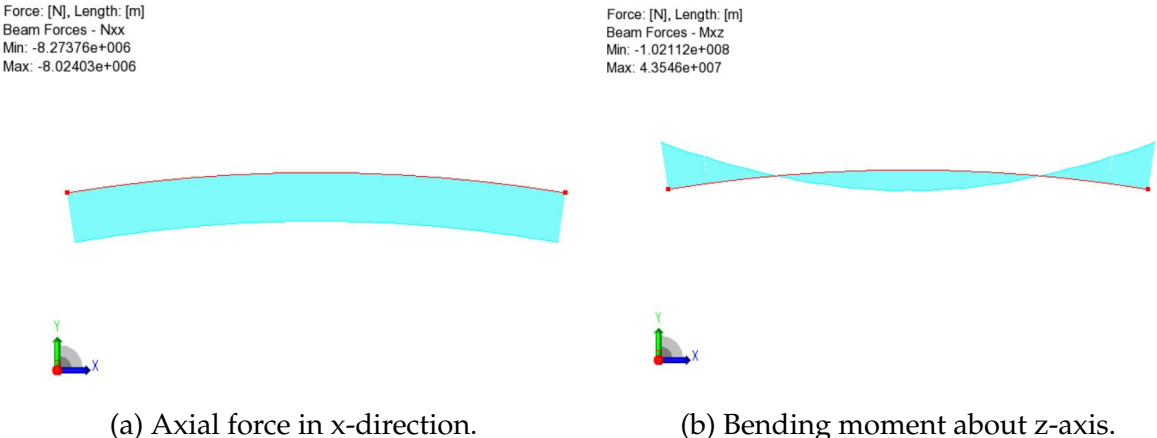
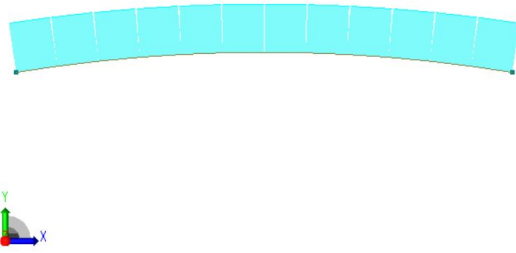


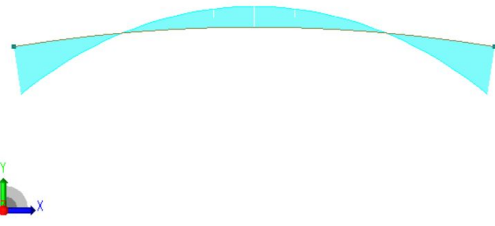
Figure G.1: Constant current applied in negative y-direction over the full length of the fjord.

Force: [N], Length: [m]
 Beam Forces - Nxx
 Min: 8.02403e+006
 Max: 8.27376e+006



(a) Axial force in x-direction.

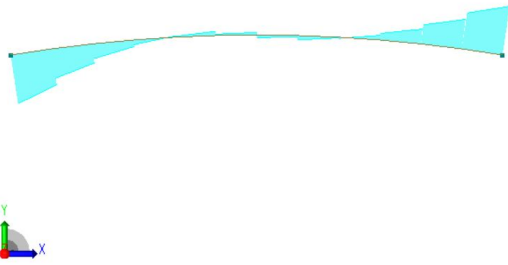
Force: [N], Length: [m]
 Beam Forces - Mxz
 Min: -4.3546e+007
 Max: 1.02112e+008



(b) Bending moment in z-direction.

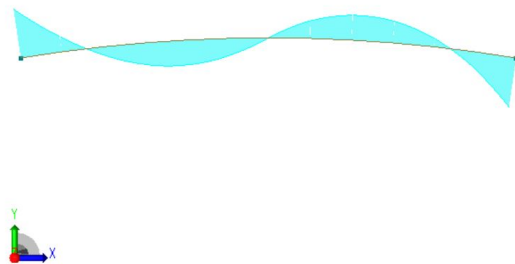
Figure G.2: Constant current applied in positive y-direction over the full length of the fjord.

Force: [N], Length: [m]
 Beam Forces - Nxx
 Min: -213949
 Max: 213950



(a) Axial force in x-direction

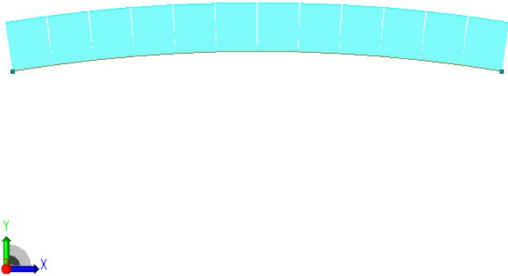
Force: [N], Length: [m]
 Beam Forces - Mxz
 Min: -9.04948e+007
 Max: 9.04948e+007



(b) Bending moment in z-direction.

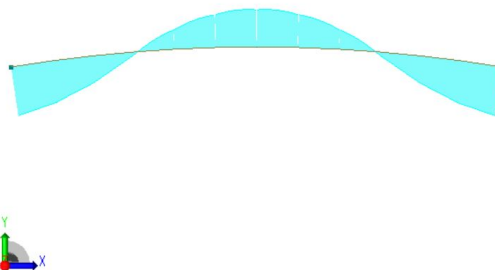
Figure G.3: Constant current applied asymmetrically in y-direction over the full length of the fjord.

Force: [N], Length: [m]
 Beam Forces - Nxx
 Min: 6.40647e+006
 Max: 6.50516e+006



(a) Axial force in x-direction.

Force: [N], Length: [m]
 Beam Forces - Mxz
 Min: -4.32829e+007
 Max: 5.66784e+007

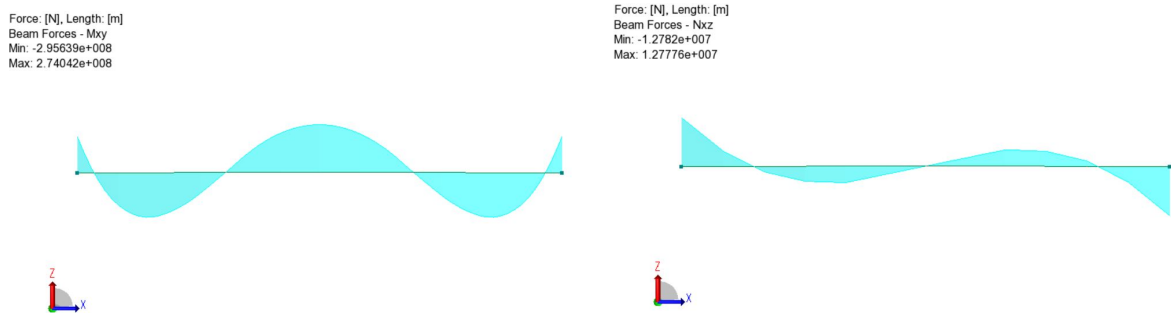


(b) Bending moment about z-direction.

Figure G.4: Constant current applied in negative y-direction at the mid-section over a length of 300m of the bridge.

G.1.2 Static analysis results for case with specific weight of reinforced concrete $26.5kN/m^3$

In the technical report [Engseth et al., 2016], $26.5kN/m^3$ was used as the specific weight of reinforced concrete in hand-calculations. This section includes results from static analysis in SLS if this specific weight is used.



(a) Resulting distribution of bending moments about y-axis if $26.5kN/m^3$ is used as density of reinforced concrete.

(b) Resulting distribution of shear forces in z-direction if $26.5kN/m^3$ is used as density of reinforced concrete.

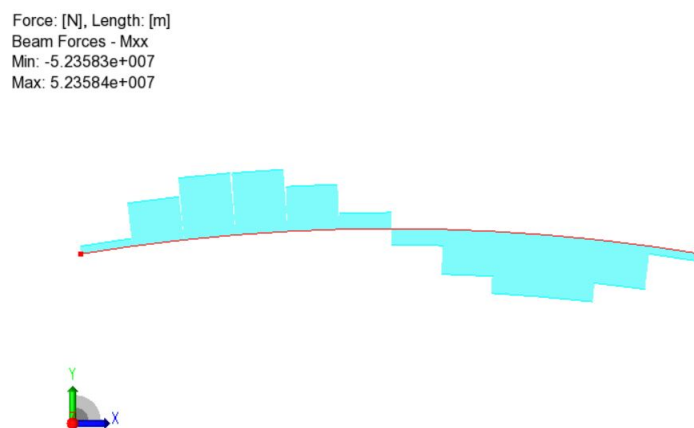


Figure G.6: Resulting distribution of torsion moment if $26.5kN/m^3$ is used as density of reinforced concrete.

Table G.1: Bending moments and reaction forces due to net vertical forces, SLS.

	Results
$M_{xy,ends}$ (GNm)	-0.222
$M_{xy,mid}$ (GNm)	-0.296
F_z (MN)	12.78

The bending moments are reduced with a factor of ten compared to the results of static analysis with specific weight of concrete $25kN/m^3$. The largest bending moment is here located at the midspan. With a positive current force, giving axial tension in the concrete, the concrete stresses were calculated at the most critical location with respect

to tension at midspan. Looking at the distribution of bending moments, the critical location wrt tension was the upper corner to the right. The concrete stress was here calculated $-5.160\text{N}/\text{mm}^2$. Thus, the concrete is in compression even though the current is subjecting the bridge to axial tension forces.

For the case with a negative current force, giving compression in the concrete, the concrete stresses were calculated at the most critical location with respect to compression at midspan. Looking at the distribution of bending moments, the critical location wrt compression was the lower left corner. Here, the concrete stress was calculated $-9.26\text{N}/\text{mm}^2$.

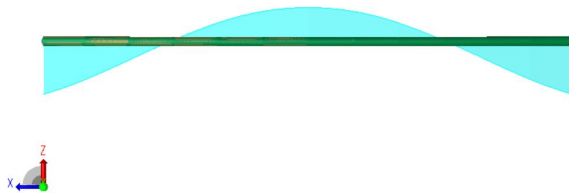
G.1.3 Static analysis results for alternative ballast cases

Two additional ballast amounts were investigated (tab.G.2). The resulting net bending moments about y-axis are given in fig.G.7. The maximal concrete stress in the most critical sections with respect to tension are given in tab.G.3.

Table G.2: Ballast fill percentages for three different ballast cases.

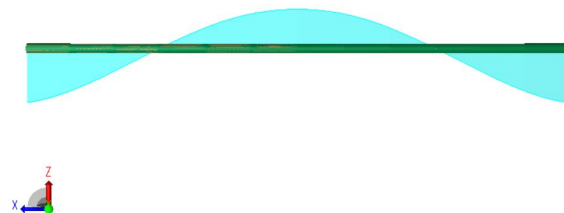
Case	1 (%)	2 (%)
Base	60.4	79.0
a	62.2	81.4
b	65.0	85.0

Force: [N], Length: [m]
Beam Forces - Mxy
Min: -1.37233e+009
Max: 2.17845e+009



(a) Net bending moment about y-axis for ballast case a.

Force: [N], Length: [m]
Beam Forces - Mxy
Min: -1.16708e+009
Max: 1.64171e+009



(b) Net bending moment about y-axis for ballast case b.

Figure G.7: Net bending moments about y-axis for alternative ballast cases.

Table G.3: Maximal concrete stress in most critical section with respect to tension.

Ballast case	σ_c N/mm^2	Utilization(%)
Base	5.7	135.7
a	4.1	97.9
b	1.6	33.1

G.2 Additional eigenvalue analysis results

G.2.1 Results for straight bridge model

The results in this section are based on a straight bridge model with constant average cross-section and constant mass over the bridge length. All rotations and translations are fixed at the bridge ends.

Analytical solutions for straight bridge

Table G.4: Vertical (V) and horizontal (H) eigenperiods and frequencies for straight bridge.

Mode	H/V	ω_n (rad/s)	f_n (1/s)	T_n (s)
1	V	0.677	0.108	9.277
2	V	1.866	0.297	3.365
3	V	3.658	0.582	1.717
4	V	6.042	0.962	1.039
5	V	9.025	1.436	0.696
1	H	0.764	1.122	8.222
2	H	2.106	0.335	2.982
3	H	4.128	0.657	1.521
4	H	6.817	1.085	0.921
5	H	10.183	1.621	0.617

Results from Sestra and Abaqus for straight bridge

Table G.5: Eigenperiods and frequencies obtained with Sestra and Abaqus.

Mode	H/V	Sestra			Abaqus		
		f_n (1/s)	T_n (s)	D_{an} (%)	f_n (1/s)	T_n (s)	D_{an} (%)
1	V	0.107	9.363	0.93	0.109	9.175	-1.10
2	H	0.120	8.317	1.16	0.123	8.134	-1.07
3	V	0.291	3.435	2.08	0.304	3.284	-2.39
4	H	0.327	3.059	2.58	0.343	2.914	-2.28
5	V	0.563	1.776	3.44	0.608	1.645	-4.21
6	H	0.630	1.587	4.34	0.685	1.460	-3.98
7	V	0.916	1.092	5.10	1.031	0.970	-6.61
8	H	1.022	0.979	6.30	1.159	0.863	-6.34
9	V	1.346	0.743	6.75	1.592	0.628	-9.74
10	H	1.496	0.669	8.43	1.787	0.560	-9.28

Results from convergence test in Sestra

Table G.6: Convergence test for straight bridge model. D_{an} is the deviation from the analytical calculation results for straight beam.

Mode	$L_e = 50m$		$L_e = 25m$		$L_e = 20m$		$L_e = 15m$	
	T_n (s)	D_{an} (%)	T_n (s)	D_{an} (%)	T_n (s)	D_{an} (%)	T_n (s)	D_{an} (%)
1	9.3659	0.95	9.3641	0.93	9.3641	0.93	9.3641	0.93
2	8.3194	1.18	8.3199	1.19	8.3199	1.19	8.3199	1.19
3	3.4595	2.80	3.4353	2.08	3.4354	2.08	3.4354	2.08
4	3.0599	2.51	3.0610	2.64	3.0611	2.64	3.0612	2.64
5	1.7769	3.51	1.7773	3.54	1.7775	3.55	1.7777	3.56
6	1.5873	4.34	1.5893	4.47	1.5896	4.48	1.5897	4.49
7	1.0919	5.05	1.0934	5.19	1.0940	5.24	1.0942	5.26
8	0.9789	6.26	0.9820	6.60	0.9823	6.63	0.9825	6.66
9	0.7433	6.83	0.7465	7.28	0.7469	7.34	0.7472	7.38
10	0.6689	8.46	0.6733	9.18	0.6737	9.25	0.6740	9.30

G.2.2 Results for curved bridge model

Analytical results

Table G.7: Analytical results for curved beam, constant cross-section, vertical (V) and horizontal (H) modes.

Mode	H/V	ω_n (rad/s)	f_n (1/s)	T_n (s)
1	V	0.678	0.108	9.268
2	V	1.868	0.297	3.362
3	V	3.662	0.583	1.715
4	V	6.048	0.963	1.038
5	V	9.034	1.439	0.695
1	H	1.247	0.199	5.037
2	H	2.113	0.337	2.972
3	H	4.143	0.660	1.516
4	H	6.842	1.090	0.918
5	H	10.221	1.628	0.614

Results from Sestra and Abaqus

Table G.8: Eigenperiods and frequencies for curved model, constant cross-section, obtained with Sestra and Abaqus.

Mode	H/V	Sestra			Abaqus		
		f_n (1/s)	T_n (s)	D_{an} (%)	f_n (1/s)	T_n (s)	D_{an} (%)
1	V	0.107	9.390	1.32	0.110	9.123	-1.56
2	H	0.186	5.381	6.83	0.189	5.299	5.20
3	V	0.291	3.438	2.26	0.307	3.261	-2.99
4	H	0.326	3.064	3.10	0.347	2.884	-2.97
5	V	0.563	1.777	3.62	0.613	1.632	-4.83
6	H	0.633	1.579	4.16	0.695	1.438	-5.14
7	V	0.916	1.091	5.11	1.039	0.963	-7.26
8	H	1.022	0.979	6.64	1.172	0.853	-7.08
9	V	1.346	0.743	6.91	1.605	0.623	-10.33
10	H	1.496	0.668	8.72	1.808	0.553	-9.97

G.2.3 Additional results from parameter studies with curve height

Table G.9: Results for the first six modes from parameter study with curve height.

Mode	H/V	An. $C = 49m$		Sestra $C = 53m$		Abaqus $C = 56m$	
		f_n (1/s)	T_n (s)	f_n (1/s)	T_n (s)	f_n (1/s)	T_n (s)
1	V	0.109	9.190	0.106	9.406	0.103	9.748
2	V	0.300	3.333	0.284	3.519	0.285	3.504
3	H	0.339	2.950	0.315	3.175	0.326	3.064
4	H	0.339	2.950	0.326	3.064	0.329	3.036
5	V	0.588	1.701	0.545	1.834	0.563	1.778
6	H	0.665	1.504	0.624	1.603	0.664	1.505

G.2.4 Abaqus eigenvalue analysis with axial compression from PT-cables

Abaqus was used to investigate how the compression from PT-cables affect the eigenperiods and mode shapes of the bridge. Two analyses were carried out, one with the straight configuration and one with the base case. The analysis with the straight configuration was conducted to compare the results from Abaqus to the analytical results (see sec. 7.1 and 7.4.1).

The compression forces were applied as "bolt loads" in Abaqus at both ends of the bridge. Both ends were considered fixed for all rotations and translations. The bolt loads were applied at both ends in a step prior to the eigenvalue-analysis step. To account for the non-linear geometric effects due to the applied pre-load, the NL-GEOM option was checked. See Abaqus user manual for more information about the meaning of bolt loads and the NL-GEOM option.

The results from the two analyses, discussed in the following, were found rather strange for both the straight bridge and the base case.

Straight bridge configuration with applied compression forces from PT-cables

Table G.10: Results for eigenvalue analysis in Abaqus for straight bridge. Results with and without compression from PT-cables are compared.

Mode	Abaqus res.	Abaqus res. w/bolt loads	D (%)
	f_n (1/s)	f_n (1/s)	
1	0.109	0.000	(-)
2	0.123	0.106	-2.69
3	0.305	1.020	-2.10
4	0.343	0.301	-1.24
5	0.608	0.340	-0.96
6	0.685	0.604	-0.63
7	1.031	0.681	-0.49
8	1.159	1.027	-0.34
9	1.592	1.156	-0.27

Table G.10 show the results from eigenvalue analysis of the straight bridge configuration in Abaqus with and without applied compression forces from PT-cables. When applying compression forces, the first eigenfrequency given by Abaqus is 0.000s. This was unexpected, and it was found difficult to figure out why the first eigenfrequency is zero. The eigenfrequency for the model without the applied compression was compared to the results from GeniE for the corresponding case (straight bridge), and the deviations was found within 5% for the first four modes. All inputs to Abaqus and modelling-steps in Abaqus was double-checked to screen for errors.

Now, lets call the case with applied compression force "case 2", and the case without the applied compression force "case 1". The next resulting eigenfrequencies (modes 2-10) for the case 2, are similar to the eigenfrequencies for mode 1-9 for case 1. The eigenfrequency for mode 1 case 1 is similar to the period for mode 2 case 2, and so on. The deviation between the corresponding modes are given as D in the same table.

The analytical calculated reductions of eigenfrequency due to axial compression for the straight bridge configuration were presented in tab.7.2. The reduction was calculated for the first modes to approximately -2.83% . In Abaqus, the reduction from the first mode for case 1, to the second mode for case 2, was found -2.69% . As for the analytical reduction results, the reduction is reduced for increasing mode number. Thus, there exists similarities between the analytical calculation model and the results from Abaqus when applying the compression forces from PT-cables. However, because of the strange first mode in Abaqus, the Abaqus model and modelling technique with bolt-loads in Abaqus should be further investigated to accept and utilize the results.

Base case bridge with applied compression forces from PT-cables

Table G.11: Abaqus results for curved structure subjected to bolt loads.

Mode	Abaqus res.	Abaqus res. w/bolt loads	D (%)
	f_n (1/s)	f_n (1/s)	
1	0.115	0.008	(-)
2	0.196	0.112	-2.57
3	0.313	0.126	-35.70
4	0.352	0.309	-1.27
5	0.619	0.348	-0.92
6	0.698	0.615	-0.65
7	1.042	0.691	-1.03
8	1.169	1.038	-0.37
9	1.608	1.166	-0.26

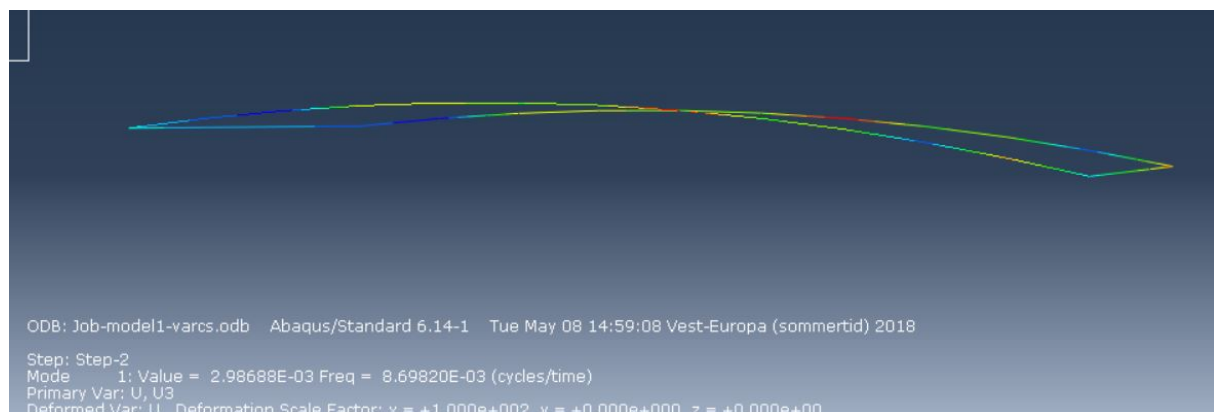
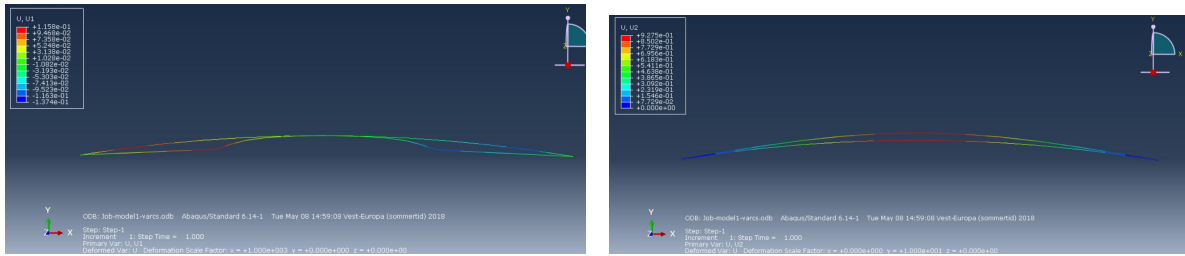


Figure G.8: First horizontal mode when the structure is subjected to bolt loads.

Table G.11 show the results from eigenvalue analysis of the base case configuration in Abaqus with and without applied compression forces from PT-cables. When applying compression forces, the first eigenfrequency given by Abaqus is 0.008s which corresponds to a period of 114s. The mode shape for the first mode is given in fig.G.8. Both the low eigenfrequency and the mode shape for the first mode were unexpected. The next eigenfrequencies (modes 2-10) for the case of applying compression (case 2), are similar to the eigenfrequencies for mode 1-9 for case without compression forces (case 1). The eigenfrequency for mode 1 case 1 is similar to the period for mode 2 case 2, and so on. The deviation between the corresponding modes are given as D in the same table. It is observed that for the base case configuration, the second horizontal mode for case 2 deviates from case 1 by approximately 36%.

The bolt loads were applied in a step prior to the eigenvalue analysis to obtain a new reference with the deformed configuration. Investigating the deformed configuration, it is observed that the bolt loads cause an deformation in x-direction with maximum value 0.8515m, and a deformation in y-direction with maximum value 0.1283m. Scaled deformations are showed for x- and y-direction in fig.G.9a and G.9b, respectively.



(a) Displacements in x-direction.

(b) Displacements in y-direction.

Figure G.9: Displacements in x- and y-direction when the structure is subjected to bolt loads. Note that the displacements are scaled.

G.3 Additional dynamic response analysis results

Note that the results are given for the direction and wave period giving the maximal results for the respective variable. The results in this section is based on a equivalent diameter equal to the diagonal of the rectangular sections.

Maximal displacements and accelerations

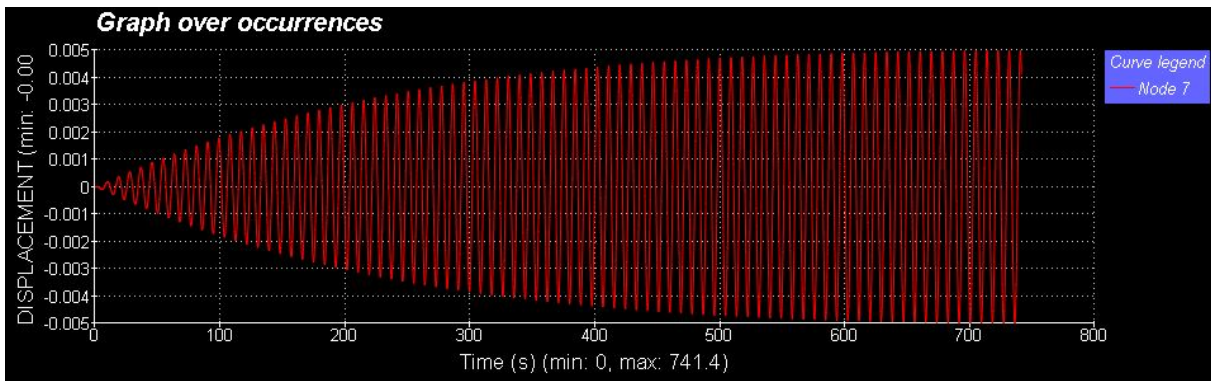


Figure G.10: Time record of vertical displacement amplitudes due to regular swell wave $T_p = 8.9s$, $\beta^0 = 110^\circ$.

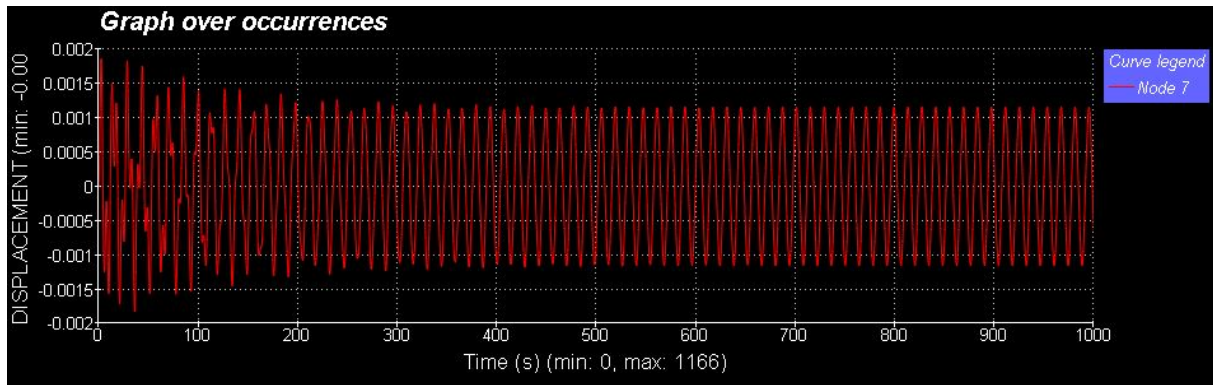


Figure G.11: Time record of transverse displacement amplitudes due to regular swell wave $T_p = 14s$, $\beta^0 = 110^\circ$.

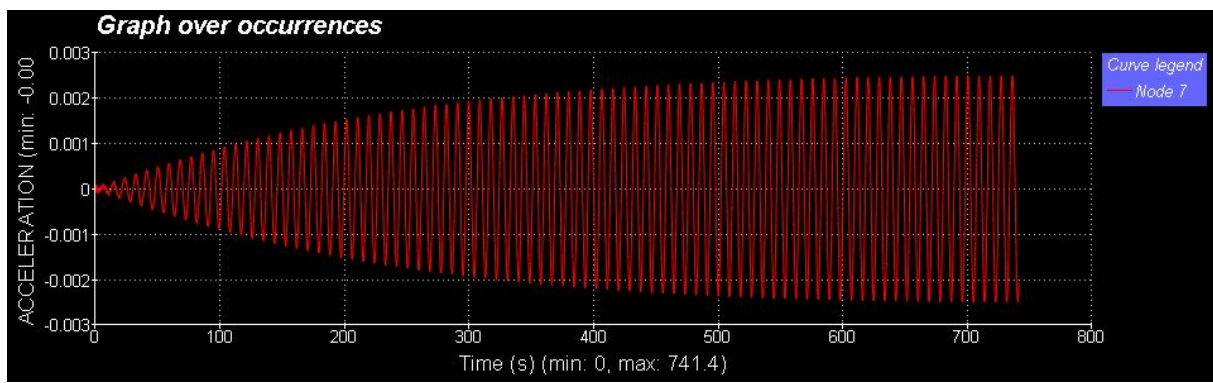


Figure G.12: Time record of vertical acceleration amplitudes due to regular swell wave $T_p = 8.9s$, $\beta^0 = 110^\circ$.

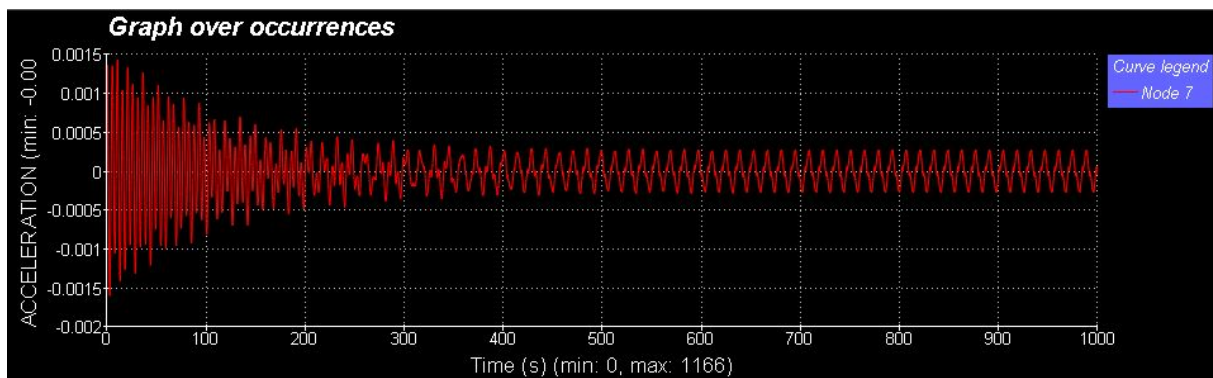
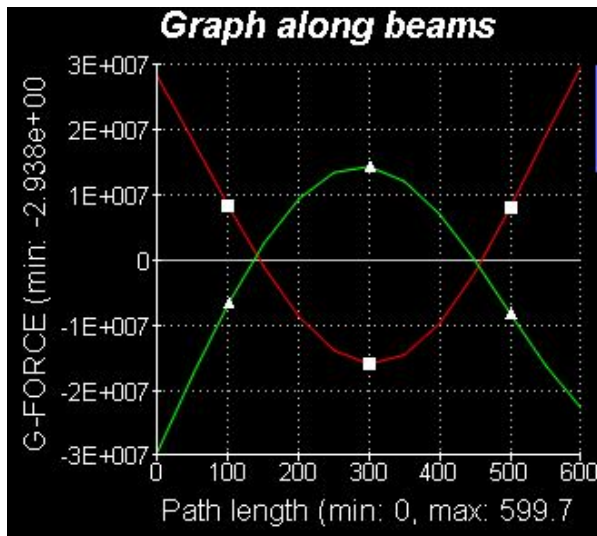
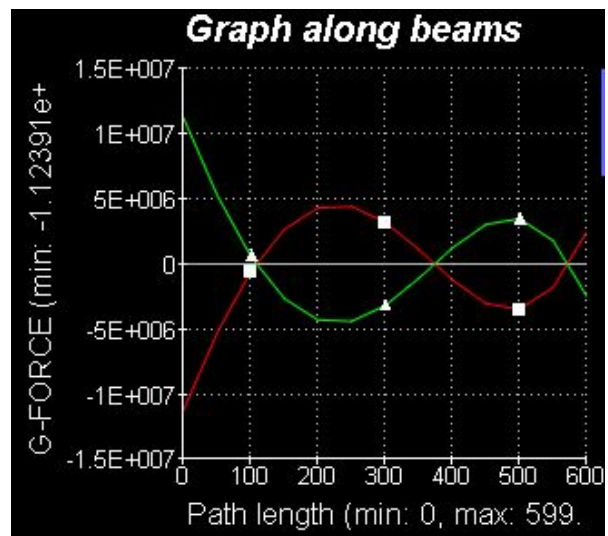
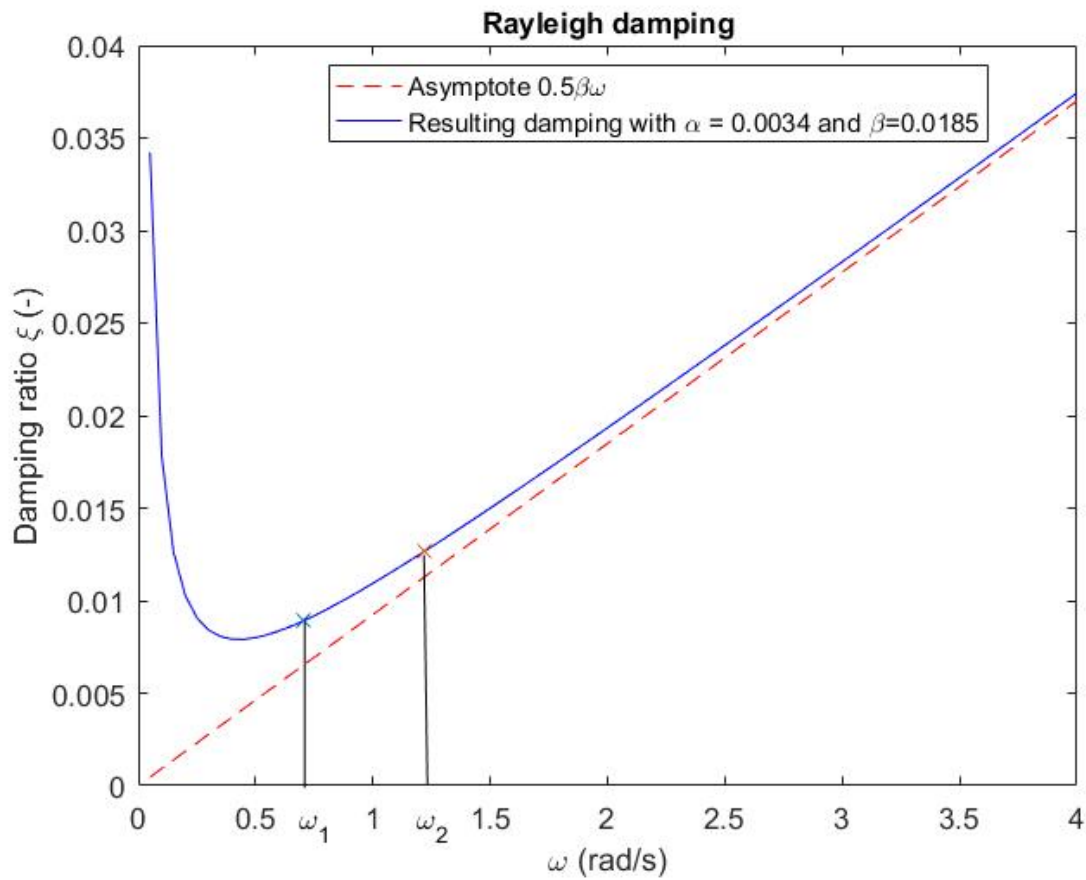


Figure G.13: Time record of transverse acceleration amplitudes due to regular swell wave $T_p = 14s$, $\beta^0 = 110^\circ$.

Envelopes of maximal bending moments

(a) M_{xy} , bending moment about z-axis.(b) M_{xz} , bending moment about y-axis.Figure G.14: Envelopes of maximal bending moments due to regular swell sea with $T_p = 14s$, $\beta^0 = 110^\circ$.

Rayleigh-damping coefficients for different damping ratios

Figure G.15: Damping ratio versus angular frequency. $\xi_i = 0.8\%$ and $\xi_j = 1.5\%$

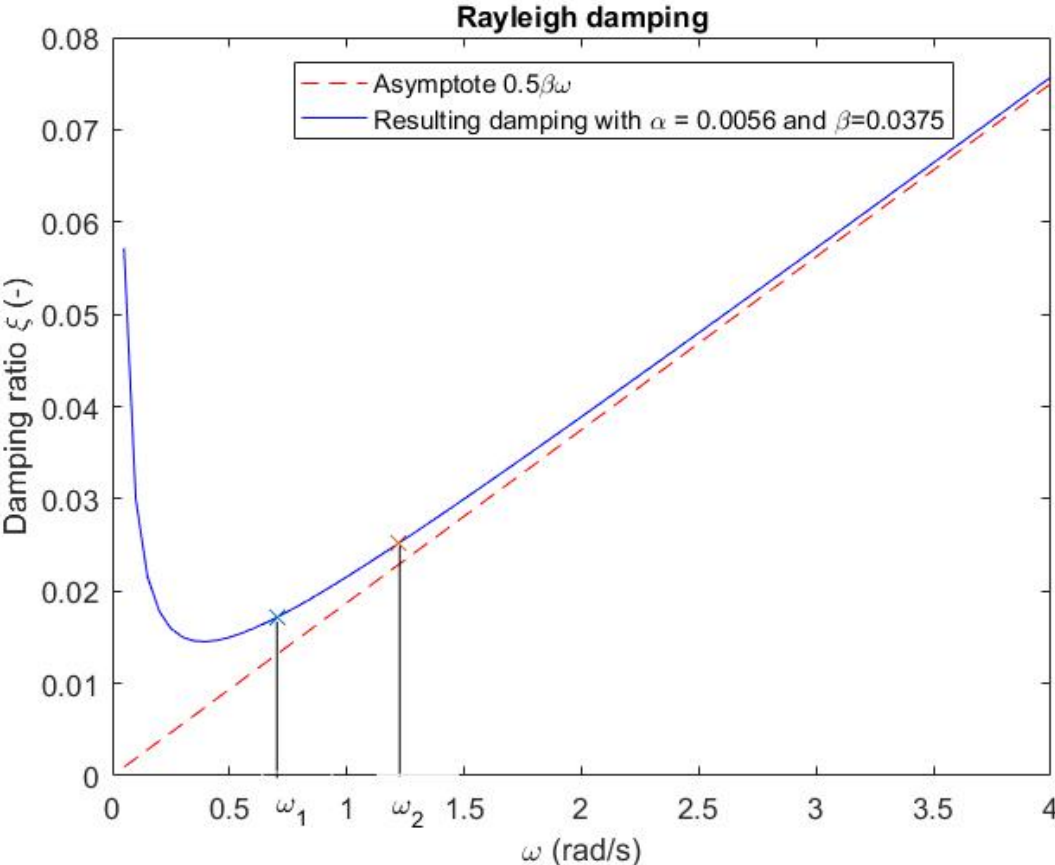


Figure G.16: Damping ratio versus angular frequency. $\xi_i = 1.5\%$ and $\xi_j = 3.0\%$

Appendix H

Hand-calculations for checking results from static analysis in Sestra

H.1 Selfweight check

To verify that the established FEM-model give reasonable results when applying the self-weight with the built-in option, the results are compared with analytic hand-calculations based on simple beam theory.

The comparison is carried out for straight configuration of the bridge, with a constant average cross-section and constant mass. In this calculation, the two ends are assumed clamped, ie. all degrees of freedom are fixed. The following calculation model is used to calculate the resulting moment at the two ends and at the mid-point of the beam (fig. H.1).

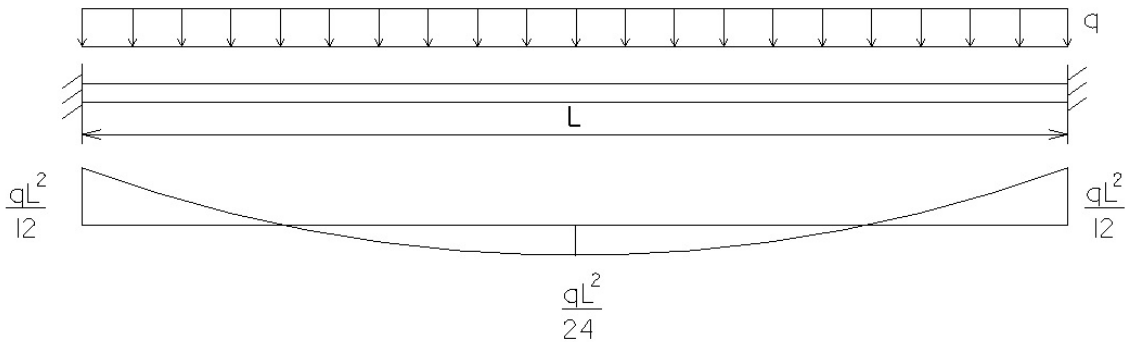


Figure H.1: Illustration of clamped plate with uniform distributed load and resulting moment diagram

q is calculated by use of the gravitational law:

$$G = mg \quad (\text{H.1})$$

m is the self-weight of reinforced concrete given by:

$$m = \rho_{\text{concrete}} V_{\text{concrete}} \quad (\text{H.2})$$

where V_{concrete} is the concrete volume.

Combining eq. H.1 and H.2 the expression for the distributed load q (N/m) is obtained:

$$q = \rho_{\text{concrete}} Ag \quad (\text{H.3})$$

The following parameters are used in the hand-calculations:

Table H.1: Calculation parameters

Parameter	Value
A	$59.8m^2$
ρ_{concrete}	$3345kg/m^3$
L	$600m$
g	$9.81m/s^2$

Where A is the cross-section area of the simplified cross-section, ie. the one without the inner sections.

H.2 Buoyancy check

The check was carried out by applying the buoyancy in two different ways, both by the built-in way in GeniE described earlier, and by applying the buoyancy manually as external distributed loads, pointing upwards. The magnitude of the buoyancy in kN/m was calculated and applied manually for each element by the formula:

$$B = \rho g A_{\text{element}} \quad (\text{H.4})$$

In this context, A_{element} is the whole circumscribed area. Meaning, $A_{\text{element}} = b_1 h_1$.

The bending moments in z-direction caused by buoyancy was then checked for both methods, giving the results in table H.2:

Table H.2: Maximal bending moments caused by buoyancy

	M_{xy} (GNm) at ends	M_{xy} (GNm) at midspan
Wajac	63.381	-27.569
Manually applied	63.532	-27.663

From table H.2 it is seen that the two methods give similar results. Wajac slightly underestimates the buoyancy. The deviation can also be caused by round-off errors. It is therefore concluded that the buoyancy is correctly applied using Wajac.

Appendix I

MATLAB script

I.1 Script estimating the Rayleigh damping coefficients

```
% This script contains information needed for calculation of coefficients
% used for Rayleigh damping

% Eigenfrequencies from GeniE
w = [0.112 0.194 0.297 0.335 0.569 0.646 0.921 1.036 1.351 1.529];
wa = 2*pi*w; % Angular eigenfrequencies
wk = [0.05:0.05:4]; % Frequency range (x-axis in plot)

% Desired damping ratios
eta1 = 0.005;
eta2 = 0.008;
eta3 = 0.015;

% Calculation of coefficients
[alpha,beta] = coeff(eta1, eta2, eta3)

% Damping ratio corresponding to first and second eigenfrequency
ratio1 = 0.5*((alpha*(1/wa(1)))+(beta*wa(1)));
ratio2 = 0.5*((alpha*(1/wa(2)))+(beta*wa(2)));

%-----Plotting-----
asyp = zeros(length(wk),1); % Asymptote
ratio = zeros(length(wk),1); % Damping ratio graph
for i = 1:length(wk)
    asyp(i) = 0.5*beta*wk(i);
    ratio(i) = 0.5*((alpha*(1/wk(i)))+(beta*wk(i)));
end
%{
figure(1)
plot(wk, asyp, '--r')
hold on
plot(wk, ratio, 'b')
hold on
plot(0.70336, ratio1, 'x') % Ratio corresponding to first eigenperiod
hold on
plot(1.21832, ratio2, 'x') % Ratio corresponding to second eigenperiod
title({'Rayleigh damping'}, 'FontSize', 10)
ylabel('Damping ratio \xi (-)')
xlabel('\omega (rad/s)')
grafnavn={'Asymptote 0.5\beta\omega', 'Resulting damping with \alpha = 0.0026 and \beta=0.0095'};
legend(grafnavn, 'Location', 'northeast')
%}
%{
figure(2)
plot(wk, asyp, '--r')
hold on
```

```
plot(wk, ratio, 'b')
hold on
plot(0.70336, ratio1, 'x') % Ratio corresponding to first eigenperiod
hold on
plot(1.21832, ratio2, 'x') % Ratio corresponding to second eigenperiod
title({'Rayleigh damping'}, 'FontSize', 10)
ylabel('Damping ratio  $\xi$  (-)')
xlabel('\omega (rad/s)')
grafnavn={'Asymptote 0.5\beta\omega', 'Resulting damping with \alpha = 0.0034 and \beta=0.0185'};
legend(grafnavn, 'Location', 'northeast')
%}
figure(3)
plot(wk, asymp, '--r')
hold on
plot(wk, ratio, 'b')
hold on
plot(0.70336, ratio1, 'x') % Ratio corresponding to first eigenperiod
hold on
plot(1.21832, ratio2, 'x') % Ratio corresponding to second eigenperiod
title({'Rayleigh damping'}, 'FontSize', 10)
ylabel('Damping ratio  $\xi$  (-)')
xlabel('\omega (rad/s)')
grafnavn={'Asymptote 0.5\beta\omega', 'Resulting damping with \alpha = 0.0056 and \beta=0.0375'};
legend(grafnavn, 'Location', 'northeast')
```

Appendix J

Sesam scripts

J.1 Wajac analysis control file

```
WAJAC
TITL      Wajac run name : Analysis1.step(2)
C
C
C          PREFIX
FMOD      GeniEModel
C
C          PREFIX          FORM
FWAVE     WajacWave      FORMATTED
C
C          UNITS  GRAVITY    RHO    VISC    RHOAIR  VISCAIR
CONS      1.      9.80665    1014.  1.19e-006  1.226  1.462e-5
C
C          OPT1    OPT2    OPT3    OPT4    OPT5    OPT6    OPT7
OPTI      0.      1.      0.      0.      0.      0.      0.
C
C          0.      0.      0.      0.      0.      0.
C
C          ILFSAV  ISETOP
MODE      1.      1.
C
C          LN
LONO     1.
C
C          ***** GEOM Section *****
GEOM
C
C          Z
MUDP     -200.
C
C          ***** HYDR Section *****
HYDR
C
C          TYPE
CPRI     SPEC
C
C          ADMAS    DAMP
MASS     1.      0.
C
C          HydroDynamicDiameter2 ( Hydrodynamic Diameter property )
C
C          M1      M2      INC      STYP  IDX  DIAM          IGWD
SPEX     2.      0.      0.      1.   1.   16.66  0.7  0.7  -1.  0.
SPEX     11.     0.      0.      1.   1.   16.66  0.7  0.7  -1.  0.
C
C          HydroDynamicDiameter3 ( Hydrodynamic Diameter property )
C
C          M1      M2      INC      STYP  IDX  DIAM          IGWD
SPEX     3.      0.      0.      1.   1.   16.37  0.7  0.7  -1.  0.
SPEX     10.     0.      0.      1.   1.   16.37  0.7  0.7  -1.  0.
C
C          HydroDynamicDiameter4 ( Hydrodynamic Diameter property )
```

```

C
C      M1      M2      INC      STYP      IDX      DIAM
SPEX      4.      0.      0.      1.      1.      16.07  0.7  0.7  -1.  0.
SPEX      9.      0.      0.      1.      1.      16.07  0.7  0.7  -1.  0.
C
C      HydroDynamicDiameter5 ( Hydrodynamic Diameter property )
C
C      M1      M2      INC      STYP      IDX      DIAM
SPEX      5.      8.      1.      1.      1.      15.92  0.7  0.7  -1.  0.
C
C      HydroDynamicDiameter1 ( Hydrodynamic Diameter property )
C
C      M1      M2      INC      STYP      IDX      DIAM
SPEX      1.      0.      0.      1.      1.      16.95  0.7  0.7  -1.  0.
SPEX     12.      0.      0.      1.      1.      16.95  0.7  0.7  -1.  0.
C
C      BuoyancyArea1 ( Buoyancy Area property )
C
C      M1      M2      INC STYP  IDX      ANFLD      AFLD
BUOA      5.      8.      1.  1.  1.      198.      198.
C
C      BuoyancyArea2 ( Buoyancy Area property )
C
C      M1      M2      INC STYP  IDX      ANFLD      AFLD
BUOA      4.      0.      0.  1.  1.      202.673   202.673
BUOA      9.      0.      0.  1.  1.      202.673   202.673
C
C      BuoyancyArea4 ( Buoyancy Area property )
C
C      M1      M2      INC STYP  IDX      ANFLD      AFLD
BUOA      3.      0.      0.  1.  1.      210.298   210.298
BUOA     10.      0.      0.  1.  1.      210.298   210.298
C
C      BuoyancyArea5 ( Buoyancy Area property )
C
C      M1      M2      INC STYP  IDX      ANFLD      AFLD
BUOA      2.      0.      0.  1.  1.      217.923   217.923
BUOA     11.      0.      0.  1.  1.      217.923   217.923
C
C      BuoyancyArea6 ( Buoyancy Area property )
C
C      M1      M2      INC STYP  IDX      ANFLD      AFLD
BUOA      1.      0.      0.  1.  1.      225.548   225.548
BUOA     12.      0.      0.  1.  1.      225.548   225.548
C
***** LOAD Section *****
LOAD
C
C      ElementRefinement1 ( Element refinement property )
C
C      Z1      Z2      SEG      SLMIN      SLMAX IMEM
SEGM      0.  250.143      1.      0.      0.  1.
C
C      M1      M2      INC STYP  IDX IMEM
MEMSEG     1.      12.      1.  1.  1.  1.
C
C      ISEA THEO  HEIGHT  PERIOD  PHI0      T0      STEP      NSTEP
SEA      1.  1.1      0.19      14.      0.      0.      10.      -3000.
C
C      ISEA BETA WKFA CTNO CBFA CSTR LOAD DLOA  WID WIME IDPT
SEAOPT   1. 110.  1.  0.  1. -1.  5.  0.  0.  0.  1.
C
C      DEPTH IDPT
DPTH     250.  1.
C
C      X      Y      Z
MMMT     0.      0.      0.
END

```

J.2 Sestra dynamic analysis control file

```

COMM
COMM
COMM HEAD Job_time_domdyn - SestraDynamicTime
COMM Superelement: 1
COMM Dynamic time domain analysis
COMM Multifront solver used
COMM
COMM Data Formats - the numbers are right adjusted in the fields
COMM <-1-><-2-><-3-><-4-><-5-><-6-><-7-><-8-><-9-><-10-><-11-><-12->
COMM <-1-><-2-><-3-><-4-><-5-><-6-><-7-><-8->
COMM
COMM
COMM CHECK ANTP MSUM MOLO STIF RTOP LBCK      PILE      CSIGN      SIGM
CMAS   0.   2.   1.   0.   0.   0.   0.
COMM
COMM -----INPUT AND OUTPUT FILES-----
COMM
COMM                PREF                FORMAT
INAM ..\_repository\GeniEModel
COMM
COMM                PREF                FORMAT
INAM ..\_repository\WajacWave
COMM
COMM                PREF                FORMAT
RNAM ..\_repository\SestraDyn          SIN
COMM
COMM ----- DIRECT TIME DOMAIN ANALYSIS -----
COMM
COMM ITP1
ITOP  1.
COMM
COMM
COMM CALTYP                RESVA      BETA      THETA      H(tmstp)
FRSP  4.                    1.      0.25     0.         1.0E-3
COMM
COMM ----- STRUCTURAL DAMPING -----
COMM
COMM          ALPHA_1          ALPHA_2
MDAP  0.0026                0.0095
COMM
COMM ----- REQUESTED RESULTS -----
RETR  3.
COMM ISEL1 ISEL2  ISEL3 ISEL4 ISEL5 ISEL6 ISEL7 ISEL8
RSEL  1.   1.   1.         1.
COMM
COMM SELTY
IDTY  1.
COMM
COMM ----- INCLUDING ADDED MASS -----
COMM IMAS IDNA ISST
DYMA  1.
COMM
Z

```